Einar Løvli Hidle

Early Detection of Subsurface Cracks in Rolling Element Bearings using the Acoustic Emission Time Series

June 2021

NTNU
Norwegian University of
Science and Technology
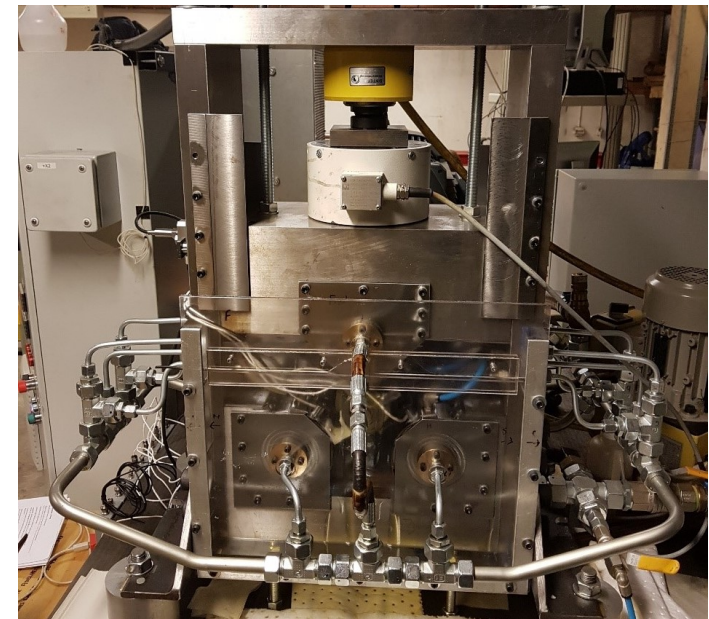
NTNU
Norwegian University of Science and Technology

Early Detection of Subsurface Cracks in Rolling Element Bearings using the Acoustic Emission Time Series

Einar Løvli Hidle

Abstract

The formation and propagation of rolling contact fatigue (RCF) induced subsurface cracks (SSC) in a test specimen roller have been monitored using the acoustic emission time series. The sampled acoustic emission (AE) waveforms were obtained from a duration test. During testing, phased array ultrasonic testing (PAUT) were performed on scheduled intervals to monitor SSC initiation and growth. After the duration test was terminated, salami cutting post inspection revealed three RCF induced SSCs.

A monitoring system using a mathematically deterministic detector, capable of independent isolated detection of multiple RCF induced SSCs occurring simultaneously in a rotating machinery is proposed in this thesis. Outputs from the detector and positive detector decisions, are fully verifiable using a tool proposed in this thesis called the *pulse integrated spectrogram* (PIS).

Four different defect behaviours were observed in the sampled AE waveforms. All behaviours were independently detected with the proposed monitoring system. The behaviour with the given name *rollerPass,* was confirmed as an SSC originated behaviour. Positive detector decision, *defect detected*, for rollerPass happened April 30, 2021. The decision was verified with PIS. At the time of detection, the SSC was 1 mm wide, confirmed in PAUT.

A review of the published research on the field that is detection of RCF induced SSCs in rolling element bearings (REB) using AE is presented in this thesis. The review reveals that unverifiable results can have caused false claims of success for the solutions presented. A criterion of confidence is therefore proposed to prevent future publications from disrupting the progress in this field of research.

Acknowledgements

AEMON

Novel Failure Monitoring System for Marine Applications by including Acoustic Emission

Gearboxes represent a critical part of the rotating machinery found in maritime vessels and wind turbines. Due to the cyclic loading conditions gears and rolling element bearings are exposed to, these components are typically the first to fail due to fatigue induced failure mechanisms. Failure in a single component imposes an evident risk of total machine failure, which is costly.

For this reason, condition monitoring systems are typically applied to alert the machine owner if a defect is present in the rotating machinery. However, the condition monitoring systems used today are mainly vibration-based and can only detect surface defects such as cracking and spalling. Thus, by the time the monitoring system identifies a defect in a component, this component might already be at risk of failure.

The AEMON project is a collaboration between NTNU and SINTEF and the industry partners Kongsberg Maritime, Kongsberg Maritime CM, Equinor Energy and Island Offshore. In this project a condition monitoring system based on Acoustic Emission will be developed to identify defects in rotating machinery at an earlier stage than what is currently possible with vibration-based systems. The project is funded by the Research Council of Norway under the MAROFF-2 programme.

Table of Contents

List of Tables

List of Figures

List of symbols, detector.

Symbol	Unit	Description
c		Confidence, that is, the number of consecutive detections required for the detector to decide that a defect is present.
$D(L, T, c)$		Decision function.
d_s	samples	The length (in samples) of each between r_s and r_{s+1}.
f_{alias}		The number of times a *bearing defect alias* excites an AE pulse. Per rev, or per second.
f_{fault}	$[1/rev]$ or $[Hz]$	The number of times a bearing defect excites an AE pulse. Per rev, or per second.
f_s	$[Hz]$	Sample rate
h	Peaks in K-spectrum	The set from 1 to the number of peaks in K-spectrum.
i	windows	The set from 0 to the Number of windows, minus 1.
j	Sub-windows	The set from 0 to the Number of sub-windows between, r_s and r_{s+1} minus 1.
K_i		K-spectrum.
L		The likelihood ratio for a given $x[n]$
l_{signal}	samples	Length of $x[n]$, in samples. Equal to $max(n)$
l_w	samples	Window length
m	windows	Peak window range in K-spectrum.
mad		Median absolute deviations
$M_{i,r}$		Rows: Windows Columns: Extracted AE pulses, one for each sub-window
$\widetilde{M}_{i,r}$		$M_{i,r}$, row-outliers removed.
N_i		The i-th row in $M_{i,r}$.

o_w	samples	Window overlap
$p_{j,s}^i[l_w, o_w]$		Sub-window start-position
p_{loc}	windows	Peak-window-positions in K-spectrum
$\hat{p}_{loc}$	windows	Peak-window-positions in K-spectrum, sorted according to p_{max}.
p_{max}		Maximum peak-values in K-spectrum
p_{width}	windows	Peak-widths in K-spectrum
$\hat{p}_{width}$	windows	Peak-widths in K-spectrum, sorted according to p_{max}.
peakPower		The peak in K-spectrum with the highest prominence divided by its width
r	Sub-windows	The set from 0 to the total number of sub-windows per window, minus 1.
r_m	$[n]$	The n-th relative start-position of the m-th recorded axle rotation. For $f_{fault} = [1/rev]$. The n-th relative pulse-position for every g-th pulse. For **odd** $f_{fault} = [1/rev]$. The n-th relative pulse-position for every g-th pulse. For $f_{fault} = [Hz]$.
r_s	$[n]$	$r_s = r_1, r_2, \dots, r_{m-1}$, where $s = \{1,2,3, \dots, m-1\}$
T		Threshold
$w_{j,s}^i[n, l_w, o_w]$		Window function
$x[n]$	[V] (Volt)	The continuously sampled AE waveform
$y_{j,s}^i[l_w, o_w]$		Extracted AE pulse

List of Abbreviations

AE   Acoustic Emission

AI   Artificial intelligence

BPFO   Ball Pass Frequency Outer

CBM   Condition Based Monitoring

DL   Deep Learning

IFD   Intelligent fault analysis

NP   Neyman-Pearson

NTNU   Norwegian University of Science and Technology

PAUT   Phased Array Ultrasonic Testing

PIS   Pulse integrated spectrogram

REB   Rolling Element Bearing

RCF   Rolling Contact Fatigue

RM   Rotating machinery

RPM   Rotations per minute

SNR   Signal-to-noise ratio

SPx   Sensor position x

SSC   Subsurface crack

SSD   Solid State Drive

STFT   Short-time Fourier Transform

TL   Transfer Learning

TML   Traditional machine learning

VA   Vibration Analysis

Introduction

1.1 The current status

In 1993, (Yoshioka, 1993) published the research paper that is considered the first documented identification of subsurface cracks present in acoustic emission waveform from a rolling element bearing. In 2005 (Price, Lees, & Friswell, 2005) published a similar study where physical inspection revealed the presence subsurface cracks in the test specimens. Since then, only a handful of papers have been published on this field of research. The results from these papers are unverified, and thus have not contributed to significant progress that can be considered useful to the path of creating the first functional subsurface crack detection system. By the addition of the typical black-box properties of machine learning models, the results are harder to verify, thus preventing the concept from reaching a level of acceptance and credibility as a tool for real world machine monitoring problems. As a result, subsurface crack detection in rolling element bearings using the acoustic emission time series remains today a niche topic in the condition monitoring world.

1.2 The proposal

The acoustic emission (AE) from a rotating machinery (RM) can be described as waveform with a continuously changing noise floor. Rolling contact fatigue (RCF) induced subsurface cracks (SSCs) are present in the waveform as short bursts of energy, or pulses, usually completely hidden in the noise. The problem is thus to *find* these pulses. There exists a well-established field of science that deals with a similar problem. That is, *the radar target detection problem.*

With this thesis, the main objective is to introduce a new way to address the problem of SSC detection in REB using AE, and to hopefully motivate the AE community to welcome a cross-disciplinary mindset. The chosen approach to the SSC detection problem takes advantage of detection criteria derived from the established signal processing radar literature. The monitoring system proposed in this thesis uses a mathematically deterministic detector capable of independent isolated detection of multiple RCF induced SSCs occurring

simultaneously in an RM. All outputs from the detector are fully verifiable, and positive detector decisions can be verified with confidence.

1.3   Research method in brief

The following work focus on the analysis of acoustic emission (AE) monitoring of an REB exposed to RCF induced SSCs. From the recorded AE waveforms, the SSCs are to be detected as early as possible, with a verifiable detector decision.

1.4   Problem Statement

The main objective for this work is to:

- Analyse AE waveforms gathered from a roller bearing duration test, executed on a roller bearing test machine located at NTNU.
- Present the mathematical description of a proposed detector capable of detecting RCF induced SSCs and other REB related defects.
- Present the evolving trend for all defect behaviours detected during the duration test. Detector decisions indicating *defect detected* are displayed and discussed.

1.5   Structure of the report

Section 2 reviews theory and literature relevant to the problem statement in 1.4. Fatigue induced failure mechanisms in REBs, the AE phenomena, detection theory of noise contaminated signals, and literature review are presented.

Section 3 explains the experimental setup for the duration test, AE recording systems, and the complete mathematical description of the proposed detector.

Section 4 presents all defect behaviours observed during the duration test, detector decisions, and detector decision verifications.

In section 5, the results are interpreted and the discussed. The performance of the proposed detector is evaluated and compared to the existing literature.

Conclusions and proposed further work are given in section 6.

2   Theory and literature review

2.1   Condition monitoring

Condition-based maintenance (CBM), also called predictive maintenance or condition monitoring is a maintenance strategy that recommends maintenance procedures based on condition monitoring data (Y. Lei, 2016, p. 6), such as AE waveforms and vibrations. CBM can reduce machine downtime and ensure proper operation. The strategy can be split into three stages: data acquisition, data processing and decision making. Data acquisition is the process of collecting sampled sensor data such as AE, temperature, ambient moisture etc. At the data processing stage, relevant features are extracted from the raw data sampled in stage one. The extracted features then act as a basis for the decision-making stage. This module will interpret the extracted features and give a health estimate of the current machine and suggest maintenance actions. Decision criteria and AI models can be used for diagnosis and estimate the probability of present defects (Martin-del-Campo & Sandin, 2017, p. 1).

2.2   Fatigue related failure in bearings

Rolling element bearings (REBs) are susceptible to multiple forms of damage including corrosion, denting, electrical erosion, fracture and spalling (Watanuki, Tsutsumi, Hidaka, Wada, & Matsunaga, 2021, p. 952). Under proper operation conditions, the elements of bearings, such as rollers and raceways, are exposed to multiaxial and non-proportional low and high-cycle fatigue loadings, which are usually the source of the rolling contact fatigue (RCF) (Romanowicz & Szybiński, 2019, p. 1). The two most dominant RCF mechanisms are subsurface originated spalling and surface originated pitting (Jalalahmadi, Slack, Raje, & Arakere, 2009, p. 2). Both of which can happen after a long period of operation. Spalling leads to increased vibration in the bearing, but usually not critical malfunction of the rotating machine (Watanuki et al., 2021, p. 952). However, at the point of spalling, debris is introduced to the rest of the mechanical system, thus accelerating the overall failure process (Fuentes, Dwyer-Joyce, Marshall, Wheals, & Cross, 2020, p. 776). Small localized stress

risers such as spalling can also lead to fatigue originated bearing fracture, which imposes a critical risk of machine breakdown (Watanuki et al., 2021, p. 952).

Subsurface originated spalling occurs when microcracks initiate below the surface and propagate toward the surface to form a surface spall. Microplastic deformation precedes crack initiation and typically occurs at microstructural discontinuities such as non-metallic inclusions and carbide clusters, often referred to as *stress risers*. In these areas, the resultant stress exceeds the local microyield limit in a fatigue cycle. (Jalalahmadi et al., 2009, p. 2). It is observed that non-metallic inclusions with size larger than 13 µm significantly decreases fatigue life (Romanowicz & Szybiński, 2019, p. 4). The formation of these cracks is found to originate in the region of maximum shear stress *below* the surface, which is displayed in

Figure 1
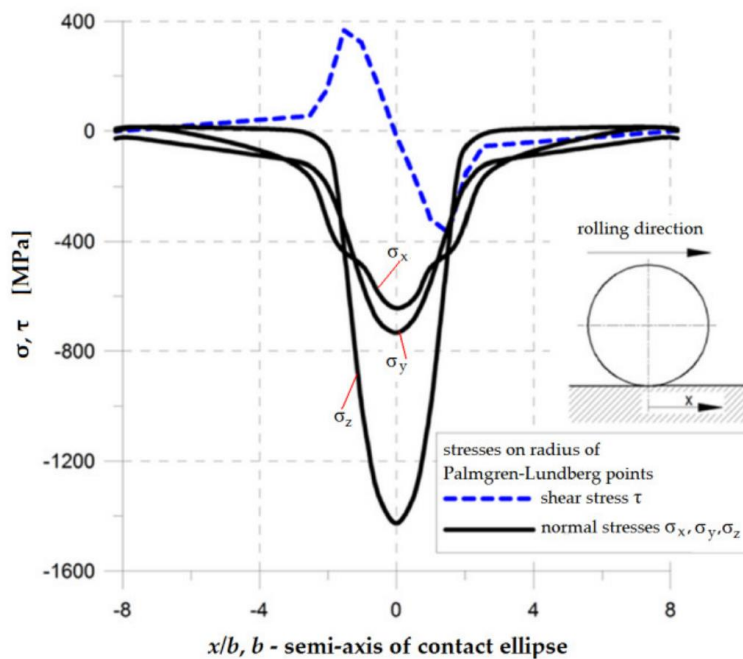
Figure 1, Typical subsurface stress distribution for rolling contact (Romanowicz & Szybiński, 2019, p. 5).

Smooth surfaces, non-metallic inclusions and absence of surface shear are factors that favour subsurface originated spalling. In properly installed and lubricated bearings, this is the main form of fatigue failure (Romanowicz & Szybiński, 2019, p. 4). Surface oriented pitting, on the other hand, occurs where surface irregularities, typically caused by sliding between contacting surfaces, initiate cracks. This is typically relevant on the contact surfaces in gear teeth, (Jalalahmadi et al., 2009, p. 2) but bearings exposed to varying degree of surface

traction shear forces, and/or with lower grade of surface smoothness, can also be prone to surface originated fatigue failure, as will be described below.

In most loading conditions, fatigue tends to originate at the surface of the materials. High stresses and imperfections due to manufacturing surface wear coalesce lead to crack initiation. In rolling element bearings however, Hertzian contact theory dictates that the highest stress present in interacting bearing rollers can be located a small distance below the surface (Fuentes et al., 2020, p. 776). Lundberg and Palmgren (Lundberg & Palmgren, 1947) were the first to provide a theoretical model for bearing life. They supposed that cracks initiate subsurface due to the simultaneous occurrence at a particular depth of the maximum orthogonal shear stress combined with the presence of a stress riser. The location of the maximum orthogonal shear stress is known as Palmgren-Lundberg's points, seen in Figure 2 (Romanowicz & Szybiński, 2019, p. 4). The stress ricers were expected to be stochastically distributed throughout the material. Weibull statistical fracture theory was applied to the stressed volume derived from pure Hertzian contact to predict the durability of the volume when exposed to subsurface initiated fatigue.
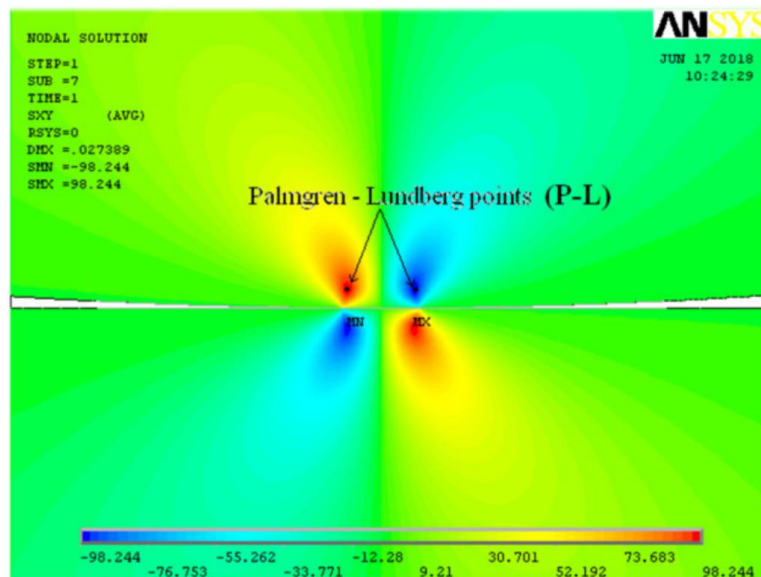
Figure 2, Distribution of subsurface shear stress. Obtained by finite element method (FEM) (Romanowicz & Szybiński, 2019, p. 5).

Since the publication, the theory has become widely accepted and today forms the basis for the industry bearing life standard, ISO 281. However, it completely disregards the possibility

of surface originated failure, and the aspect of lubrication and hence lubrication film. Load direction is assumed to be normal only, without surface shear traction. In practical scenarios, some surface traction will always be present, and thus moves the location of maximum orthogonal shear stress closer to the surface. Assuming pure Hertzian contact also implies that the contacting surfaces are perfectly smooth, which rarely the case real REBs. The stress field will thus deviate considerably from the pure Hertzian case (Jalalahmadi et al., 2009, p. 3). Numerous methods have been developed to cope with these shortcomings, but they are outside the scope of this thesis.

Material degradation caused by RCF in a bearing can be described as a three-stage process: shakedown (1), steady-state elastic response (2), and instability (3). At shakedown, material strength and micro yield stress are increased due to induced residual stress from work hardening and possibly transformation of retained austenite to martensite. Subsurface volume exposed to plastic deformation is reduced to nearly zero. A higher initial load applied during this stage results in a higher saturation level of work hardening, thus extending fatigue life by modifying material response in the next two stages.

Stage 2 describes the period of operation where cyclic response is elastic and no fatigue damage is expected to occur. The duration of this period is a function of maximum stress, mechanical properties, and operating temperature, where operating temperature is highly relevant. Stability of finely dispersed carbides in the tempered martensite is also considered important for prolonging this stage. Maintaining a stage 2 operating condition is critical to bearing fatigue life.

At stage 3, material softening caused by an increase in plastically deformed subsurface volume causes a decrease in yield stress. The softening is thought to be caused by slip systems induced by carbon diffusion due to temperature peaks. The development of a radial tensile stress and texture development promotes growth of cracks parallel to the rolling surface (Jalalahmadi et al., 2009, pp. 1-2).

It is observed that spalls originated from indentations in ball bearings develop initially at the trailing edge of a pre-indented raceway with a typical V-shaped spall. In this location, the raceway material first detaches at the edge of the dent, forming a V-shaped damaged area, before growing at fast rate along the raceway. Roller bearings, however, follow the well-known behaviour of slowly growing the spall directly across the raceway, before continuing along the rolling path (Morales-Espejel & Gabelli, 2015, p. 418).

2.3 Acoustic Emission Fundamentals

ASTM, formerly American Society for Testing and Materials, proposed in 2020 an AE standard named ASTM E1316 20. In this standard, the definition of AE is given as: *The class of phenomena whereby transient stress/ displacement waves are generated by the rapid release of energy from localized sources within a material, or the transient waves so generated* (He et al., 2021, p. 4). Rapid release of energy, are typically caused by plastic deformation, crack propagation and dislocation motion during growth of flaws in solids (Eitzen & Wadley, 1984, pp. 75-76).

When a component is impacted by an external drive, the concentrated energy source begin to release elastic mechanical waves (Meserkhani, Jafari, & Rahi, 2021, pp. 1-2). These waves are often referred to as AE- *hits*, *events* and *pulses*. Depending on how the material is excited, a combination of longitudinal, transversal and surface waves propagate through the solid to the surface of the component. Each wave propagate at different speed and carry a different percentage of the total energy (Fuentes, Howard, Marshall, Cross, & Dwyer-Joyce, 2016, p. 1371).

2.3.1 Transfer Function Formalism

To extract quantitative information from an AE event, the source of the event must be mathematically expressible. Scruby has shown that an AE source can be represented as a point source with two main assumptions (Leser, Yuan, & Newman, 2013, p. 2). The source is assumed to be internal and self-equilibrating, which means that every force or couple making up the source must be a force dipole or double couple. The second assumption is that all forces involved in making up the source, must occur simultaneously and thus share the same history (Leser et al., 2013, p. 2). If the first assumption is ignored, the displacement response on the body surface due to a point source can then be described as follows:

Let the force, $h_j(\vec{\xi}, t)$ be applied to a body at position $\vec{\xi}$ in direction j at time t. The displacement vector, $u_i(\vec{x}, t)$ at position $\vec{x}$ in direction i can be calculated as the convolution of h_j and G_{ij}

$$u_i(\vec{x}, \vec{\xi}, t,) = (h * G)(t) = h_j(\vec{\xi}, t) * G_{ij}(\vec{x}, \vec{\xi}, t) \qquad 1$$

where $G_{ij}(\vec{x}, \vec{\xi}, t)$ is the Green's function defined as the displacement response at $\vec{x}$ in direction i from the impulse load at $\vec{\xi}$ in direction j. (Leser et al., 2013, p. 2). However, this model does not fully capture the AE phenomena. For the purpose of modelling an AE event to an electric voltage at the transducer output, additional assumptions and simplifications must be made.

AE sources are generally considered to be sharply limited in spatial extent and are usually measured over some limited frequency range due to instrumentation limitations and noise. Complex models containing the entire static and dynamic stress history of the structure are therefore excessive. However, the possibility that each stress relaxation, or AE pulse, could have a distinct temporal behaviour, complicates the calculation of the Green's tensor. To avoid this problem, two assumptions are introduced. Distributed AE sources are approximated by a Taylors expansion about a point centroid source at location, $\overrightarrow{\xi_0}$. All AE events are considered to have identical temporal behaviour (from seismology) (Eitzen & Wadley, 1984, pp. 77-79). The resulting model follows:

$$u_i(\vec{x}, \overrightarrow{\xi_0}, t) = (\overline{\Delta\dot{\boldsymbol{\sigma}}} * G)(t) = \overline{\Delta\dot{\boldsymbol{\sigma}}}_{j\hat{k}}(t) * G_{ij,\widehat{k'}}(\vec{x}, \overrightarrow{\xi_0}, t) \qquad 2$$

where $\overline{\Delta\dot{\boldsymbol{\sigma}}}_{j\hat{k}}$ is the space averaged stress drop, considered distributed at $\overrightarrow{\xi_0}$, and $\hat{k}$ is the direction of the Heaviside elastic Green's tensor (Eitzen & Wadley, 1984, p. 78). Now the response of the transducer can be included. A transducer sensitive to displacement has an impulse response that can be expressed as $TP_i(\vec{r}, t)$, $\vec{r} \in S_T$, the voltage at time t excited by a Dirac delta impulse in direction i at point $\vec{r}$ at time zero. S_T is the given surface of the body of which the transducer is connected. In frequency domain, the transfer function formalism ultimately becomes:

$$V(\omega) = T_{j\hat{k}}(\omega)\overline{\Delta\dot{\boldsymbol{\sigma}}}_{j\hat{k}}(\omega) \qquad 3$$

where $T_{j\hat{k}}(\omega)$ is the combined transfer function of the structure and the transducer. $\overline{\Delta\dot{\boldsymbol{\sigma}}}_{j\hat{k}}(\omega)$ is the stress drop tensor of the AE source (Eitzen & Wadley, 1984, pp. 77-79). By defining this transfer function, information about the source is considered passed in frequencies through the filter (transfer tensor) to the output in the manner of a linear system. The information is independently transmitted, frequency by frequency, and thus filtering and other digital signal processing tools can be used to separate the noise from the useful signals (Eitzen & Wadley, 1984, pp. 77-79).

2.3.2   The five-stage process

The process of collecting an AE signal can be described by the five-stage process expressed in Figure 3. The stages include source generation, evolution, signal transduction and signal processing (SP). An event, or AE source, arises within or near the surface of a solid. This event causes a dynamic stress or force field change at the location of the event (stage 1). This change propagates a mechanical disturbance, or elastic wave, $U(x,t)$, through the whole solid (stage 2). A sensor (usually piezoelectric) located at the surface of the solid detects the disturbance by outputting a voltage, $V(t)$, proportional to the mechanical stress acted on the transducer from the disturbance (stage 3). The raw signal is then interpreted, and relevant features are extracted using SP (stage 4). Then the extracted results from the SP is used to classify the character and significance of the AE event (stage 5). (Eitzen & Wadley, 1984, pp. 76-77).
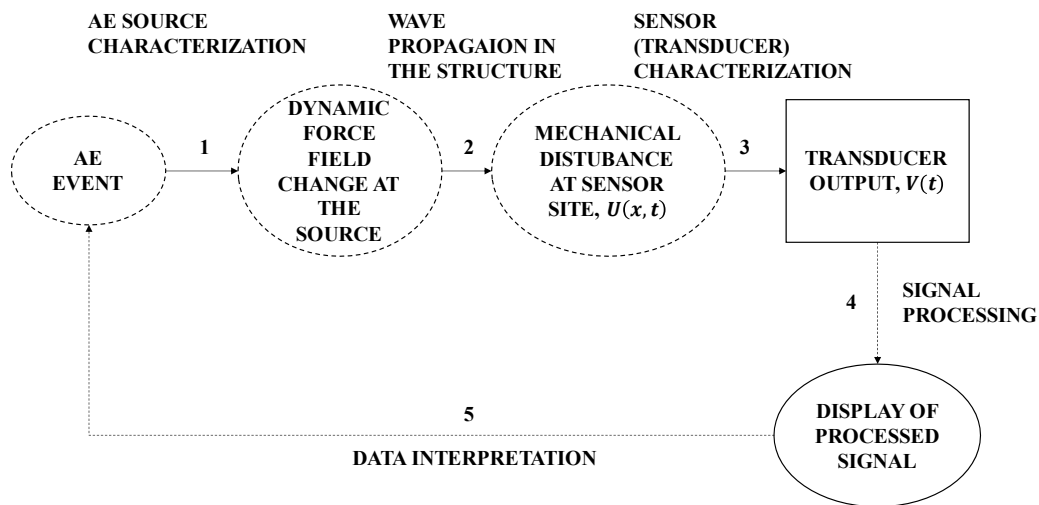
Figure 3, The causal chain of AE analysis (Eitzen & Wadley, 1984, p. 77).

Extracting informative features is no easy task, and the reason lies in how mechanical elastic waves travels through a solid. Wave propagation through a solid structure is affected by interaction with material properties, inhomogeneities, geometrical configuration of free surfaces and loading conditions. Frequency response of the chosen sensor also alter the sampled waveform. Because of these variables, the characteristics and source of an AE event is effectively unknown (Eitzen & Wadley, 1984, pp. 76-77).

9

2.3.3   AE in RM context

In the application to RM monitoring, AE is defined as transient elastic waves generated by the interaction of two media in relative motion. Sources of AE in rotating machinery include impacting, friction, cyclic fatigue, material loss, cavitation etc. For example a bearing roller passing a defect on a bearing race, will excite an AE pulse (Mba, 2006, p. 1). AE activity can be categorised into three different modes. That is *Burst type, Continuous,* and, *Mixed mode*, as seen in Figure 4.

In RMs, exclusive burst mode activity is not seen, as there are often high levels of background noise. In fixed, non-rotating machines, electrical- and background noise are the main contributors to AE noise. Rotating machines on the other hand are noisy, and AE bursts/peaks can be caused by friction, roller impact, misalignments and transient loads. These factors will sum up to a constantly changing background noise (Fuentes et al., 2020, p. 783).

Consequently, normal operating RMs will typically emit AE activity continuously, with faults such as surface pitting appearing as pulses superimposed on the continuous signal, that is, *mixed mode*. Many researches have demonstrated the ability of AE to detect faults such as pitting in bearings, but the lead time to failure of these systems is highly dependent on the level of the background noise, and thus the signal-to-noise ratio (SNR). Bursts from early wear events, such as SSCs are typically buried in noisy environments. To monitor wear at an early stage and to better understand AE generation in RMs, requires the analysis of continuously sampled AE waveforms (Price et al., 2005, p. 86).
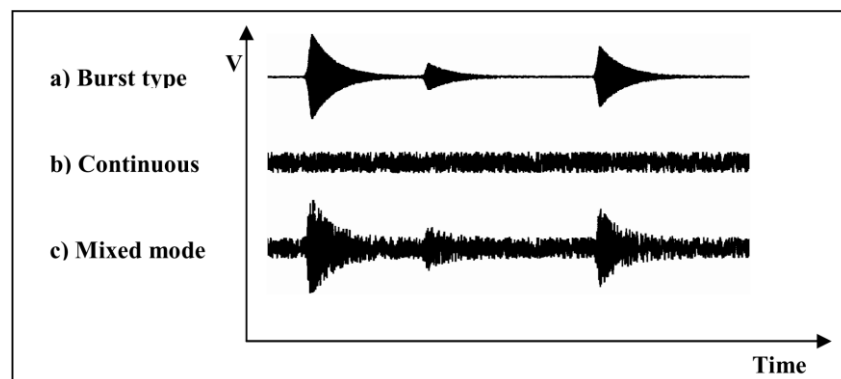
Figure 4, AE waveforms categories (Price et al., 2005, p. 86)

10

A high sampling rate is needed to successfully capture an AE-signal, typically $f_s > 1Mhz$. When sampling continuous AE waveforms, the recorded time-series are challenging to analyse because of the tremendous amounts of data. Model-based feature extraction is one approach used to overcome this issue by converting huge amounts of raw data into small feature vectors. Another challenge that affects all approaches to feature extraction from the AE time-series is the signature of a distinct RM. In formula 3, $T_{j\hat{k}}(\omega)$ can be interpreted as a filter, where the impulse response of the RM itself shapes the AE pulses as they propagate to the transducer. The impulse response of the machine will be determined by vibration paths (Yang, Lei, Jia, & Xing, 2019, p. 693), material-and mechanical properties (Zurita-Millán et al., 2016, p. 2), inhomogeneities, geometrical arrangement of free surfaces, and loading conditions (Eitzen & Wadley, 1984, p. 77). These factors all contribute to how the AE signal is altered from the AE source to the transducer (Kim & Kim, 2020, p. 2).

2.3.4 CBM using AE

Vibration analysis (VA) is the most widely used method for monitoring RMs today. However, the technique is limited to detecting surface defects *only*. That is, subsurface cracks (SSC) induced by RCF cannot be detected by VA until the SSCs propagate to the surface of a bearing element, ball/roller or raceway. This is because changes in vibration signals occur mainly due to the modification of surface geometry (Nélias & Yoshioka, 1998, p. 34).

AE is one of the non-destructive testing methods used today for CBM. One of the important benefits of AE compared to VA is the possibility to monitor SSC growth for identification of dynamic damage characteristics (Meserkhani et al., 2021, pp. 1-2). In comparison to established CBM systems, that focus mainly on VA, AE sensors operate over a far wider frequency range. The frequency band of an AE transducer is typically in the range of 20 kHz – 1 MHz, whereas the frequency band of traditional vibration transducers are in the range of 0 – 50 kHz. Because of this, traditional vibration based CBM rely heavily on the increase in amplitude of the bearing defect frequencies as damage propagated along the raceways and rollers.

With the much wider frequency range of AE sensors, research has shown that these sensors are able to detect the transient elastic surface waves caused by released strain energy during plastic deformation in materials, crack initiation and growth, and frictional sources

(Cockerill et al., 2016, pp. 1-2). To summarize, VA can only detect subsurface originated spalling and surface originated pitting, while AE technique additionally can detect early stage SSC initiation and growth. (Rahman, Ohba, Yoshioka, & Yamamoto, 2009, p. 807).

2.4   Detection of signals in noise

2.4.1   Hypothesis testing

Decision theory is a branch of probability theory that describes the process of mapping noise contaminated input data, to a decision regarding the state of a system. Let's consider the data as a random process because some elements in the data source are not describable with certainty. This could for example be the sampled output voltage from an AE-transducer connected to a rolling element bearing. At some point in time, an SSC might be present in the bearing, and thus might excite an AE event. The output voltage of the transducer at a given time will depend on the AE event being present or not (McDonough & Whalen, 1995, p. 152).

Now suppose that we want to determine, or classify, which kind of situation the data originates from. Hypotheses H_i, $i = \{0,1,2,\dots,m-1\}$ define m probabilistic models that describe a distinct system state class. By processing the data x at hand, we want to determine which of the models i was in effect to produce the data. The outcome of the processing is defined as decision D_j, that the data originates from hypothesis H_j. Given the hypothesis H_i, $i = \{0,1,2,\dots,m-1\}$, we want to determine how to arrive at decision D_j, and how well that strategy performs on average.

SSC detection in an RM can be considered as a binary hypothesis-testing problem, meaning that only two hypotheses, H_0 and H_1, cover all the states the machine is expected to inherit. The hypothesis H_0 is typically used as the *null hypothesis*, describing the normal operational condition, and H_1 denotes the *alternative hypothesis*, where a SSC is present. To determine which hypothesis the sampled data belongs to, the data is divided into two regions, R_0 and R_1. The *acceptance region, R_0*, is where we accept H_0 as our hypothesis, and the *critical region*, R_1, is where the we reject H_0, and choose H_1 as true. That is, a decision, D_i, that hypothesis H_i is the current machine state, is made if input data x lies in region R_i. These regions must together include all points in x-space, as any input-data must be given a decision

D. At the same time, no point in x-space can be in more than one region, as this would invoke an ambiguous decision (McDonough & Whalen, 1995, pp. 152-153)

2.4.2 Make a decision

To reach a decision D, a mathematical description on how to process the input data optimally must first be established. This can be done by defining which errors a signal detector can do. A binary hypothesis-testing problem can produce two errors, the false positive, and the false negative. The false positive, or the Type I error, happens when the detector arrives at decision D_1, when the data originates from a machine at state H_0. This is also called a false alarm. The false negative, or the *Type II error*, happens when the opposite is the case. Both errors will be made with some probability $p_{fa} = p(D_1|H_0)$, and $p_{fn} = p(D_0|H_1)$ respectively. Given that this is a binary hypothesis problem, either decision D_0 or D_1 must be produced for every input, thus the probability of crack detection, p_D becomes

$$p_D = p(D_1|H_1) = 1 - p_{fn} \qquad\qquad 4$$

(McDonough & Whalen, 1995, pp. 153-154).

Suppose we are sampling the AE waveform from a rolling element bearing containing a small subsurface defect. Each time a rolling element passes the defect, an AE event message, $m_1 = 1$ is excited. Between rollers, the defect does not excite any AE and the message is then, $m_0 = 0$. We do not know which message that is sent at a given time, and the message m, consisting of m_0 and m_1 is modelled as a random variable with probabilities P_0 and P_1 respectively. In addition to this, we assume that friction, surface irregularities and other noise sources add a zero-mean Gaussian random noise variable n to the waveform. The waveform arriving at the transducer is then the random variable $x = m + n$. If the noise variance is σ_n^2, the two AE messages m_0 and m_1 now correspond to two different probability densities for the sampled data x, as seen in Figure 5. Depending on the original message, x is a Gaussian with variance σ_n^2 and mean of m, being ether m_0 or m_1. That is,

$$p_x(x|m) = \frac{e^{-\frac{(x-m)^2}{2\sigma_n^2}}}{\sqrt{2\pi\sigma_n^2}} \qquad\qquad 5$$

(McDonough & Whalen, 1995, p. 155)

Now we must determine what the optimal decision for any given input would be. One strategy called MAP (maximum a posteriori criterion), dictates that the most probable m, given the input data x, is the optimum choice. Thus choose m_1, if given the input x satisfies $p_m(m_1|x) > p_m(m_0|x)$. Given the probabilities for m, P_0 and P_1, Bayes' rule yields

$$p_m(m_1|x) = \frac{p_x(x|m_1)P_1}{p_x(x)}, \text{ and } p_m(m_0|x) = \frac{p_x(x|m_0)P_0}{p_x(x)}.$$

The decision rule then becomes: Choose $m = m_1$ if the likelihood ratio $L(x) > 1$. That is

$$L(x) = \frac{p_m(m_1|x)}{p_m(m_0|x)} = \frac{p_x(x|m_1)P_1}{p_x(x|m_0)P_0} > 1 \qquad 6$$

This is also called a *detector* (McDonough & Whalen, 1995, pp. 155-156).
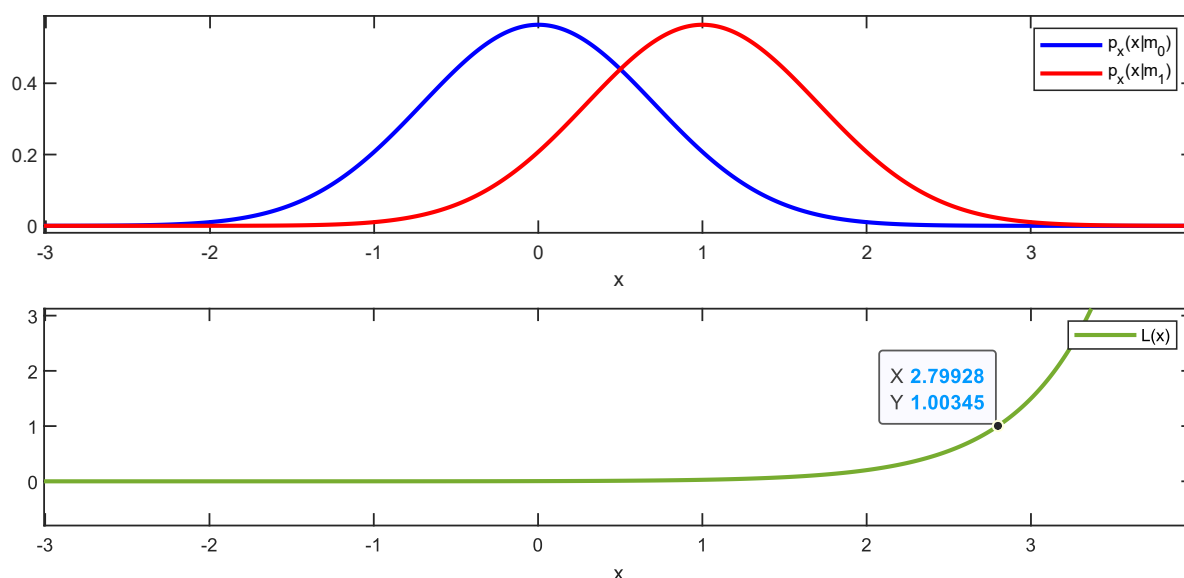
Figure 5, **Top**: Probability density functions of sample space for a binary hypothesis test, given $m_0 = 0$, $m_1 = 1$, and $\sigma_n^2 = 0.5$. **Bottom**: Corresponding likelihood ratio $L(x)$, given $P_0 = 99\%$, and $P_1 = 1\%$. Given these parameters, we choose $m = m_1$ for $x > 2.799$.

2.4.3   The Neyman-Pearson Criterion

In the previous section, the MAP criterion was introduced as our optimal decision-making tool for detection. This is a good criterion to demonstrate the process of decision making in noisy waveforms. However, it implies that we know the probabilities of each hypothesis, P_0

and P_1. In CBM, P_0 and P_1 are unknown. The decision-making in this thesis is therefore based on the Neyman-Pearson (NP) criterion, which has been acknowledged as the most suitable in radar and sonar problems (McDonough & Whalen, 1995, p. 159; Skolnik, 1990, p. 8.2). When using NP, we choose the probability of false alarm, p_{fa} as large as we are willing to tolerate, to minimize the probability of missed detection p_{fn}. Thus, maximizing the probability of detection, p_D. Effectively we decide D_1 if likelihood ratio is equal or greater than T. That is

$$L(x) = \frac{p(x|H_1)}{p(x|H_0)} \geq T \qquad 7$$

where $T = T(p_{fa})$ is set constant or set given one or multiple criteria. In radar detection, T is typically set according to weather conditions. Rain typically induce more uncertainty to the detection problem; thus, T is increased (Skolnik, 1990, p. 8.2).

2.4.4 Defining T

So far, the presented theory describing detection of signals in noise has been relevant to both the radar target detection problem and the crack detection problem in RM. There is however a fundamental difference between the two problems, that is the *time course-dependency*. Probability of target detection, p_D in Radar systems can be considered a Markov process. It does not depend on the past. Consider the detection of an airplane. p_D does not depend on the time of day, nor the total runtime of the radar, if it is in normal working condition. If the airplane is within the radars working range, the most influential factors on p_D, is the distance to the airplane and the weather-condition the moment the radar antenna approaches the sector containing the airplane. However, if the airplane it out of range or the weather condition is bad, we *do not expect* to detect it. This means that the probability of detection can be expressed as $p_D = p_D[r(t), w(t)]$, where $r(t)$ is the distance to the target, and $w(t)$ is the weather conditions, at the time t.

In crack detection in RM, that is induced by RCF, time course is the most influential factor. We do not expect to detect any cracks in an RM that has zero working hours. Operational conditions such as elevated working temperature, loading and component misalignment *only*

matters if the factors have been present over a course of time. If an SSC develops in a RM, it does not go away over time. That is, unlike the radar target detection problem, once a crack has been detected in a RM, it *must* be detectable later. Thus, p_D is expected to be correlated in time. Given these factors, probability of detected cracks can be expressed as $p_D = p_D[f(x_1(t)), f(x_2(t)), \dots, f(x_n(t))]$, where $x_1, \dots x_n$ are the operational conditions at time t, and $f(x_i(t)) = \int_{t_0}^{t} x_i(j)dj$.

Estimating the probability of crack detection in a RM given the integral of the operational condition history, is outside the scope of this thesis. Instead we define a *baseline*. We define T given historic sampled AE data from when the RM were in normal operational state. The amount of historic data used for baselining, is proportional to the expected service life of the RM, and the complexity of the excited AE waveform. If the RM consist of multiple subsystems as pumps, hydraulics etc. the complexity of the excited AE waveforms are expected to increase.

2.4.5   Single-Pulse Detector

So far, we have considered input data, x as a single sampled number. To connect the decision-making theory to the real problem of radar target detection and crack detection in RM, we now consider the input data as a vector of samples $\boldsymbol{x}[i]$, where $i = \{1,2,3, \dots k\}$ and k is the number of samples in x. Consider the message m described in section 2.4.2, but now m consists of either a *pulse,* a vector of $m_1 = 1$, with length, k, or zeros, $m_0 = 0$. The white gaussian noise, n is added the same way as before, and we have $\boldsymbol{x}[i] = \boldsymbol{m}[i] + \boldsymbol{n}[i]$, where each sample in x is an uncorrelated random variable with mean either m_0 or m_1. Using the NP based detector in equation 6, we could make a decision for every entry of x, however a better approach is to first pre-process the data vector, $\boldsymbol{x}$ by taking advantage of what we know about the event. In this case, the optimal pre-processing is to estimate the *mean*. We know that $\boldsymbol{x}$ has a mean of either m_0 or m_1, thus the estimated mean, $\widehat{\mu_x} = \frac{1}{k}\sum_{i=1}^{k} \boldsymbol{x}[i]$ is the optimal pre-processing for $\boldsymbol{x}$ (McDonough & Whalen, 1995, pp. 173-174).

2.4.6 Multiple-Pulse Detector

Pulsed radars transmit and receive a train of equal pulses to determine the range and velocity of a target (Mahafza, 2016, p. 9). The shape and time of excitation of the pulses are known to the radar processing unit. By measuring the time duration from the pulses leaving the antenna to the pulse echoes reach the receiver, the distance to the target can be calculated (Mahafza, 2016, p. 10). The pulses are zero mean; thus, estimating the mean would not work in this case. Instead we take advantage of the fact that the transmitted pulse is *known,* and we can utilize a fully matched filter.

The matched filter output for the input signal $\boldsymbol{x}[i]$, is $\boldsymbol{y}[i]$, which achieves the maximum obtainable SNR for the target echo. The radar transmits N pulses while the rotating antenna illuminates the target, and N signal vectors $\boldsymbol{x}$ are received. Thus, the total matched-filtered signal from a target in the antenna beam is $\boldsymbol{y}[i, k]$ where i is the range index and k is the pulse number. Usually some 1000 range samples are collected per pulse while the number of pulses are below 100. For every range i we now have a multiple pulse detection problem. The NP solution is based on the likelihood ratio and we decide D_1 if it is equal or greater than T. That is

$$L(\boldsymbol{y}[i, 1], \dots, \boldsymbol{y}[i, n]) = \frac{p(\boldsymbol{y}[i, 1], \dots, \boldsymbol{y}[i, N]|H_1)}{p(\boldsymbol{y}[i, 1], \dots, \boldsymbol{y}[i, N]|H_0)} \geq T \qquad 8$$

(Blake, 1986, p. 36).

2.4.7 Pulse Integration

In systems where multiple pulses from a process can be expected to occur, pulse integration can be utilized. When the period from one pulse to the next is predictable, several pulses can be *integrated* to achieve improved detectability of the pulses. That is, a smaller SNR per pulse is required for detection (Blake, 1986, pp. 41-42). For the NP-based detector, the pulse integrating detector is reduced to the square-law detector, where D_1 is decided if the likelihood ratio is equal or greater than T. That is

$$L(y[i]) = \sum_{k=1}^{N} \boldsymbol{y}^2[i, k] \geq T \qquad 9$$

(Skolnik, 1990, p. 8.3) The improved detectability from pulse integration is understood by the fact that integration is a variance reducing process. If N independent noise samples are averaged, the standard-deviation-to-mean ratio of L is reduced by $\sqrt{N}$ relative to the variation of the y_j-s. Thus, the improved detectability from pulse integration primarily dependent on reduced noise, rather than the on the signal enhancement. With the smoothened pulse-noise, the threshold-to-mean ratio can now be reduced while still sustaining the same p_{fa} (Blake, 1986, pp. 41-42). In radar, this process is also called a *video integrator* (Skolnik, 1990, p. 287).

2.4.8   Pulse detection in AE

As described in section 2.3.3, AE-events originated from cracks and crack growth, take form of pulses, or short bursts of energy. Combined with the constantly changing noise of a RM, the result is an AE-waveform with potential crack-originated pulses, hidden in noise. Given the combined transfer function $T_{j\hat{k}}(\omega)$ in equation 3, we know little about the shape-characteristics of a crack originated pulse, and therefore cannot base a detector on a fully matched filter. That is, a fully matched filter will *only* work, if its impulse response is precisely matched to the crack originated AE pulse. According to the radar literature, the alternative solution is the *Envelope Detector*. This detector consists of a bandpass amplifier, a rectifying element, and a lowpass video amplifier (Skolnik, 1990, p. 287). For digital signal processing this is simply: band-pass filter, rectifier, and low-pass filter.

Additionally, AE pulses are expected to occur periodically in an RM. This means that when the rotation frequency is known, pulse integration can also be utilized. We also know that the pulses are short, and broad-banded in the frequency domain. Given this knowledge, the proposed detector for detecting SSC originated AE pulses in an RM is given in section 3.6.1.

2.5   Literature review

2.5.1   Fault diagnosis

Lei et al., (Yaguo Lei et al., 2020), made a thorough review on the past, present and future developments on artificially intelligent fault diagnosis (IFD) in machines. The main areas of

IFD can be divided into three categories: Traditional machine learning (TML)-based IFD, Deep learning (DL)-based IFD, and Transfer learning (TL)-based IFD. In the past (1970s-mid 2000s), TML was the focus in IFD. The methods used, typically incorporated data collection, manual feature extraction and health state recognition (classification). These procedures are typically computationally inexpensive and effective, however they rely heavily on expert knowledge and labeled data (Yaguo Lei et al., 2020, p. 29).
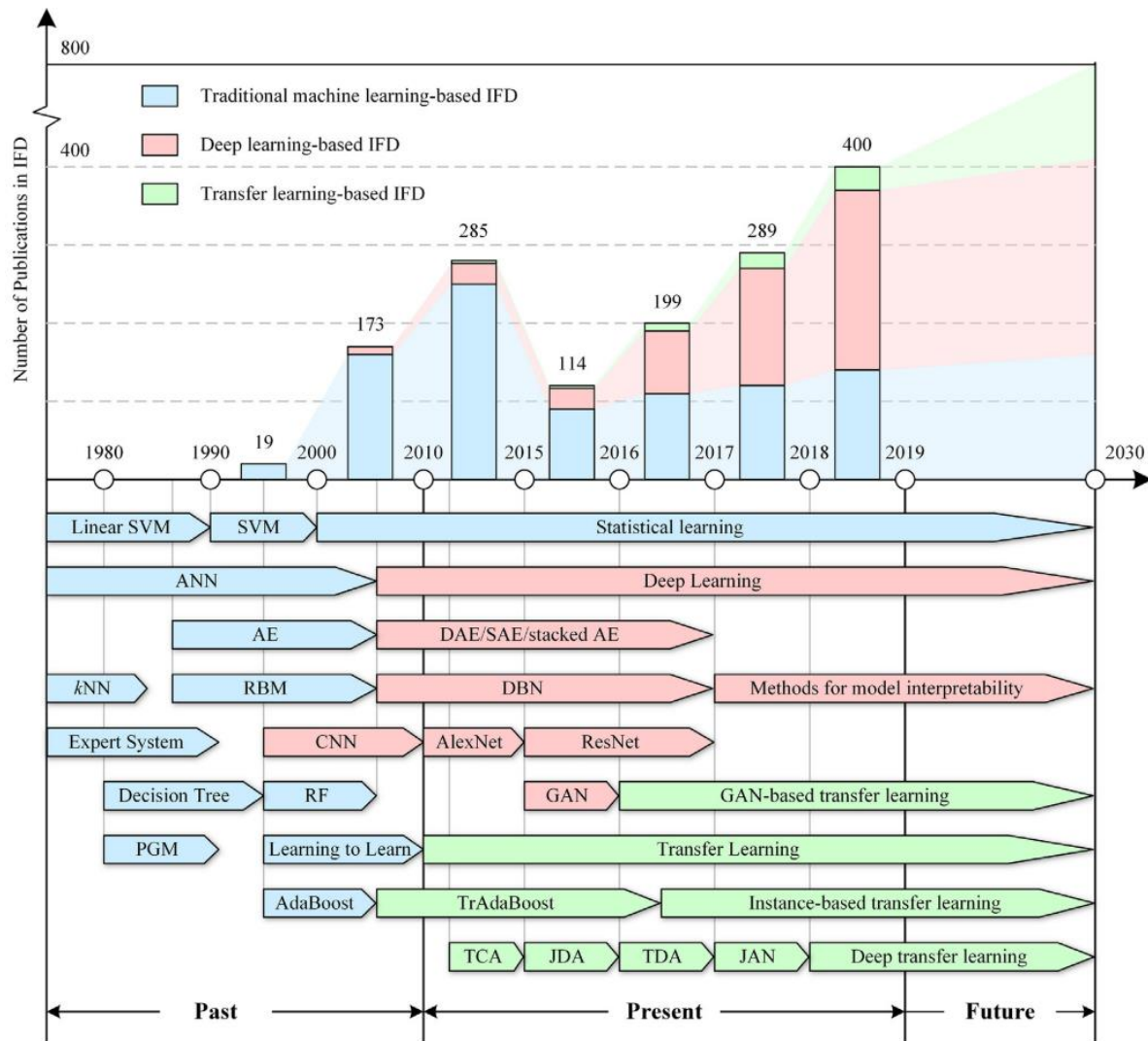
Figure 6, The development of intelligent fault diagnosis (Yaguo Lei et al., 2020, p. 3)

The introduction of DL aimed to mitigate the demand for expert knowledge, by bridging the relationship between the raw monitoring data and the health state of machines. Instead of manually choosing which features to extract from raw data, deep hierarchical architectures represent abstract features automatically, and further establish relationship between the learned features and the target output directly. Although DL models has proved highly

successful in for example computer vision, and to some degree in IFD, they typically rely on sufficient supply of labeled data and complete information about the health state of machines. The final and future solution to this problem, according to Lei et al., is TL. The concept of TL is to reuse knowledge from deep diagnostics models trained on related machines. Diagnostics knowledge gathered from MLBs could for example be used for fault diagnosis in MRBs *if* the diagnosis knowledge could be reused (Yaguo Lei et al., 2020, pp. 13-26, 29).

Out of the 15 research papers based on TL, reviewed by Lei et at., none of them base their research on AE data. Four out of the 443 papers reviewed in the report by Lei et al. base their research on AE. The rest is mainly VA.

2.5.2   AE

The first major study of the AE phenomena was conducted by Kaiser in 1953 (Eitzen & Wadley, 1984, p. 75). 11 years later, the first documented application of the AE technique to an engineering structure was published. During the 1970s, commercial pressure and enthusiasm over the new non-destructive testing alternative led to invalid claims on the underlying workings of the process. The knowledge and understanding of the physical process were still in the early stage and many of the tests conducted were invalid which led to uncritical interpretation of data. However, the method did successfully solve some problems related to leak detection and acceptance testing of fiberglass structures. Being cost-effective, the technique proved to be valuable in monitoring oil and gas pipelines and nuclear power plant components (Eitzen & Wadley, 1984).

2.5.3   Application of AE for RCF induced SSCs in REBs

As mentioned in section 1.1, the published work of (Yoshioka, 1993) is considered the first documented application of AE to detect RCF induced SSCs in REBs. This paper is not reviewed in this thesis, as it could not be obtained before the delivery deadline.

Since the publication from Yoshioka, only a handful of research papers have been published on this topic. There are numerous papers that investigate the use of AE as a *fault detection* tool, but these papers analyse the presence of surface defects *only*. The following sections

review most of the published papers that base their research mainly on the detection of RCF induced SSCs using AE. First, the only paper that successfully used AE to identify the presence of RCF induced SSCs in roller bearings, is reviewed. The next sections review papers that tackle the same problem but lack confirmation of present SSCs. These papers will be referred to as *unverified*. The papers are reviewed in chronological order.

In 2005, (Price et al., 2005) conducted a series loading fatigue tests using a four-ball machine. The first tests lasted about 10-12 minutes before they were stopped when noise from pitting defects could be detected audibly. During testing, continuous recording of AE waveforms were done at an interval of $2.5s$. The length of the recorded segments was equivalent to one ball rotation ($40\ ms$ at $1500\ RPM$). Realtime time-frequency analysis using STFT (Short Time Fourier Transform) was used to manually monitor the sampled AE waveforms during testing. Test 2 and test 3 displayed a distinct change in time-frequency domain after about 7 minutes. In test 2, periodic pulses suddenly appeared, and in test 3, the main frequency energy band suddenly dropped, as seen in Figure 7.

Rolling test FFT results, Test 2, 150–250 kHz   Rolling test FFT results, Test 3, 50–150 kHz
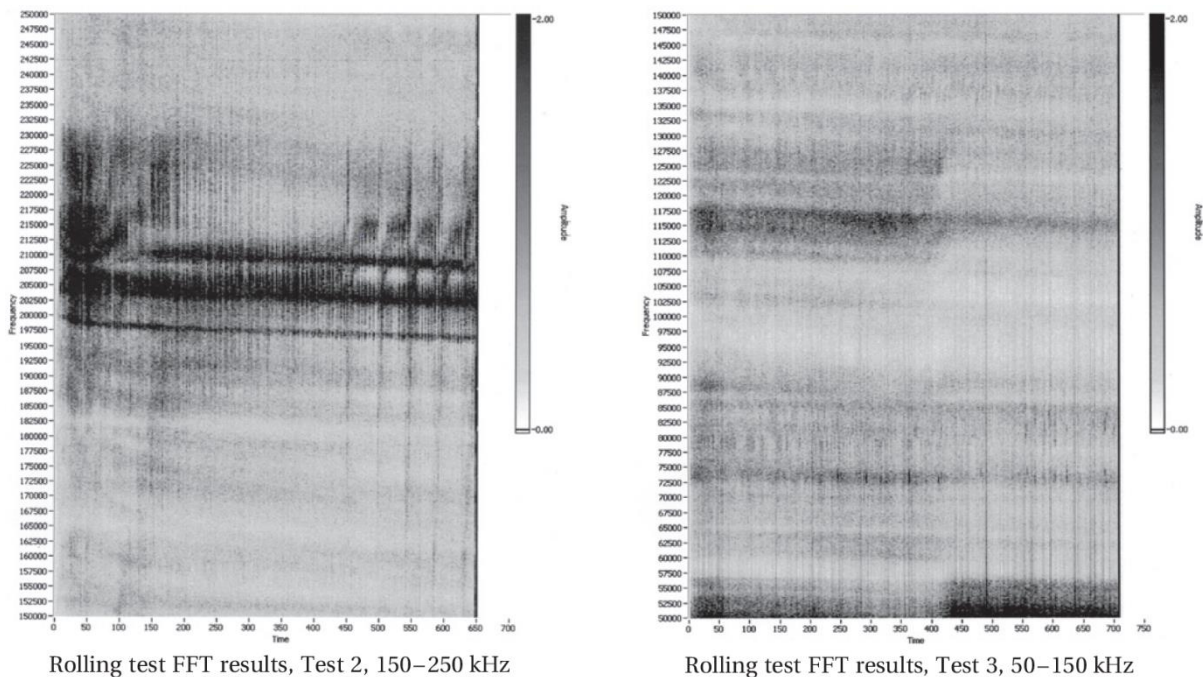
Figure 7, Sudden changes in time-frequency spectrum (Price et al., 2005, p. 94)

In post inspection, the balls were mounted in conductive resin and sectioned through their respective pit defect. The sectioned balls were examined using a scanning electron

21

microscope that revealed SSCs. No additional material change in the area around the SSCs was observed.
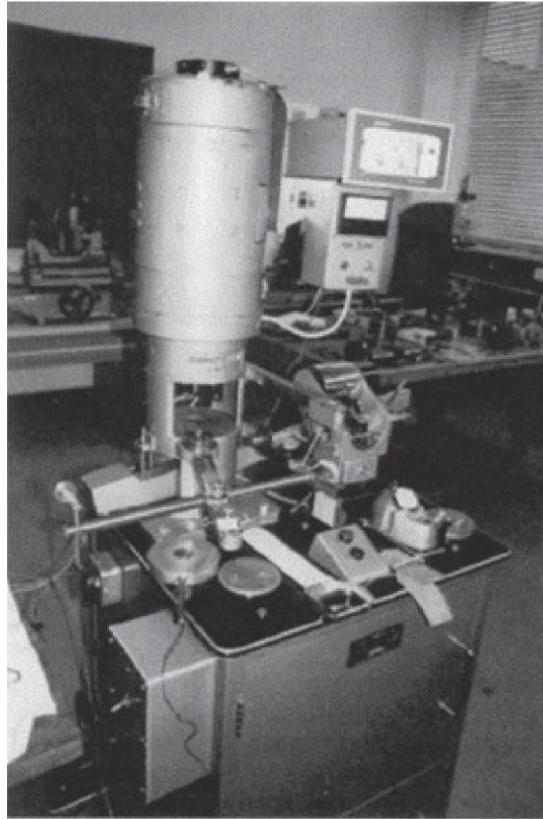
Figure 8, Four-ball machine used in Price' fatigue tests (Price et al., 2005, p. 87)

Two additional tests, Test 4 and Test 5, were then conducted. When similar behaviour change in time-frequency domain was observed, the tests were immediately stopped. Post inspection revealed SSCs in the sectioned balls, but no surface defects, as shown in Figure 9. (Price et al., 2005, p. 95) concludes that if these tests could continue, pitting would initiate in the area of the SSCs. Then, the paper suggests that an automated pattern recognition system based on AE time-frequency data could be used for on-line detection of SSCs formation. The paper does not specify applied contact stress, or fatigue cycle count. Inspection of SSC presence is only done post-testing.

Subsurface crack from Test 4   Subsurface crack from Test 5
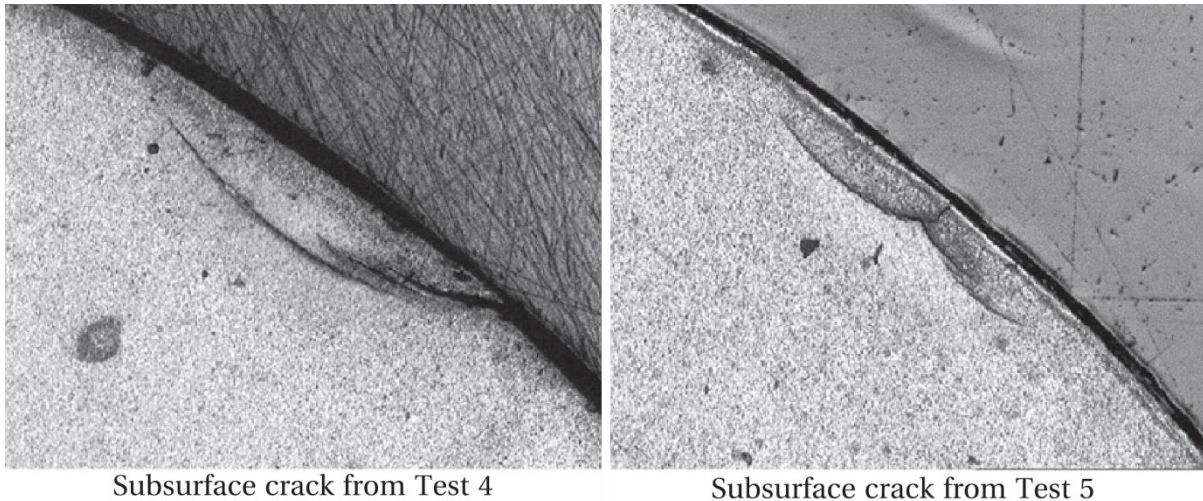
Figure 9, SSCs discovered after Test 4 and Test 5 were stopped due to sudden change in time-frequency AE behaviour (Price et al., 2005, p. 96).

2.5.3.1 Unverified

(Elforjani & Mba, 2010) investigated accelerated natural degradation of a bearing race. To decrease the fatigue life of the bearing, one bearing race of a thrust *ball* bearing was replaced by a bearing race of a thrust *roller* bearing, thus achieving higher contact stresses. Visual inspections of the test specimen bearings are done periodically. Data analysis is done through time-domain analysis, frequency-analysis, and time-frequency analysis. The paper concludes that there is a clear correlation between increasing AE energy levels and the natural propagation and formation of bearing defects. However, the paper express that the method presented for identification of onset crack propagation cannot be used on real operational bearings, but possibly be used as a quality control tool for manufacturers. No subsurface inspection is done to verify the presence of SSCs.

(Quiney, Lees, Ganji, & Murray, 2012) investigated in 2012 the potential advantages AE represent in early fault detection, compared to VA. Fatigue tests were conducted using a four-ball machine. The tests lasted from 7 to 116 hours and were stopped when a vibration triggered alarm indicated spall defects in the fatigued components. Maximum contact stress during testing was kept constant at $6.31 GPa$ and the rotation frequency on the top ball was fixed at $1500 RPM$. AE waveforms were continuously recorded at $f_s = 5MHz$ with length of $0.64\,s$ at $3\,s$ intervals, or $1.6\,s$ at $5\,s$ intervals. For signal processing they used the Hilbert transform to decompose the sampled AE waveforms. The components corresponding to the

distinct failure frequencies of the 4-ball machine were then converted to frequency power spectrums. From the power spectrums, they could detect sudden changes in amplitude approximately $30\ s$ before the machine stopped due to spall induced vibration. The paper concludes that the cause of the sudden increase in AE activity -*clearly indicate the presence of a subsurface fault* (Quiney et al., 2012, p. 135). The paper does not specify the total number of fatigue cycles accumulated for each test. No subsurface inspection is done to verify the presence of SSCs.

(Esmaeili, Zuercher, Wang, Harvey, & Holweger, 2017) researched the formation of white etching cracks (WECs) on the subsurface of bearings. Electrical and mechanical (axial) load is applied during testing. Time-frequency (STFT) analysis is used to monitor the fatigue development during roller testing. Results are interpreted directly from the time-frequency recorded data, and no feature extraction is done. The paper concludes that AE can be used to detect the signatures of WECs in the frequency band $0 - 20\ kHz$. No subsurface inspection is done to verify the presence of subsurface WECs.

(Fuentes et al., 2020) presented a method for identifying seeded subsurface- and early-stage surface defects in ball bearings using AE. Surface defects was made using either using spark erosion or scratching with Cubic Boron Nitride. The subsurface defects where artificially made by applying load to compress the outside surface of a bearing raceway with a rolling element. Hertzian contact mechanics dictated that subsurface yield would occur at $1000\ kN$, and the raceway was subjected to loads of maximum $2000\ kN$. The presence of subsurface cracks was observed with AE-*hit* monitoring during compression. To detect the defects present in the AE waveforms, TML is used. Features are extracted manually from time-domain only. Data selection is hit-based, meaning that only bursts/pulses in the recorded waveforms are stored for feature extraction. To identify the hits from the constantly changing noise floor of a rotating machine, a moving RMS hit identification function is used. For classification Gaussian mixture models is used. Sampling frequency is $f_s = 1MHz$. Testing parameters such as fatigue cycle count, contact stress, and test duration are not described. No subsurface inspection is done to verify the presence of SSCs.

3 Methodology, materials, and experimental setup

3.1 Duration test

The data used for analysis in this thesis is gathered from one duration test, completed during the master's period. A purpose-built test machine located at Materialteknisk (MTI), NTNU was used for the entire test. The objective of the test was to generate RCF induced SSCs in a test specimen roller. This is achieved by replicating the loading conditions typically present to rolling elements inside a REB during operation. The test was completed in stages. During each stage, contact stress on the test specimen, and rotation frequency, f_r were kept constant.

Between each stage, a PAUT (Phased Array Ultrasonic Test) was conducted to monitor SSC development and propagation. The PAUT equipment used was an Olympus OMNISCAN sx (Appendix K). All relevant information collected during the test was logged in a spreadsheet. This spreadsheet will be referred to as the "test-log." A compressed version of the test-log is presented in Table 2.

From the test start 2021 Mar 16, F_A (specified in formula 10) was kept constant at $F_A = 364\ RPM$. April 19, 2021, due to excessive vibration in the machine, F_A was reduced to $F_A = 256\ RPM$.

3.2 Test machine
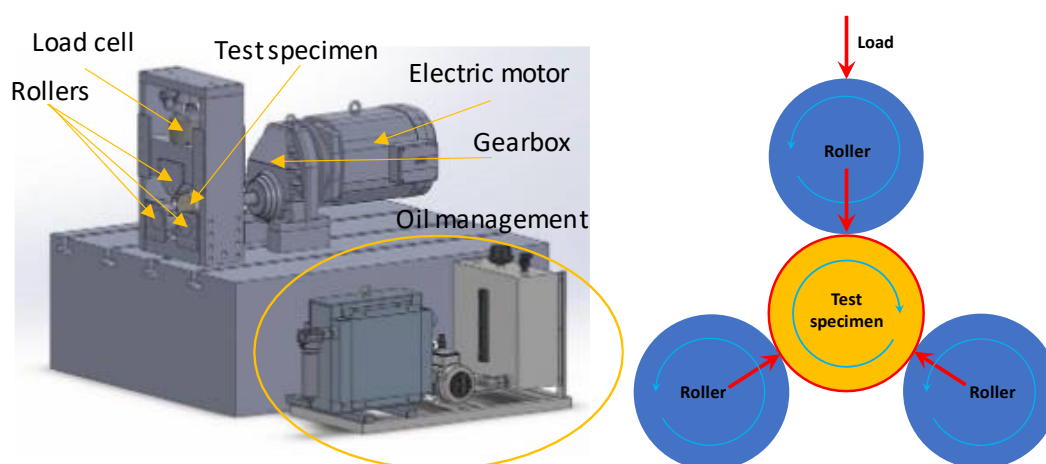
Figure 10, **Left**: Cad drawing of the test machine. **Right**: Arrangement of support rollers and test specimen.

The general layout of the test machine is displayed in Figure 10. A 22 kW SEW electric motor drives the whole arrangement. It is connected to a 375:128 reduction gearbox which is directly coupled to the test specimen with a flexible shaft coupler. Three rollers support the test specimen, and each roller is supported by two needle bearings as seen in Figure 11. The specification for the needle bearings can be found in Appendix C. Support roller dimensions can be found in Appendix A. A load cell controlling the contact stress between the rollers and test specimen acts on the top support roller. The contact stress distributed between the three contact points are assumed equal due to the symmetrical 120° angle between the centre of each support roller and the centre of the test specimen.

Due to the arrangement of the test specimen and the support rollers, one point on the perimeter of the test specimen passes three contact points (support rollers) per rotation. Thus, three fatigue cycles occur per axle rotation. The corresponding "test frequency," is thus defined as

$$f_{test} = 3f_r,$$ 10

where $f_r = \frac{F_A}{60}$,

and F_A is the axle rotation frequency in RPM.
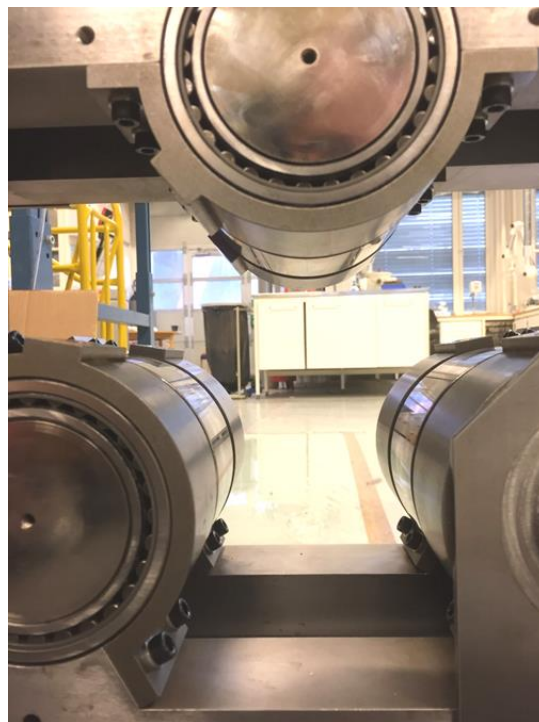
Figure 11, Support rollers and needle bearings.

3.3 Recording systems and sensors
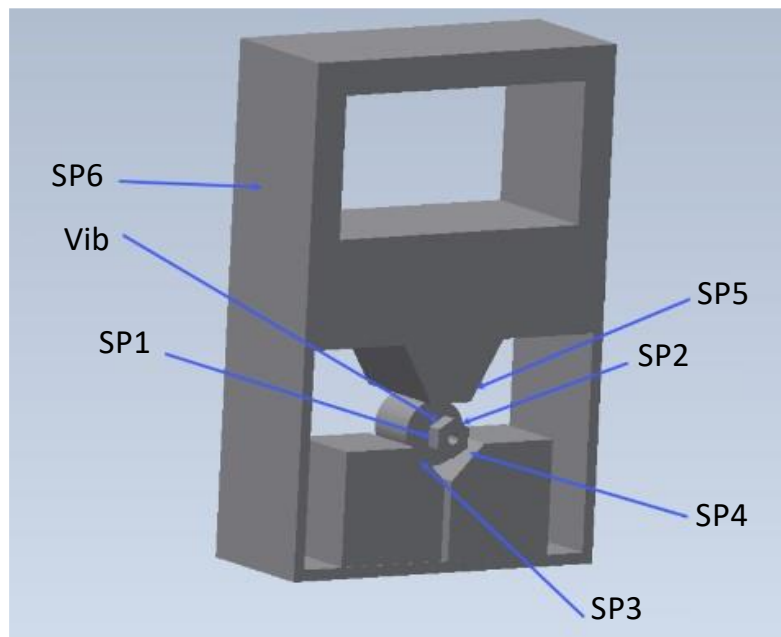
Figure 12, Test machine sensor location layout. SPx refers to sensor position x.

There are two separate systems recording the AE-waveforms during testing, the NTNU (MISTRAS) system, and the Kongsberg Maritime (KM) system. MISTRAS records AE waveforms from the sensor at SP1, and KM records AE waveforms from the sensors at SP2-SP5. The sensor at SP6 and the Vib sensor were not used for analysis in this thesis.

An axle pin is bolted to the test specimen on the opposite side from the shaft coupler, as seen in Figure 13. SP1 and SP2 are on a linear bearing mounted to the axle pin. Specifications of the linear bearing can be found in Appendix . SP3-SP5 are on the front needle bearing housings, as seen in Figure 14. The linear bearing, needle bearings, and the contact points between the test specimen and support rollers are all lubricated with gear oil supplied from the oil management system seen in Figure 14. The contact medium used between the sensors and the contact surface is a high temperature paste from FUCHS, named GLEITMO 591 (Appendix M).

The AE sensor in SP1-SP2, is the WD sensor by PHYSICAL ACOUSTICS.

> *WD is a true differential wideband sensor with a very high sensitivity and bandwidth. It has a very good frequency response over the range of 100-900 kHz. Differential*

sensors differ from their general purpose counterparts by employing two sensing elements with opposite polarization directions. The two signal leads feed into a differential pre-amplifier which eliminates common-mode noise resulting in a lower noise output from the pre-amplifier (Appendix).

The AE sensor in SP3-SP5 is the Micro30D by Physical Acoustics.

MICRO30D is a differential sensor designed to isolate the sensing terminals electrically from the cavity. This electrical isolation makes the sensor particularly useful for applications where high background electrical noise is a major concern. It has a very good sensitivity and frequency response over the range of 150 – 400 kHz. The two signal leads from the sensing element feed into a differential pre-amplifier which eliminates common mode noise resulting in a lower noise output from the pre-amplifier (Appendix).
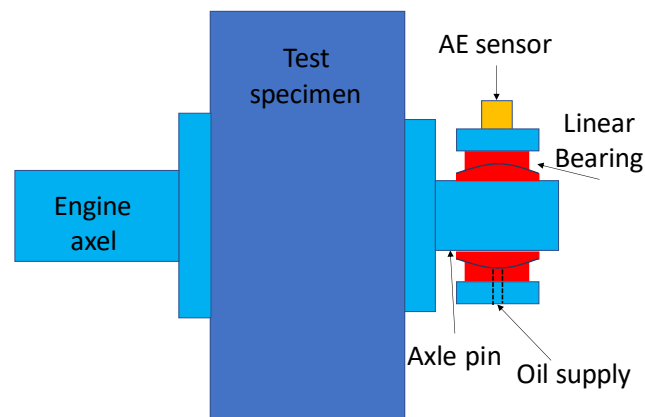
Figure 13, Layout for the test specimen, SP1 and SP2.
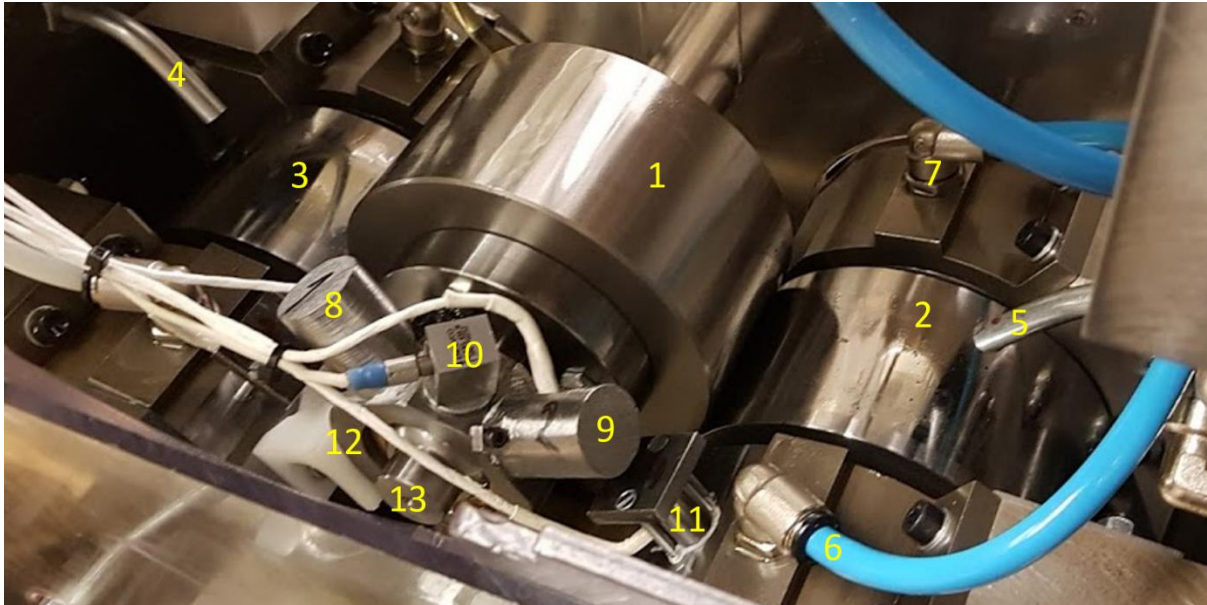
Figure 14, Test machine components **1**: Test specimen, **2**: Right support roller, **3**: Left support roller, **4**: Left oil-splash, **5**: Right oil-splash, **6**: Oil supply, front right needle-bearing, **7**: Oil supply, back right needle-bearing, **8**: SP1, WD-sensor (MISTRAS), **9**: SP2, WD-sensor (KM), **10**: Vib (KM), **11**: SP4, Micro30D-sensor (KM), **12**: Linear bearing, **13**: Axle pin.

3.4   Test specimen

Only one test specimen was used through the entire duration test. It is made from case hardened gear steel with a surface hardness of approximately 700 Vickers. Case hardening means that only the outer perimeter is fully hardened, and the core is not. Given the theory on RCF induced SSCs in section 2.2, the intention of the case hardening is to increase the probability of SSCs to be the first occurring failure mode. Dimensions and tolerance for the test specimen can be found in Appendix B.

3.5   Signal Equipment used

3.5.1   **Mistras (NTNU)**

A low-noise wide band preamplifier, PAC 2/4/6 by PHYSICAL ACOUSTICS (MISTRAS) was used to amplify the signal from the WD sensor by $40\ dB$, and bandpass filtered in the frequency band $50\ kHz - 1300\ kHz$. Information about the PAC 2/4/6 can be found in Appendix . The signal was then passed on to a 2-channel PC-controlled AE-recording system based on the PCI-2 data acquisition board by PHYSICAL ACOUSTICS (MISTRAS) with

continuous data streaming capability. Information about the PCI-2 can be found in Appendix
.

During testing, continuous AE waveform segments of 10 seconds length were recorded at an interval of 10 minutes. After the first SSC was confirmed in PAUT, the interval was reduced to 5 minutes. The AE recording was performed continuously, with a sampling frequency, $f_s = 2MHz$ and a bit depth of 16 bits per sample.

Software used for recording is AEwin by PHYSICAL ACOUSTICS (MISTRAS). Information about AEwin can be found in Appendix . Recorded AE segments were saved in .wfs format. These .wfs-files cannot be easily opened outside the AEwin environment. A wfs-reader MATLAB-script was provided by the supervisor to open the AE waveforms in the MATLAB-workspace. Further analysis on the waveforms could then be performed.

The files names were on the format *RT8-QyyyyMMdd-HHmmss-000.wfs*. *yyyy* is year, *MM* is month, *dd* is day, *HH* is hour, *mm* is minute, *ss* is second and *Q* is a counter. To avoid any confusion regarding which SPx the file originates from the file was renamed to RT8-*QyyyyMMdd-HHmmss-00x.wfs*, where *x* refers to SPx.

A total $360GB$ of raw data, gathered by the Mistras system, is used for further analysis.

3.5.2 KM (Kongsberg Maritime)

The same preamplifier, PAC 2/4/6, is used in the KM system with 40 db gain, and bandpass filtered in the frequency band $20kHz – 1200kHz$. The signal was the passed on to 12 channel high-speed acquisition board that is, Kongsberg HSIO-100-A (Appendix).

During testing, continuous AE waveform segments of 2 seconds were recorded at an interval of 60 minutes. After PAUT confirmed the first SSC, the interval was reduced to 20 minutes. The AE recording was performed continuously, with a sampling frequency, $f_s = 2MHz$, and a bit depth of 24 bits per sample. Recording is automatically started when the F_A is greater than a threshold. 2021 Apr 19, when the F_A was lowered due to vibrations (as mentioned in 3.1), it was lower than the threshold, and no recording was done until the threshold was lowered 22 April, 2021.

Recorded AE segments were provided in .csv format, which can be opened directly in the MATLAB workspace. The csv files contained either data from SP2 only, or SP3-SP5. The files names were on the format *dd.MM.yyyy-HH.mm.ss.csv*. *dd* is date, *MM* is month, *yyyy* is

year, *HH* is hour, *mm* is minute, and *ss* is second. As the data from MISTRAS was the first data used for analysis, the csv-files containing sensor-data from SP2 only were renamed to match the MISTRAS filename-syntax. Csv-files containing sensor-data from SP3-SP5 were first opened in MATLAB, then the data corresponding to each SPx was saved in separate .mat-files with filenames corresponding to MISTRAS filename-syntax. This was done to reduce file-loading time, as the three .mat files corresponding to one .csv file use 1/16 the space on the SSD (Solid State Drive).

A total $292GB$ of raw data, gathered by the KM system, is used for further analysis. For both systems put together, a grand total of $652GB$ of raw data is used for further analysis. The total number of files used for analysis from each SPx is listed in Table 1.

Sensor position	Number of files
SP1 (MISTRAS)	9324
SP2 (KM)	2350
SP3 (KM)	442
SP4 (KM)	442
SP5 (KM)	442

Table 1, Number of files used for analysis.

3.6   Procedures and algorithms

3.6.1   Proposed Detector

A method for detecting SSC originated AE pulses in RM is introduced in this thesis. The core principle of the detector is derived from established theory used to solve the *radar target detection problem*. This is reviewed in section 2.4. The main advantage to the detector lies in the use of pulse integration. Pulses are first extracted from the sampled AE waveform at precise intervals, defined by a window function. The extracted pulses are then integrated. *If* the result of the pulse integration contain defect originated pulses, it will have a higher value than if the data only contains noise. The detector is developed in the MATLAB environment, thus all sets and matrices describing the computational procedures are *one*-base-indexed.

31

3.6.1.1 The Sampled AE Waveform

Let $x[n]$ be the sampled AE waveform of length l_{signal}, where $n = \{1,2,3,\dots,l_{signal}\}$. Figure 15 displays an example of what the raw sampled waveform $x[n]$ can look like. The waveform is recorded on MISTRAS, 2021 May 18, 17:43:30, and will be used for demonstration purposes throughout this section. The recording contains AE pulses repeating at $f_{fault} = 3/rev$ and $f_{fault} = 1/rev$, where f_{fault} denote the number of times per axle rotation a defect originated AE pulse is expected to occur.
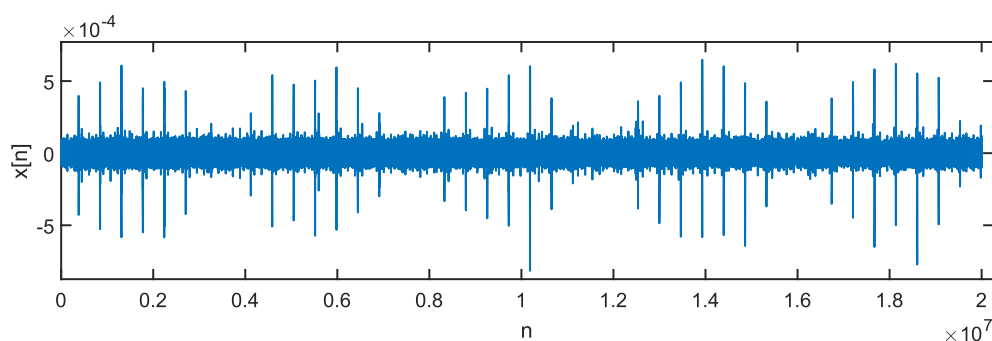

Figure 15, An example of $x[n]$, sampled at $f_s = 2\ Mhz$ for a period of $l_{signal} = 10s f_s$. Pulses repeating at $f_{fault} = 1/rev$ are visible as peaks in $x[n]$.

3.6.1.2 Determine starting position of all recorded axle rotations

The first step is to estimate all window positions. These can be calculated using the rotation frequency, f_r at the time of the recorded waveform x, and is the chosen method for this thesis. For now, it is assumed that the exact rotation frequency, f_r of the RM during a recording, is known. To calculate the position of all windows, an estimated relative starting position for every axle rotation is needed. However, this implies that the f_r is kept constant through the entire recording, which is unlikely. The ideal way to calculate window positions, would be to use axle position data sampled simultaneously with the AE sampling. This was unavailable during the development of the detector. Thus f_r is estimated from x instead.

The following sections describe the *general,* ideal detector solution, which accounts for an unstable rotation frequency, f_r during an AE recording. This solution choice will be discussed further in 6.1.6.

Let r_m denote the starting positions of the recorded axle rotations, and f_{fault} denote the number of times between r_m and r_{m+1} a defect originated AE pulse is expected to occur.

To correctly detect every defect behavior in an RM, a generalization of f_{fault} is needed. That is

$$f_{fault} = \begin{cases} k/rev, k \in \mathbb{N} & , case1 \\ k/rev, k \notin \mathbb{N} & , case2 \\ k\ Hz, k \in \mathbb{R} & , case3 \end{cases} \qquad 11$$

Where case:

1- A defect excites an AE pulse an integer number of times per axle revolution.
2- A defect excites an AE pulse a fraction number of times per axle revolution.
3- A defect excites an AE pulses with a rate unrelated to f_r.

For $f_{fault} = k/rev,\ k \in \mathbb{N}$, r_m becomes

$$r_m = \{0,1,2,\dots,m-1\}\left\lfloor\frac{f_s}{f_r}\right\rfloor + 1, \text{ where } m = \left\{1,2,3,\dots,\left\lfloor\frac{l_{signal}f_r}{f_s}\right\rfloor\right\} \qquad 12$$

For $f_{fault} = k/rev,\ k \notin \mathbb{N}$, then the AE pulses will not occur at one distinct axle position from one axle rotation to the next. Instead of denoting r_m as the axle starting position, r_m now denotes every g-th AE pulse. Given $g = 10$, 10 pulses are expected to occur between r_m and r_{m+1}.

$$r_m = \{0,1,2,\dots,m-1\}\left\lfloor\frac{f_s g}{f_r f_{fault}}\right\rfloor + 1, \qquad 13$$

$$\text{where } m = \left\{1,2,3\dots,\left\lfloor\frac{l_{signal}f_r f_{fault}}{f_s g}\right\rfloor\right\}, \text{ and } g \in \mathbb{N} > 1$$

g is an integer that must be more than one to in order to prevent round-off error. For PIS verification (ref section 3.6.2) g is it kept at $g = 4$.

For $f_{fault} = k\ Hz, k \in \mathbb{R}$, where the AE pulses repeat with a rate unrelated to f_r, r_m becomes

$$r_m = \{0,1,2,\dots,m-1\}\left\lfloor\frac{f_s g}{f_{fault}}\right\rfloor + 1, \qquad 14$$

$$\text{where } m = \left\{1,2,3\dots,\left\lfloor\frac{l_{signal}f_{fault}}{f_s g}\right\rfloor\right\}, \text{ and } g \in \mathbb{N} > 1$$

The length of each rotation in samples, d_s is

$$d_s = r_{s+1} - r_s, \text{ where } r_s = \{r_1, r_2, \dots, r_{m-1}\}, \tag{15}$$
$$\text{and } s = \{1, 2, 3, \dots, m-1\}$$

When defining the set, d_s from a constant f_r, every entry in d_s are equal. Thus, the general solution is excessive in this case and d_s could be replaced by the constant d. However, d_s is used to give a more complete representation of the detector.
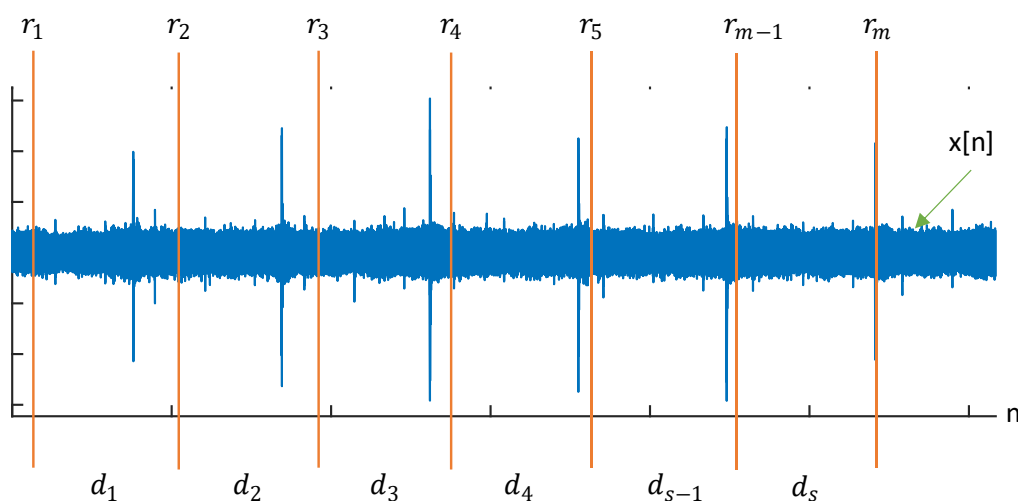
Figure 16, $x[n]$ with calculated rotation start positions r_m, and rotation durations d_s.

3.6.1.3 *Define windows*

Given r_s, and d_s, the window function is defined as a window of sub-windows. That is

$$w_{j,s}^i[n, l_w, o_w] = \begin{cases} 1 & p_{j,s}^i[l_w, o_w] \leq n \leq p_{j,s}^i[l_w, o_w] + l_w \\ 0 & otherwise \end{cases}, \tag{16}$$

where position, $p_{j,s}^i[l_w, o_w] = r_s + (l_w - o_w)i + \dfrac{d_s}{f_{fault}}j$,

$i = \left\{0, 1, 2, \dots \left\lceil \dfrac{d_s}{f_{fault}} \right\rceil - 1\right\}, j = \{0, 1, 2, \dots f_{fault} - 1\}$,

l_w is the window length, and o_w is the window overlap.

Figure 17, $x[n]$ with illustrated windows. The green rectangles illustrate the sub-windows of the first window, that is $w_{j,s}^0[n, l_w, o_w]$, and the purple rectangles illustrate the sub-windows of last the window, that is $w_{j,s}^{max(i)}[n, l_w, o_w]$, with a failure rate, $f_{fault} = 1$.

To clarify how the sub-windows of a window are distributed in n-space, consider this example:

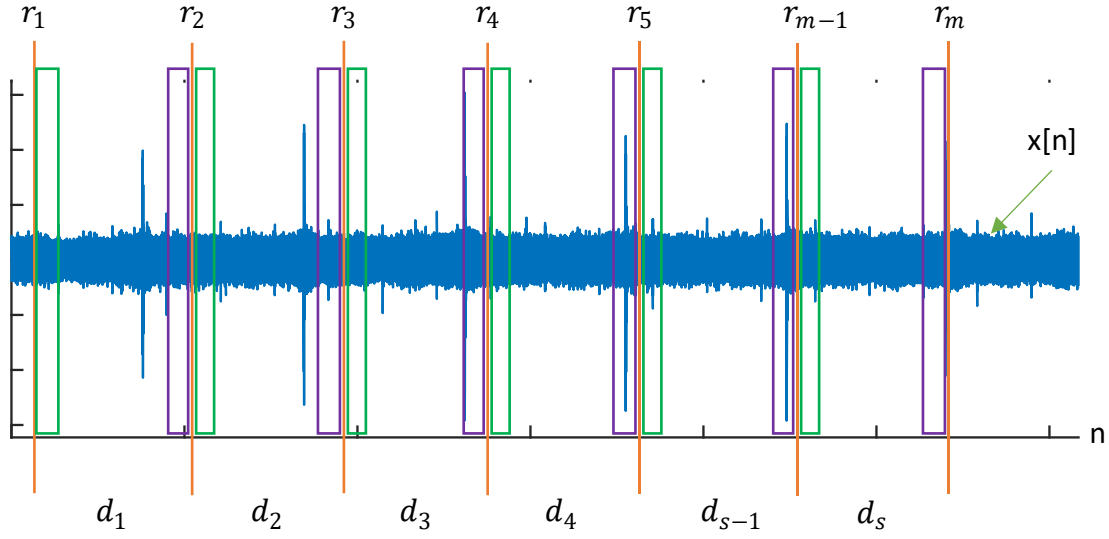> A sampled waveform $x_1[n]$ has a recorded 11 axle start-positions. That means that there are 10 full axle rotations recorded in $x_1[n]$. We want to detect a defect that excites AE pulses at $f_{fault} = 3/rev$. That means a total 30 AE pulses are recorded in $x_1[n]$. The corresponding window function thus consist of windows with $max(s)(max(j) + 1) = 30$ sub-windows, where $max(s) = 10$, and $max(j) = 2$.

3.6.1.4 Pulse Extraction-and Integration

With the window positions calculated, the pulses in each window $y_{0,1}^0, \dots, y_{j,s}^i$ can now be extracted. As described in section 2.4.8, $x[n]$ cannot be matched-filtered to maximize the SNR for the AE pulses, because the AE pulse shape is unknown. Instead, the pulses are extracted using an envelope detector. As further described in section 2.4.8, the envelope detector consists of a band-pass filter, a rectifier, and a low-pass filter.

The bandpass filter is used for rejecting noise outside the AE pulse frequency band. In RM AE monitoring it can be necessary to attenuate the lower part of the frequency band due to

high noise level. The test machine used to generate AE waveforms in this thesis, had a constant noise frequency band between $0 - 500 \, kHz$. Therefore, $\boldsymbol{x}[n]$ is filtered using a high-pass filter with cut-off frequency at $500 \, kHz$ to attenuate most of the RM originated noise. $\boldsymbol{x}_{HP}[n]$ denotes the high-pass filtered $\boldsymbol{x}[n]$. The built in MATLAB function *highpass* (MATLAB, 2021d) was the chosen filtering-function. In Figure 18, the spectrograms of $\boldsymbol{x}[n]$ and $\boldsymbol{x}_{HP}[n]$ are presented. The spectrograms are generated using the built in MATLAB function *pspectrum* (MATLAB, 2021f).
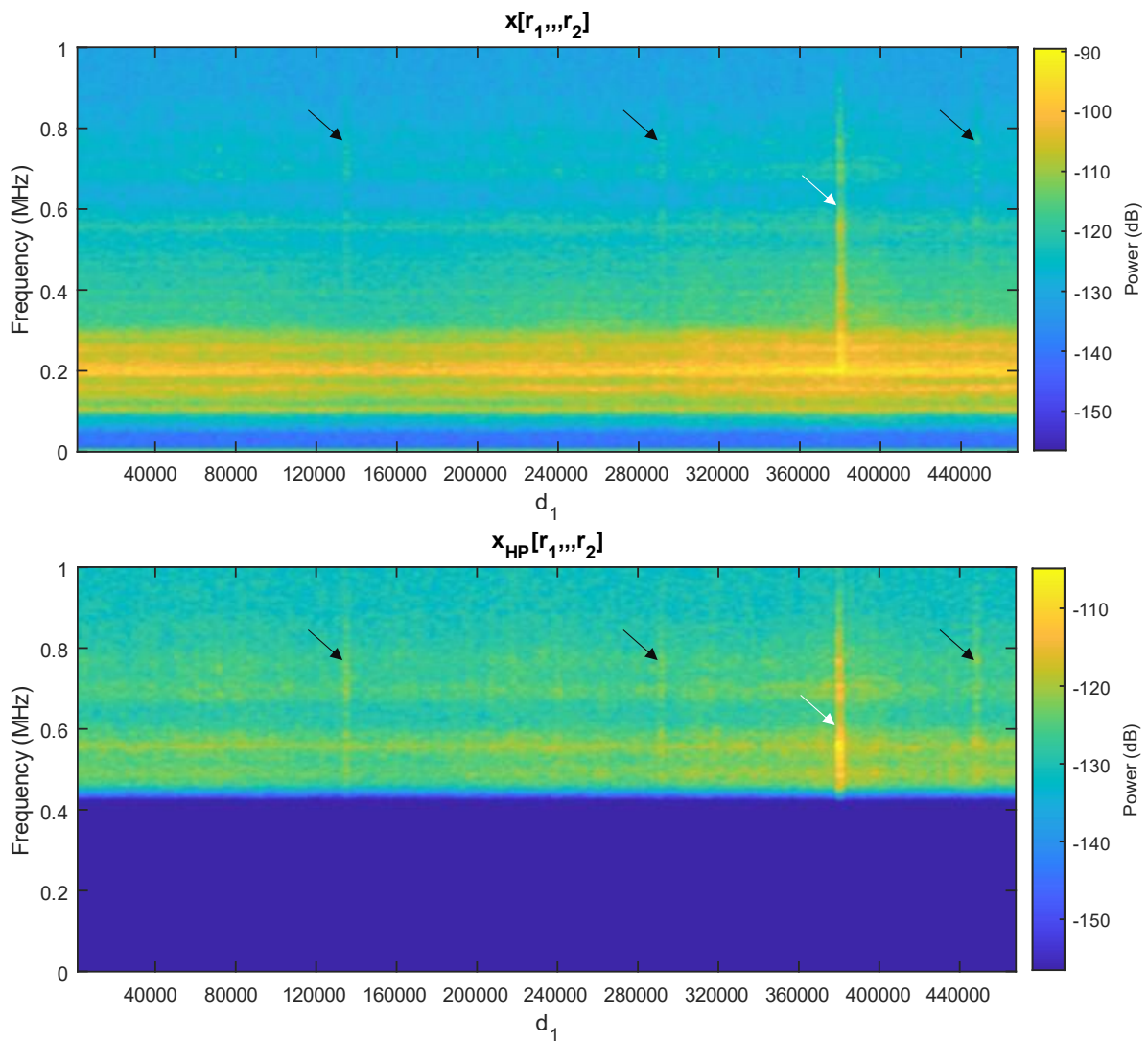

Figure 18, The spectrogram of $\boldsymbol{x}[n]$ and $\boldsymbol{x}_{HP}[n]$, plotted between $n = r_1,,,r_2$, given $f_{fault} = 3/rev$. The black arrows indicate the AE pulses repeating at $f_{fault} = 3/rev$, and the white arrows indicate the AE pulses repeating at $f_{fault} = 1/rev$. NB, this is an ordinary spectrogram and must not be confused with the PIS (ref section 3.6.2).

The chosen rectifying element for the envelope detector is to square $x_{HP}[n]$, that is, $x_{HP}^2[n]$. This is the rectifier that produced the best results.

The low-pass filter is to sum all the squared samples inside the window. This summation is effectively a low pass operation. The extracted pulses are thus calculated

$$y_{j,s}^i[l_w, o_w] = \sum_{n=1}^{l_{signal}} w_{j,s}^i[l_w, o_w, n] x_{HP}^2[n] \qquad\qquad 17$$

Equation 17 can be simplified by describing $y_{j,s}^i[l_w, o_w]$ as a matrix, $\boldsymbol{M}_{i,r}$, where the entries of each row is the extracted pulse from each sub-window in window i. By referring to Figure 17: The green rectangles would correspond to the first row, $\boldsymbol{M}_{0,r}$, and the purple rectangles would correspond to the last row, $\boldsymbol{M}_{max(i),r}$. That is

$$\boldsymbol{M}_{i,r} = \begin{pmatrix} y_{0,1}^0 & y_{1,1}^0 & \cdots & y_{j-1,1}^0 & y_{j,1}^0 & y_{0,2}^0 & \cdots & y_{j-1,s}^0 & y_{j,s}^0 \\ y_{0,1}^1 & \cdots & \cdots & \cdots & \cdots & \cdots & \cdots & \cdots & y_{j,s}^1 \\ \vdots & \cdots & \cdots & \cdots & \cdots & \cdots & \cdots & \cdots & \vdots \\ y_{0,1}^{i-1} & \cdots & \cdots & \cdots & \cdots & \cdots & \cdots & \cdots & y_{j,s}^{i-1} \\ y_{0,1}^i & \cdots & \cdots & \cdots & \cdots & \cdots & \cdots & \cdots & y_{j,s}^i \end{pmatrix}, \qquad 18$$

where $r = \{0,1,2,\dots, s(j+1) - 1\}$.

3.6.1.5 Outlier removal

All entries in one row are expected to be close in value. Either the window is in position of the pulse, and is detected in most sub-windows, or it is not. If only a small number of sub-windows give a higher value than the rest, that means that these sub-windows detect other AE pulses than what we are looking for. These are *outliers* and must be removed before proceeding.

Let the row vector N_i with length r, be the i-th row in $\boldsymbol{M}_{i,r}$. The entries in N_i considered outliers are set to the *mean* of the entries in N_i *not* considered outliers. This is done for all i's. In MATLAB notation this becomes

$$N_i[isoutlier\{N_i\}] = mean\{N_i[\sim isoutlier\{N_i\}]\} \qquad\qquad 19$$

Where isoutlier(A) is a built-in function in MATLAB that returns the indices of the entries in vector A that is more than three scaled median absolute deviations (MAD) away from the median(A). mad(A) is defined as $c \cdot median\left(abs\left(A - median(A)\right)\right)$, where $c = -\frac{1}{\sqrt{2}}erfcinv\left(\frac{3}{2}\right)$ (MATLAB, 2021e), and $erfcinv$ is the inverse complementary error function (MATLAB, 2021b). Now, $\widetilde{M}_{i,r}$ is denoted as the row-outlier-free matrix.
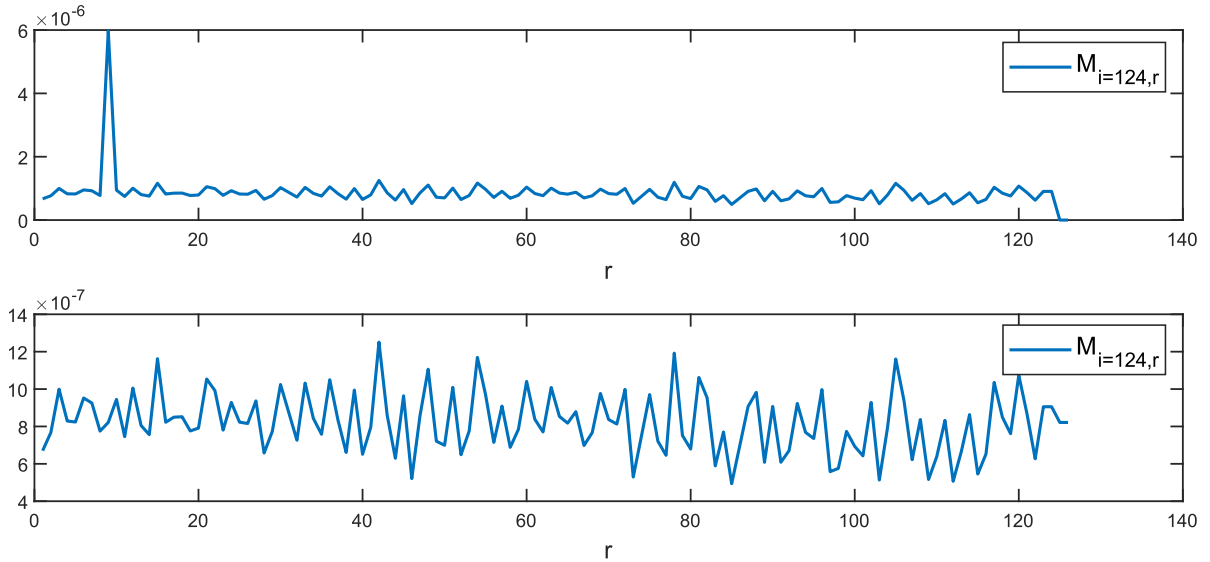
Figure 19, **Top**: The 124-th row of $\boldsymbol{M}$ (before outliers are removed) plotted with respect to r. At $r = 9$, there is a clear outlier. **Bottom**: The same row is plotted, but now the outliers are removed.

With the row outliers removed, pulse integration is done by summing the squares of each row in $\widetilde{M}_{i,r}$, that is

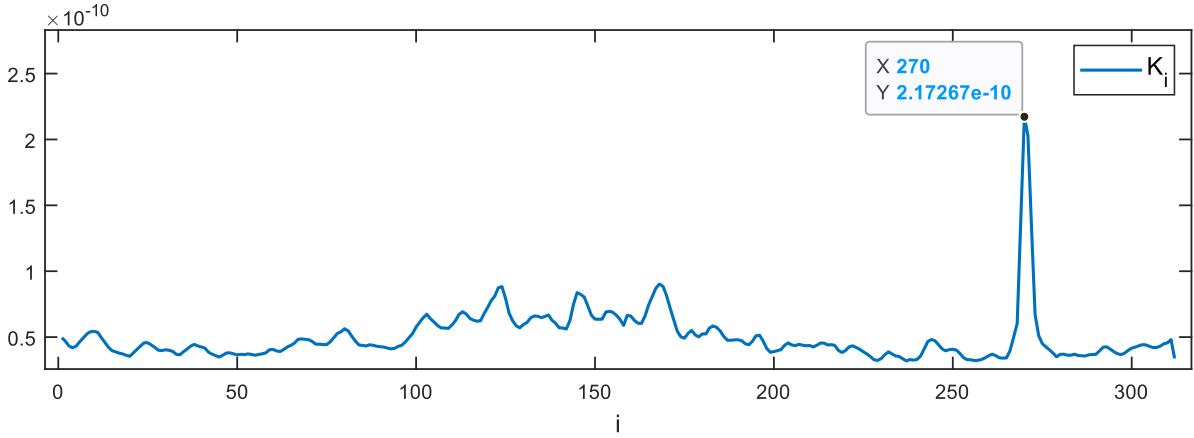$$K_i = \sum_{r=0}^{s(j+1)-1} \left(\widetilde{\boldsymbol{M}}_{i,r}\right)^2 \qquad 20$$

Figure 20, K_i plotted with respect to i. This will be referred to as the *K-spectrum*. Defect related AE-pulses will be present in the K-spectrum as peaks. The peak corresponding to the SSC is at $i = 270$. Windows used are: $l_w = 1000, o_w = 500$.

3.6.1.6 Anti-Aliasing

Suppose that there exist AE-pulses in the sampled waveform $x[n]$ that originate from multiple bearing defects. If the detector is set to capture a defect with failure rate, $f_{fault} = 1$, how could we know if the integrated pulses does not correspond to a bearing defect with a failure rate, $f_{fault} = 1k$, where $k \in \mathbb{N} > 1$? This can be recognised as an undersampling issue. Nyquist sampling theorem states that in order to not have aliases in a recorded signal, the sample rate must be equal to, or greater than the highest frequency component in the raw signal (Weik, 2001). At the pulse extraction stage (equation 17), $x[n]$ is essentially sampled in sections of width, l_w with a sample rate of f_{fault} per axle rotation. If there exists an AE defect in the bearing that excite pulses at for example $f_{fault} = 3$ these pulses would show up in K_i as three aliases. This scenario can be seen in Figure 23.
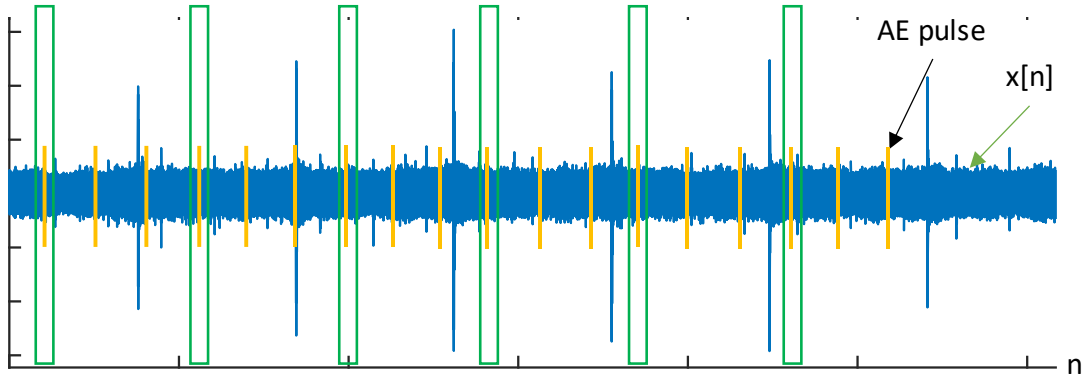
Figure 21, Alias problem. The green rectangles illustrate the sub-windows of window, $w_{j,s}^1[l_w, o_w, n]$. Notice that the spacing between the sub-windows indicate a sought defect repeating at $f_{fault} = 1$. However, the present AE pulses occur at a failure rate of $f_{fault} = 3$.

Given Nyquist's theorem and the scenario from Figure 21, we must extract pulses from $x[n]$ at a failure rate of $f_{fault} \geq 6$ to prevent aliases in the K-spectrum. This is illustrated in Figure 22.
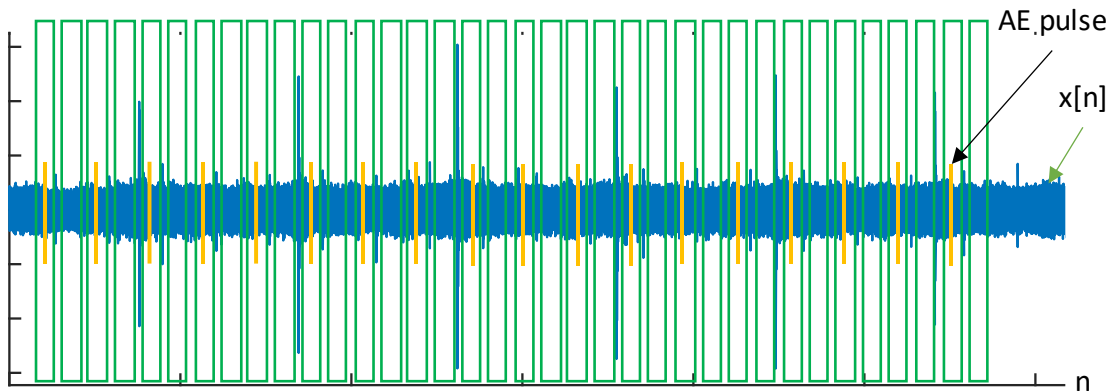
Figure 22, The detector extracts pulses at $f_{fault} = 6$.

However, by doing this, additional noise is introduced to the pulse extraction. This can be seen in Figure 22. Notice that every other sub-window (green rectangle) is located at a position where there is no AE pulse. This is *always* the case. Extracted pulses from these sub-windows using equation 17 will only add noise. What this means is that whenever there exists a bearing defect originated pulse in $x[n]$ that repeats at a multiple of the defect sought to detect, the aliases must be removed, rather than sampling at the Nyquist rate.

Figure 23, K-spectrum generated using $f_{fault} = 1$, $l_w = 1000$ and $o_w = 500$. Notice that the three protruding peaks are aliases of the AE pulses with $f_{fault} = 3$ shown in Figure 20. The spacing between the aliases is $max(i)/3$.

Additional information: As described in Figure 15, the file used to generate this K-spectrum contains a behaviour repeating at $f_{fault} = 1$. However, no significant peak from this behaviour is present in this K-spectrum. The reason for this is explained in section 5.1.3.

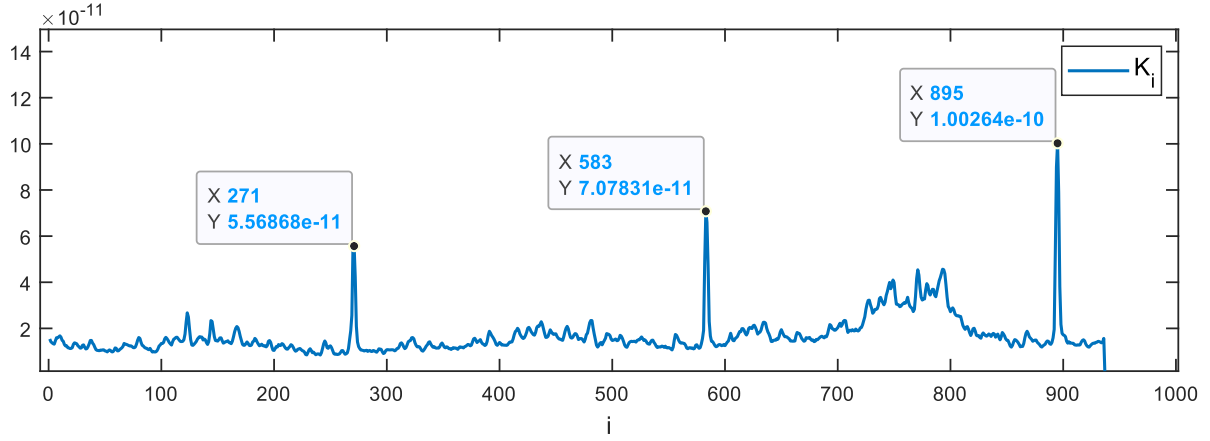The chosen way to remove aliases starts with finding the local maxima in the K-spectrum. This is done using the built in MATLAB function, *findpeaks* (MATLAB, 2021c). That is

$$[\boldsymbol{p}_{max}, \boldsymbol{p}_{loc}, \boldsymbol{p}_{width}, \sim] = findpeaks(K_i) \qquad 21$$

where $\boldsymbol{p}_{max}$ is the peak tops, $\boldsymbol{p}_{loc}$ is the *i*-locations, and $\boldsymbol{p}_{width}$ is the peak widths. Only peaks with prominence more than $0.01max(K_i)$ are included. The three $\boldsymbol{p}$-vectors are then sorted according to the $\boldsymbol{p}_{max}$ vector, as the alias peaks are assumed to be similar in height. Given the sorted location vector $\hat{\boldsymbol{p}}_{loc}$ the peaks that are considered aliases are set to the mean of K_i. Two peaks are considered aliases if the distance between them (in *i*-space) is equal to the length of the i-space, divided by $\frac{f_{alias}}{k}$, where f_{alias} is the failure rate of the alias, and $k = \{1,2,3, \dots f_{alias} - 1\}$. The expression becomes

$$K_m = \begin{cases} mean(K_i), & min\left(diff_{\hat{p}_{loc}}[n] - \dfrac{max(i)}{\left[\dfrac{f_{alias}}{1}, \dfrac{f_{alias}}{2}, \dots, \dfrac{f_{alias}}{f_{alias} - 1} \right]} \right) < q \\ K_m, & otherwise \end{cases} \qquad 22$$

Where $diff_{\hat{p}_{loc}}[h] = \hat{\boldsymbol{p}}_{loc}[h + 1] - \hat{\boldsymbol{p}}_{loc}[h]$,

41

$m = \{\hat{p}_{loc}[h] - \hat{p}_{width}[h], \ldots, \hat{p}_{loc}[h] + \hat{p}_{width}[h]\}$, $h = \{1,2,3, \ldots length(\boldsymbol{p}) - 1\}$, and q is a threshold that allows the peaks locations to be slightly shifted in i-space. It is typically set to $0.01max(i)$.
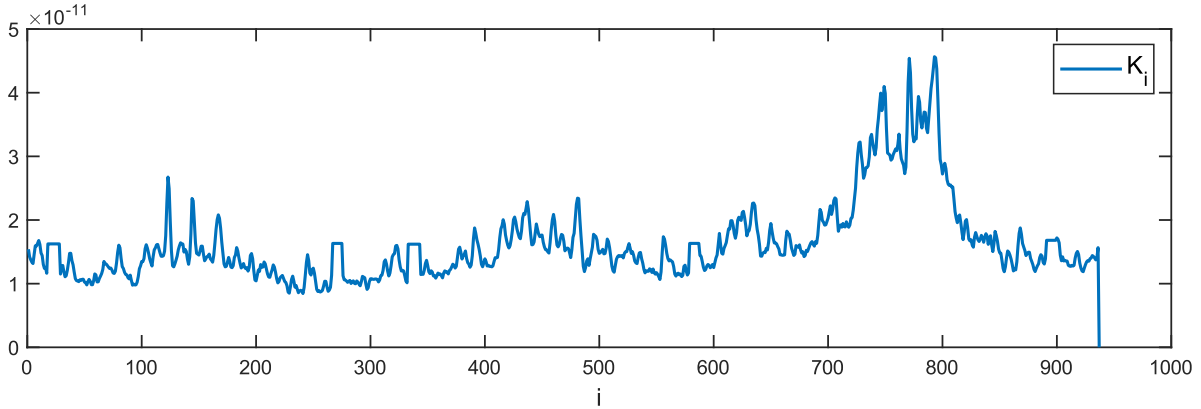
Figure 24, This is the same K-spectrum as in Figure 23, but now the aliases are removed.

3.6.1.7 *Peak extraction*

With the aliases removed, there is only one peak in K-spectrum that corresponds to the sought defect. This is the peak with the highest *peakPower*. The value, $peakPower = \frac{peakPromince}{peakWidth}$, captures two distinct parameters of a peak. The peak prominence, which must not be confused with *peak height* (or $\boldsymbol{p}_{max}$), denotes the distance from the root of the peak to the top. The reason why this parameter is used is simply because the peak with the largest peak height in the K-spectrum is *not* necessarily the peak corresponding to the sought defect. This scenario can be seen in Figure 25.

Figure 25, K-spectrum given $f_{fault} = 3$, $l_w = 1000$, $o_w = 500$. The most significant/prominent peak is located at $i = 77$, however the peak with the maximum value is located at $i = 245$. This K-spectrum corresponds to a sampled waveform from the KM-system, recorded 2021 Apr 30, 13:32:46.

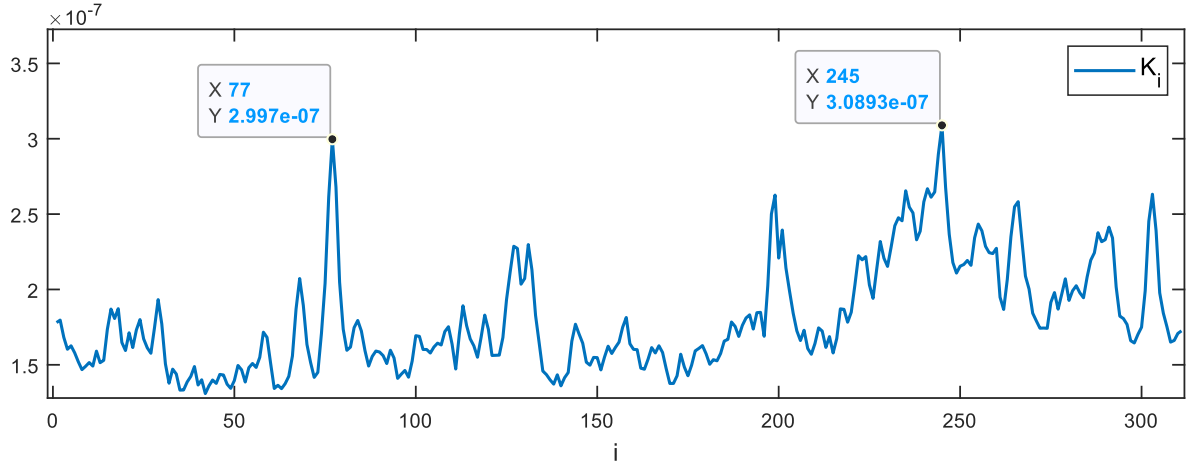The peak width is an indicator of how stably the AE pulses repeat. If the peak is narrow, only a few windows capture the AE pulses, which is a good indicator. Peak width also corresponds to how accurate the axle position is estimated. The equation describing *peakPower* is best described in MATLAB notation using logical indexing. That is

$$[\sim, \sim, \boldsymbol{p}_{width}, \boldsymbol{p}_{prom}] = findpeaks(K_i)$$

and,

$$peakPower = \frac{\boldsymbol{P}_{prom}\left[\frac{\boldsymbol{P}_{prom}}{\boldsymbol{P}_{width}} == max\left(\frac{\boldsymbol{P}_{prom}}{\boldsymbol{P}_{width}}\right)\right]}{\boldsymbol{P}_{width}\left[\frac{\boldsymbol{P}_{prom}}{\boldsymbol{P}_{width}} == max\left(\frac{\boldsymbol{P}_{prom}}{\boldsymbol{P}_{width}}\right)\right]} \tag{23}$$

Edge case: The peak with the highest peakPower *can* be located between the first and last entries in i-space (or the first and last windows). This is solved by performing the peak extraction step (equation 23) twice. The first is performed with the original K-spectrum directly. The second is performed with the K-spectrum shifted circularly with a shift length of $max(i)/4$. The extracted peak with the highest peakPower from either the K-spectrum or the circularly shifted K-spectrum is chosen. An example of this edge case can be seen in Figure 53.

3.6.1.8 Noise

Friction-and electrically generated noise can alter the AE waveform drastically. Figure 26, displays the spectrograms from friction originated AE waveforms at different load levels.
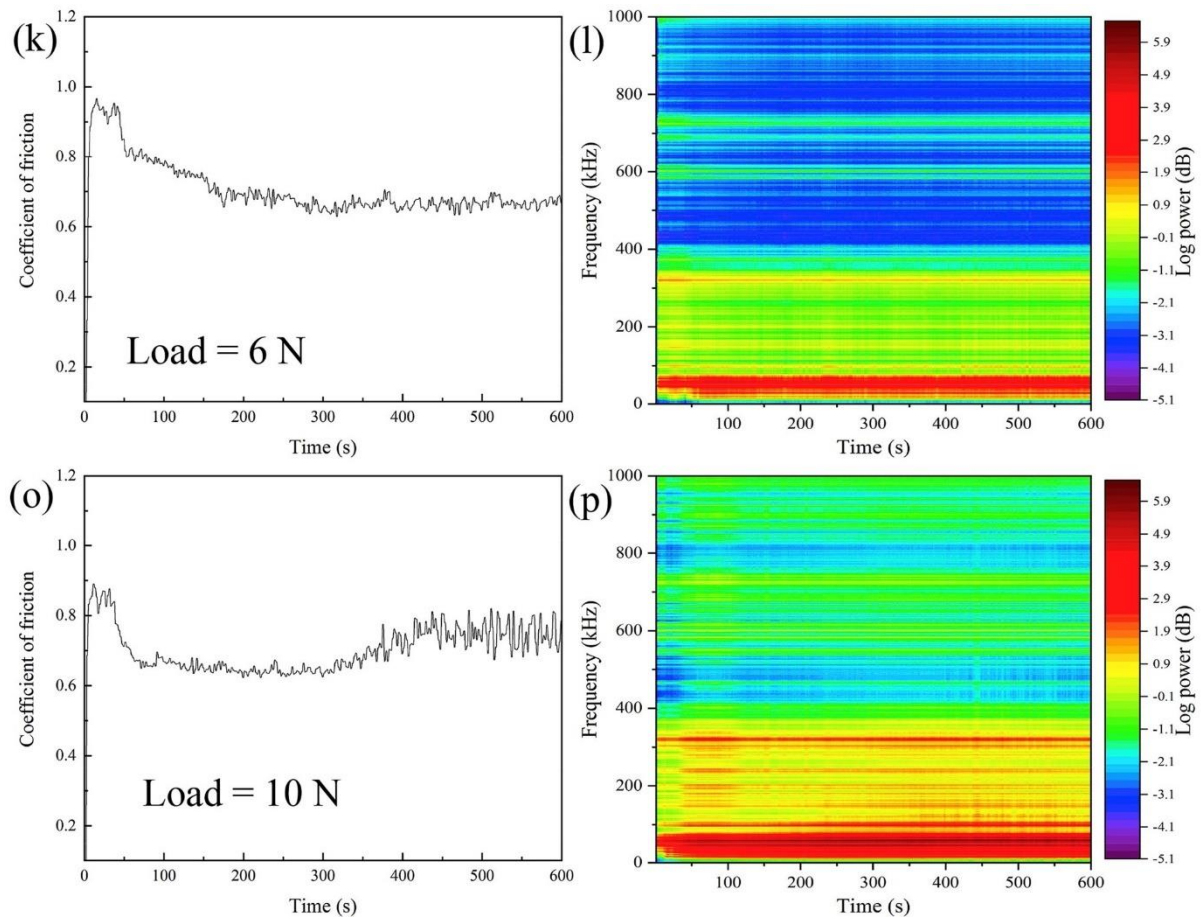
Figure 26, The observations from a friction and wear characterizing study, done by (Geng, Puhan, & Reddyhoff, 2019). Notice the dramatic increase in AE activity from $400kHz$ to $1MHz$ when the applied load is increased.

When an RM excite AE waveforms containing these levels of noise, the SNR is simply too small to detect any sub-surface cracks. However, the K-spectrums generated from these waveforms can potentially contain significant peaks, as seen in Figure 27.
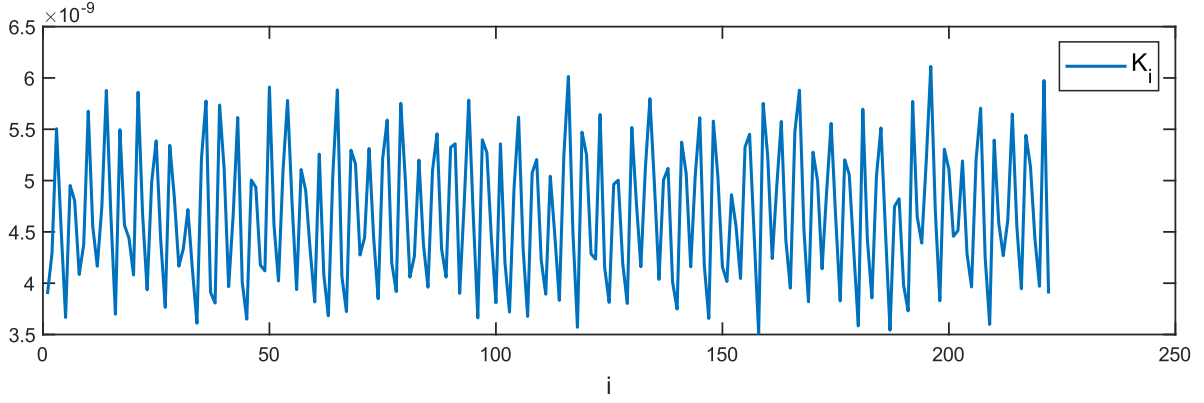
Figure 27, K-spectrum given $f_{fault} = 3$, $l_w = 1000$, $o_w = 500$. This is generated from a sampled AE waveform recorded 2021 Apr 7, 15:31:33 on MISTRAS, with high noise content. Compared to the K-spectrum in Figure 20, the lowest value here is more than 16 times larger than the peak in Figure 20.

These peaks must not be mistaken for crack related peaks, as this would increase p_{fa} (probability of false alarm). However, another consequence of high noise AE waveforms is that the corresponding K-spectrums are higher valued. That is

$$\int_i K_t^{SNR>k} \, dt < \int_i K_t^{SNR<k} \, dt, \text{ for some real number } k. \qquad\qquad 24$$

Thus, the integral of $\boldsymbol{K}_i$ is inversely proportional to the confidence of the peakPower.

3.6.1.9 K-spectrum length

The window length, l_w, and window overlap, o_w, are always kept constant. Given equations 13-20, the number of windows, which is equal to the length of the K-spectrum, are determined by the rotation frequency, f_r, l_w, and o_w. If f_r is reduced, the K-spectrum length is increased, and vice versa. Since the integral of K_i is proportional to the length of the K-spectrum (length of the i-space), this must also be compensated for when normalizing peakPower.

3.6.1.10 Normalizing

Given the statements in section 3.6.1.8 and 3.6.1.9, the final likelihood ratio for crack related AE pulses at a particular failure rate is the normalized peakPower. That is

$$L = \frac{peakPower}{max(i) \int_i K_t \, dt} \qquad 25$$

3.6.1.11 Threshold *T*

A simple model for the threshold, T, given by the NP-criteria, is used as basis for decision making. It is inspired by the built in function in MATLAB *isoutlier* (MATLAB, 2021e), and establishes an upper threshold for L, given the baseline of historic L-s, discussed in section 2.4.4. The chosen definition for T is

$$T = 3mad(Baseline) + median(Baseline) \qquad 26$$

where $Baseline = [L_0, L_1, \ldots, L_{l_b}]$, and l_b is the chosen length of the baseline. The definitions for functions *mad* and *median* are given in equation 19.

3.6.1.12 The final detector

Although measures have been taken to prevent noise and unrelated AE activity to interfere with the detector decision making, abnormal AE activity will still cause detections, $L \geq T$, unrelated to the sought bearing defect. The chosen solution to this problem is to use a *confidence* parameter, c. Abnormal AE behaviour are typically bursts/pulses of unknown character that does not repeat consistently. Detections, $L \geq T$, originated from these behaviours will therefore not represent a change in *trend*. Given the *confidence* parameter, c, the only detection, $L \geq T$ that will cause the detector to decide D_1, is the detection $L \geq T$ preceding c previous consecutive detections. That is, c consecutive detections are needed for the detector to decide D_1, *defect detected.* Thus, the final expression for the detector is,

$$D(L, T, c) = \begin{cases} D_1 & [L_{-c}, L_{-c+1}, L_{-c+2}, \ldots, L] \geq T \\ D_0 & otherwise \end{cases} \qquad 27$$

A flowchart of the detector, Figure 28, is displayed on the next page. As discussed in 2.4.4, a bearing defect does not disappear over time. Consequently, once the detector reaches the decision $D = D_1$, this decision stays until the system is restarted. An alternative would be to include a *discard defect* option that is operated manually by a machine operator. This is not included in this work, as the goal is to determine a bearing defect early.
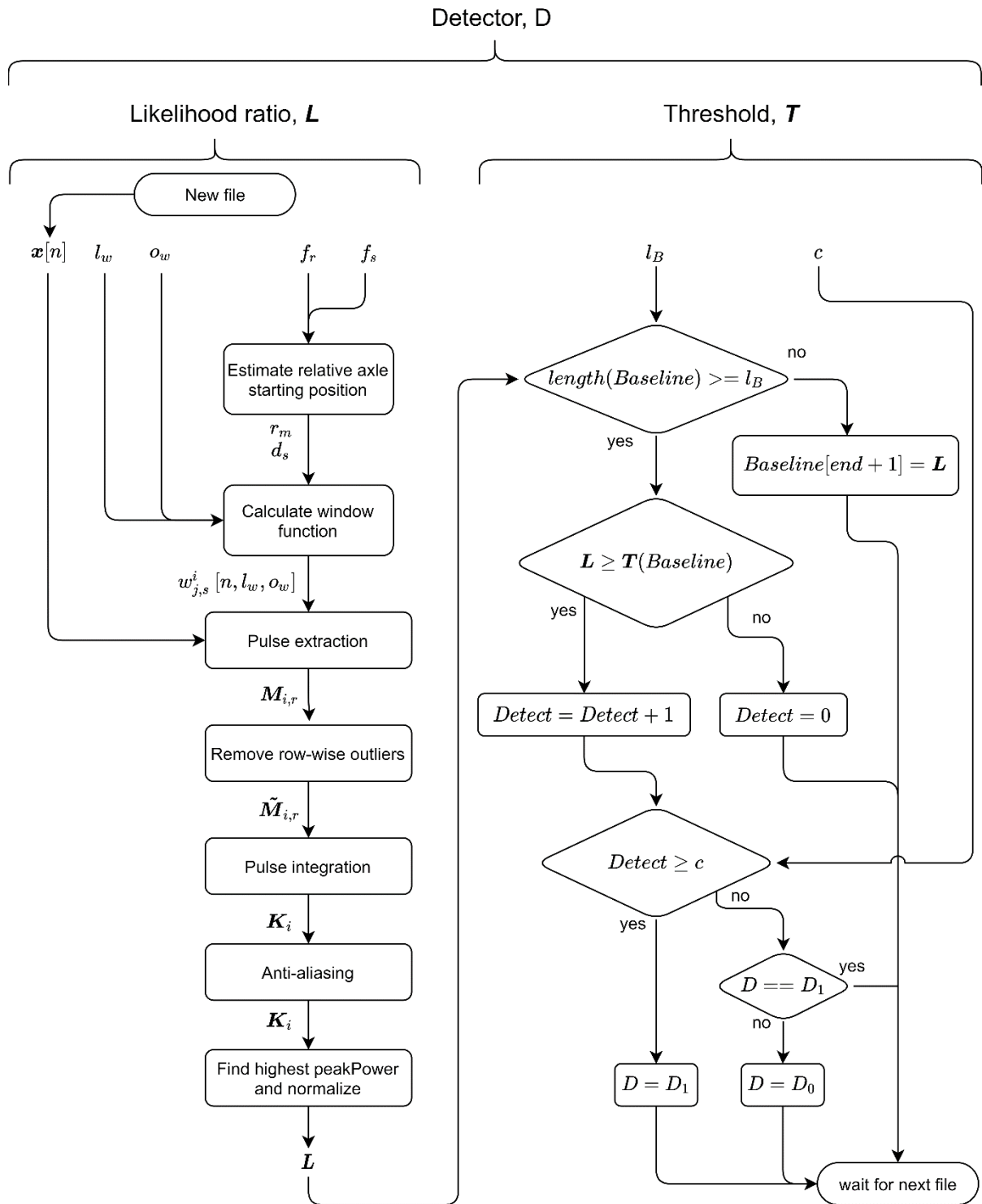
Figure 28, Flowchart for the proposed detector.

3.6.2   Pulse Integrated Spectrogram

As described in section 2.5.3, (Price et al., 2005) suggested than an automatic pattern recognition system could be based on the time-frequency representation of the AE waveform for identifying the presence of SSCs. In this work, the identification is done by the proposed detector. However, how can we verify that the detector detects the sought defects? The chosen solution was to develop a visual verification tool based on the time-frequency representation of the AE waveform, as suggested by (Price et al., 2005).

The tool is based on the *spectrogram,* which is one way to visualize the waveform in time-frequency domain. The built in MATLAB function *pspectrum* (MATLAB, 2021f) was the chosen function used to generate it. Now, recall that the proposed detector only reacts to AE pulses repeating at a fixed rate, that is f_{fault}. Without the pulse integration step, these pulses can be so weak that they do not register in a spectrogram. The solution is to pulse integrate the high-pass filtered waveform $x_{HP}[n]$ before generating the spectrogram. To verify that the pulses indeed occur at f_{fault} from r_s to r_{s+1} each

$x_{HP}[r_s, r_s + 1, \dots, r_s + d_s]$ is envelope detected. The envelope detector used is the same as described in 3.6.1.7. Then, the envelope detected rotations segments are pulse integrated. The output is a signal vector $y[n]$, where AE pulses repeating consistently between every r_s, is amplified. As this is based on the general solution, where the distance between axle start-positions can vary, the expression is simplified by using the average rotation distance $mean(d_s)$.

$$y[n] = \sum_{s=1}^{m-1}\left(a_{gain}x_{HP}[r_s, r_s + 1, \dots, r_s + d]\right)^2,$$

$PIS = pspectrum\{y[n]\}$, where $d = mean(d_s)$, and a_{gain} is a gain constant that is tuned manually for best contrast in the PIS.

(28)

The chosen peak in the K-spectrum corresponding a specific detection can now be visually verified from the pulse integrated spectrogram (PIS). An example is shown in Figure 29.
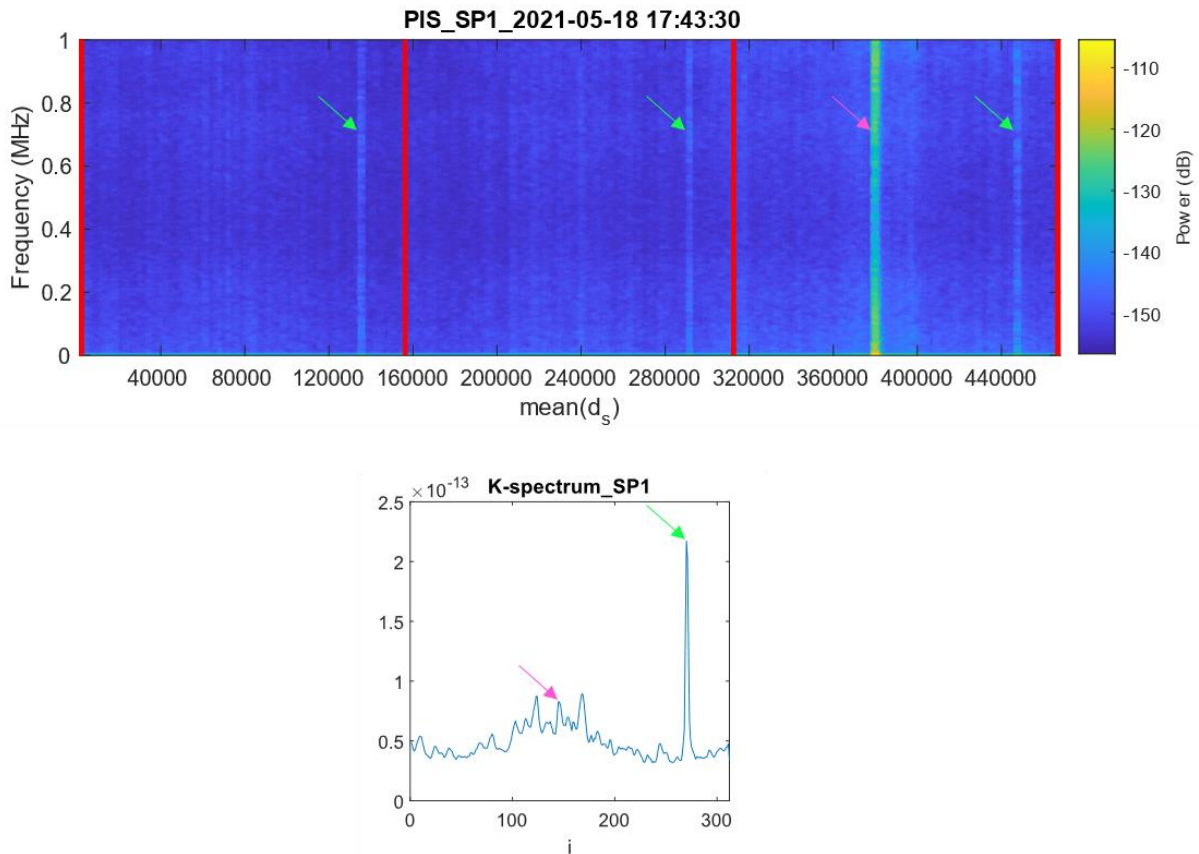
Figure 29, **Top**: PIS. **Bottom:** corresponding K-spectrum for the file specified in section 3.6.1.1. The detector for this K-spectrum, seeks a defect with $f_{fault} = 3$.

The confirmation that is made from the PIS verification displayed in Figure 29, is performed this way:

There are four red vertical lines in this PIS. The three segments limited by the red lines should all contain one AE pulse that corresponds to a single peak in the K-spectrum. That is, an AE pulse should occur at the same position in all three segments. The peak with the highest peakPower should be in the same relative position in the K-spectrum. Thus, the three AE pulses marked with green arrows in the PIS corresponds to the peak in K-spectrum marked with a green arrow. We now *know* if the detector reacted to the correct AE behaviour. Additionally, notice that the much stronger AE pulse marked with a pink arrow does not generate any substantial peaks in the K-spectrum. As this pulse only appears in once in the PIS, that means that it corresponds to an $f_{fault} = 1$. Due to the outlier removal step expressed in section 3.6.1.5, this behaviour does not interfere when we try to detect defects with $f_{fault} = 3$. The "Power (dB)" scale in Figure 29 is influenced by the gain parameter

a_{gain} in equation 28, and thus not provide any useful information to the PIS. In the PIS verifications in section 4.2, this scale is therefore hidden to not cause any confusion.

3.6.3   Estimating f_r

In 3.6.1.2, f_r was assumed to be known. Referencing the test log to the timing marks in the filename of each AE-recording, the correct f_r can then be mapped to each file. However, for pulse integration to work optimally, the accuracy of f_r must be precise. The solution chosen, was to run the detector on a specific AE-recording, with a known defect present in the waveform. The file chosen from the MISTRAS system was recorded 2021 May 18, 17:43:30, and contained the AE pulses originated from a subsurface defect, repeating at $f_{fault} = 3$. At this time, the approximate f_r given in the test log was $f_r = \frac{F_A=256rpm}{60} = 4.267Hz$. Monitoring which i-positions in the K-spectrum the defect was present, the detector was run repeatedly on the same file, incrementing the f_r from one run to the next. The best estimate for f_r was achieved when the i-position in K-spectrum reached the maximum value. This process was repeated until the maximum value in the K-spectrum stabilized, at which the f_r increment was in range of nHz. Window parameters were kept constant at $l_w = 1000$ and $o_w = 500$ for the whole process. After the optimum f_r was determined, the detector was tried on other files recorded at the same F_A to verify rpm consistency. The result concluded that the rpm was stable enough that the optimum f_r could be used for all files recorded at $F_A = 256rpm$. The same process was done to estimate f_r for files recorded at $F_A = 364RPM$.

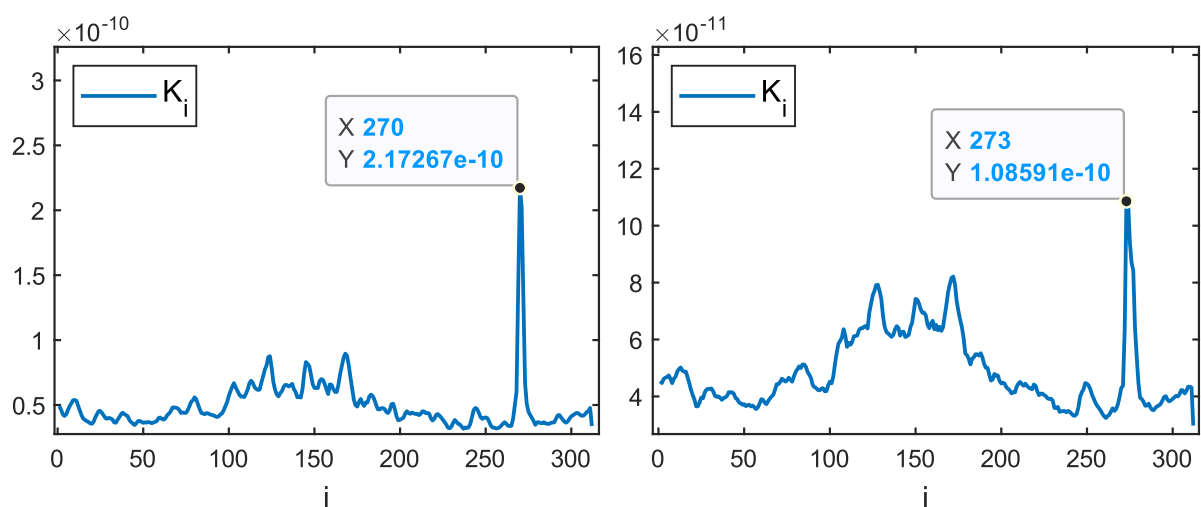Figure 30, f_r accuracy. **Left**: The K-spectrum calculated with the best estimate of $f_r = 4.2660Hz$. The sampled AE waveform is from the file stated in section 3.6.2. **Right**: The same K_spectrum, but here $f_r = 4.2670Hz$, which illustrates the importance of accurate rotation frequency. Notice that the peak height corresponding to the bearing defect is half the value of the peak in the left K-spectrum.

The same procedure was done for the KM-system. However, the optimum f_r for the KM system was slightly lower than the optimum f_r for the MISRAS system. The difference is believed to be caused by a slight difference in f_s between the two systems.

Ultimately, the optimum estimated frequencies are

$$f_r^{KM,256} = 4.266013 \ Hz,$$
$$f_r^{KM,364} = 6.055189 \ Hz,$$
$$f_r^{MISTRAS,256} = 4.266019 \ Hz,$$
$$f_r^{MISTRAS,364} = 6.0552034 \ Hz.$$

29

3.6.4 System architecture and data handling

Working on $652 GB$ of raw data requires a data processing architecture that is robust and built with efficiency and traceability as main quality requirements. Another challenge to be solved was the fact that the system was built during the duration test, which means that it also had to be modular. MATLAB was the chosen system developing environment for this work. Time is an important dimension in this work. Information about f_r and contact stress at a particular time can only be found in the test-log. The files recorded on the Mistras system only provided the time of recording in the filename. The MATLAB built-in *datetime* (MATLAB, 2021a) array function was therefore used extensively to ensure time consistency.

The following list describes the workflow.

- Data location
  Three SSD-s where used in this work, that is the C-drive (500GB), SSD-A(1TB) and SSD-B (500GB). All code was stored on the C-drive, MISTRAS-data was stored in SSD-A, and KM-data was stored in SSD-B.

- Generate K-spectrums
  During system development, the first important step is to reduce raw data to data features that occupy little space on the SSD. This is the most time-consuming step and should be done as few times as possible during system development. This implies that

only the necessary steps required to generate the data features are done. System implementations such as normalizing, and anti-aliasing are *not* developed here.

In this case, the first processing stage is to generate K-spectrums from the raw files. This is done for one system at the time. For each file, a datetime-object is created from the filename. This is cross-referenced with datetime-objects gathered from the test-log, to establish the contact stress and f_r at the time of the recording. Correct sensor position, SPx is also collected from the filename. One K-spectrum is then calculated for each of the defect behaviours sought to detect (ref 4.2). When finished, all K-spectrums, f_r , defect-description, SPx, datetime-object, and RMS (ref 5.2.3) of the entire recording and are combined in a cell-array and stored in one .mat-file. The .mat-file filename is equal to the input-file filename.

This process takes approximately five hours to complete for the SP1 (MISTRAS) data, and approximately 2 hours for SP2 (KM) data, using an Intel i9-9900K CPU. It is therefore typically performed overnight. When finished, all the .mat-files from the MISTRAS system require approximately $90MB$ combined, and the -mat-files from the KM-system require approximately $20MB$ combined. The most important advantage in storing one .mat-file per raw data-file, is that when new files are gathered from the ongoing duration test, the old files do not need to be recalculated.

- Calculate *L*

   The next step is to calculate *L*. Given the K-spectrums saved in the .mat-files, anti-aliasing, peak extraction and normalizing are performed. Finally, the calculated L-s, f_r, and defect-description are stored in a result-table. One result-table per system is stored as a .csv-file. The whole process takes approximately one minute for the MISTRAS system.

- Plotting

   Given the result-table: Baseline, and T are calculated. Then all *L*-s are plotted with respect to defect behaviour (f_{fault}), and system. Positive detector decisions D_1 (defect detected), are visualized in the *L*-plots as x-markers.

4 Results

4.1 Test log and PAUT results

Multiple SSCs were developed in the test specimen during the duration test. Only one of them were identified in PAUT. The rest were identified in post inspection done by SINTEF. This was performed using a salami cutting procedure. The first SSC identified in PAUT was first discovered after 29,095,504 fatigue cycles, that is (16,466,958 + 10,891,798 + 1,736,748) fatigue cycles at (1800 MPa, 1900 MPa and 2000 MPa) contact stress respectively. The width of the SSC was at this point 0.5 mm. At 66,585,266 fatigue cycles, the duration test was terminated. The SSC had now grown to a 2 mm width and 10 mm length, extending in the transverse direction. No surface spalling, pitting or roughness was identified on the test specimen contact surface in neither PAUTs nor salami-inspection.

A compressed version of the test-log is presented in Table 2. Results from PAUT and post inspection is presented in Figure 31, Figure 32 and Figure 33.

| Date	Contact stress	F_A	SSC-width [mm]	Fatigue cycle count	Description
16-03-21	1800 MPa	364 RPM	0	0	Test started.
12-04-21	1900 MPa	364 RPM	0	16,466,958	Increased contact stress.
19-04-21	2000 MPa	364 RPM	0	27,358,756	Increased contact stress.
19-04-21	2000 MPa		0	27,831,079	Machine stopped due to vibration alarm. The loading (contact stress) is active overnight.
20-04-21	2000 MPa	256 RPM	0	27,831,079	F_A is reduced and the machine is functioning correctly.
21-04-21	2000 MPa	256 RPM	0.5	29,095,504	One SSC discovered, extending in the transverse direction (TD).
27-04-21	2000 MPa	256 RPM	0.5	35,920,018	Machine stopped due to vibration alarm.
29-04-21	2000 MPA	256 RPM	1.0	37,086,115	Crack growth. Direction TD.
11-05-21	2000 MPa	256 RPM	1.5	50,248,116	Crack growth. Direction TD.
13-05-21	2000 MPa	256 RPM	1.5	52,708,597	1.5 mm wide crack. Direction TD. 5-10 mm long.
18-05-21	2000 MPa	256 RPM	1.5	52,708,597	Starting continuous testing without PAUT.
27-05-21	1900 MPa	256 RPM	(No PAUT)	62,578,177	Reduced contact stress.
27-05-21	1900 MPa	256 RPM	(No PAUT)	62,753,322	Machine stopped due to power loss.
01-06-21	1900 MPa	364 RPM	(No PAUT)	63,759,638	Increased F_A.
02-06-21	2000 MPa	256 RPM	(No PAUT)	65,370,773	Increased contact stress, reduced F_A.
03-06-21	2000 MPa	256 RPM	2	66,585,266	Test finished. 10 mm long crack. Direction TD. 2 mm wide.

Table 2, Compressed test-log.
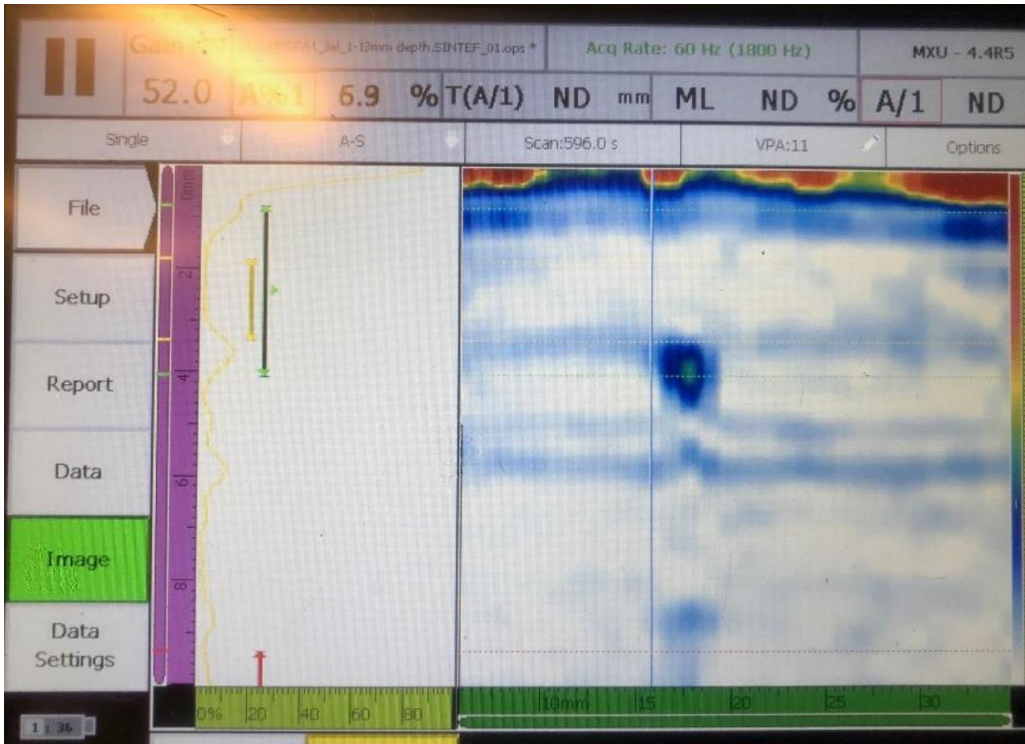
Figure 31, The first PAUT identifying the presence of an SSC. This photo is provided by Hans Lange from SINTEF.

Figure 32, The final PAUT after the test was terminated. This photo is provided by Hans Lange from SINTEF.
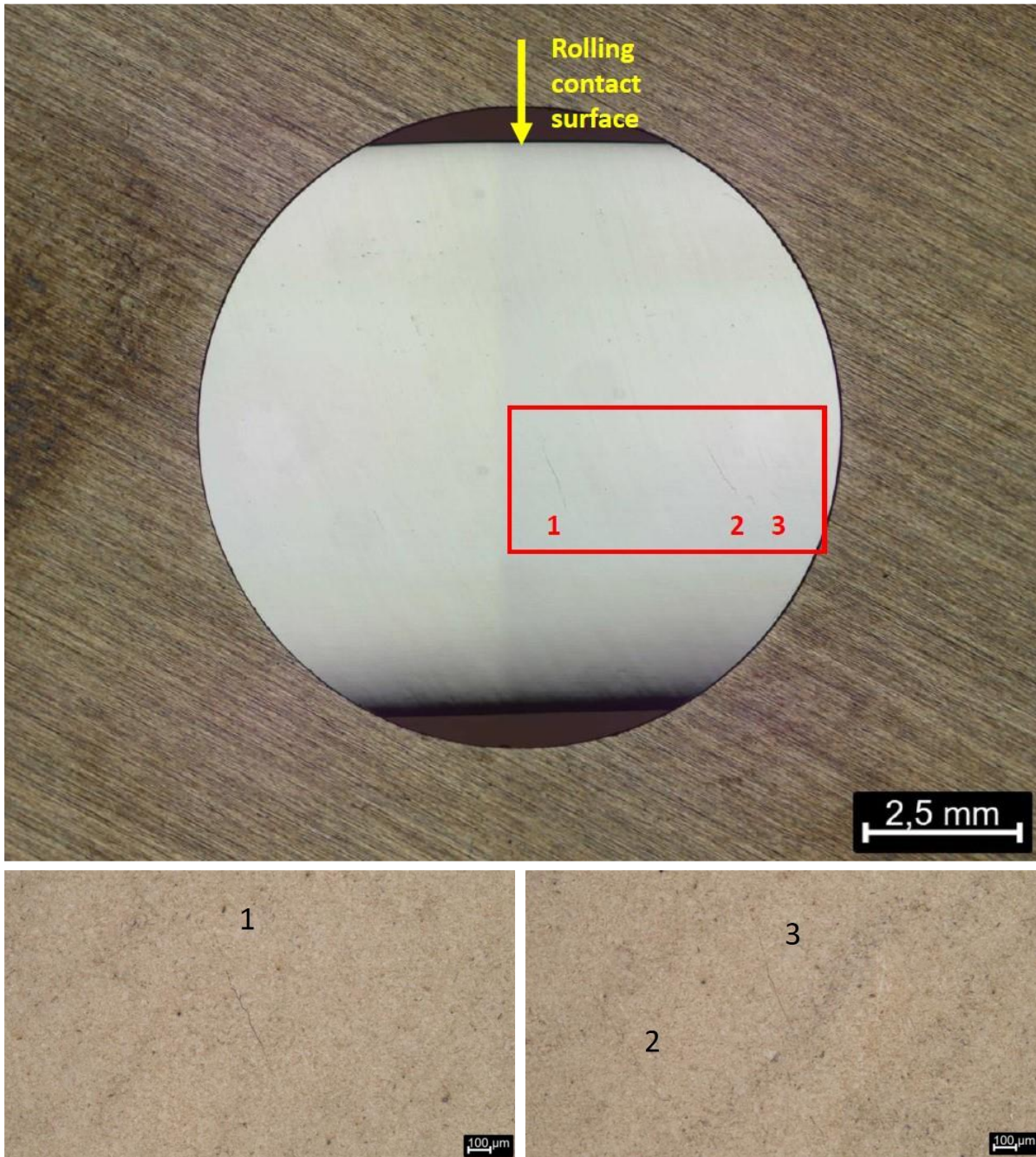
Figure 33, Results from post inspection (salami).

4.2 Observed defect behaviours

Given name	f_{fault}
rollerPass	$3/rev$
rotationPass	$1/rev$
BPFO	$13.0209/rev$
100 Hz	$100\ Hz$

Table 3, Observed repeating AE behaviours from the duration test.

A total of 4 different consistently repeating AE behaviours were observed during the duration test. An overview of the behaviours is presented in Table 3. 4 detector-instanced were used to track each behaviour for all SPx. All available files are used as input, including the files used for baselining (to determine T). Each behaviour will be explained in detail in the following sections. L-time plots are presented for each sensor. Detector decisions D_1 (*defect detected*), will be presented for SP1 and SP2 only. This is because the number of files available from SP3-SP5 are not sufficient to establish a proper baseline. The purpose of presenting the L-time plots for these sensors is to provide a more complete overview of how the overserved behaviours were observed from different locations.

Parameters for the detector is given in Table 4. These parameters apply to all plots in the following section.

Detector parameters	
l_w	1000
o_w	500
c	10
l_B	All recordings from test start to 2021 Apr 17, 00:00:00. That is, SP1(MISTRAS): $l_B = 2064$, and SP2(KM): $l_B = 300$

Table 4, Chosen detector parameters.

4.2.1   Behaviour 1, rollerPass

4.2.1.1   SP1 and SP2

The observed behaviour corresponding to $f_{fault} = 3/rev$, is denoted *rollerPass*. That is – the *only* place in the test machine that will cause this behaviour, is a point on the test specimen perimeter passing the support rollers. L-time plots and detector decisions D_1 for SP1 and SP2 are presented in Figure 34. PIS verification of detector decision D_1 for both sensors are displayed in Figure 35.
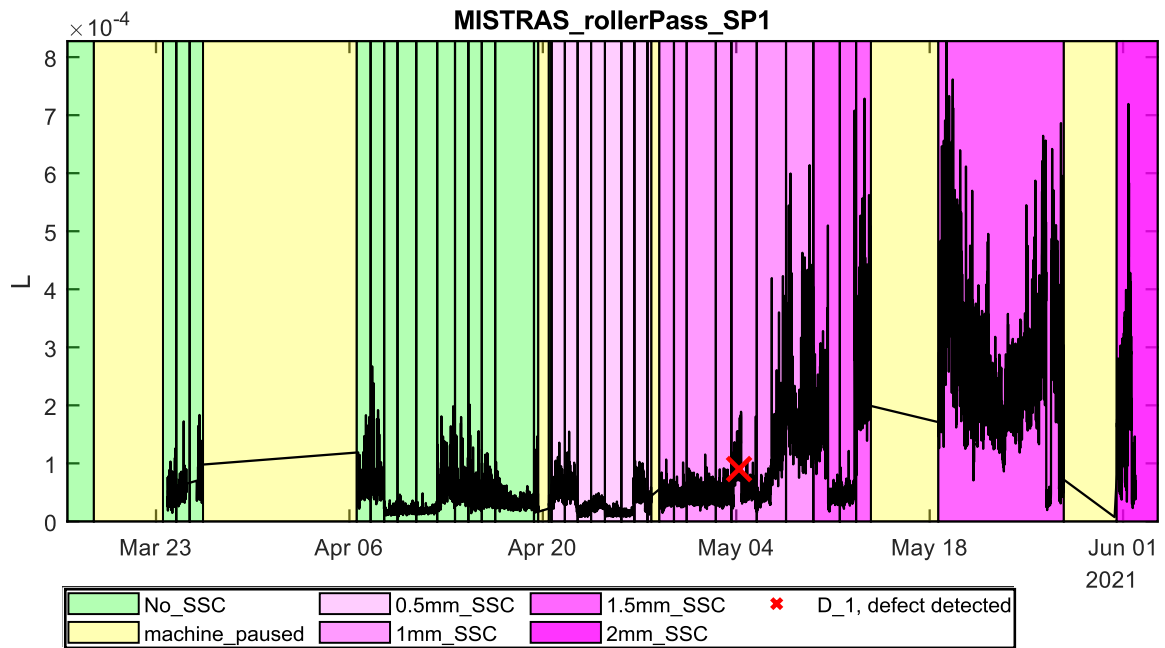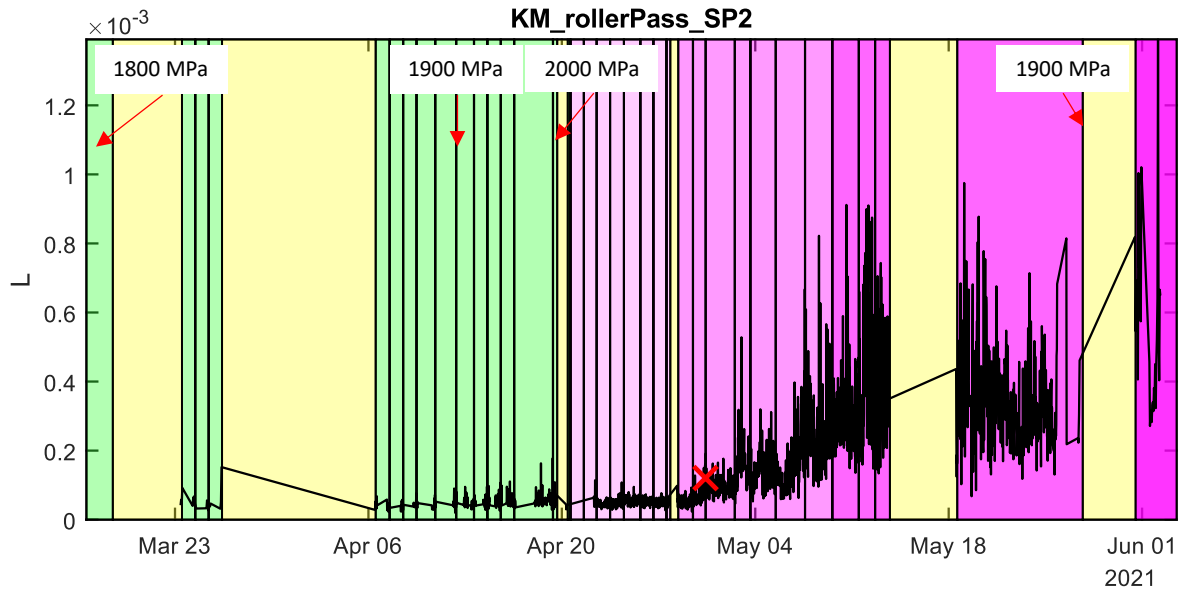
Figure 34, L-time plots for SP1 and SP2, rollerPass. Colour coding refers to SSC presence – and magnitude. The black vertical lines indicate PAUTs. Change in contact stress throughout the test is indicated in the white rectangles. D_1, for both sensors happen at a $SSC_{width} = 1mm$.
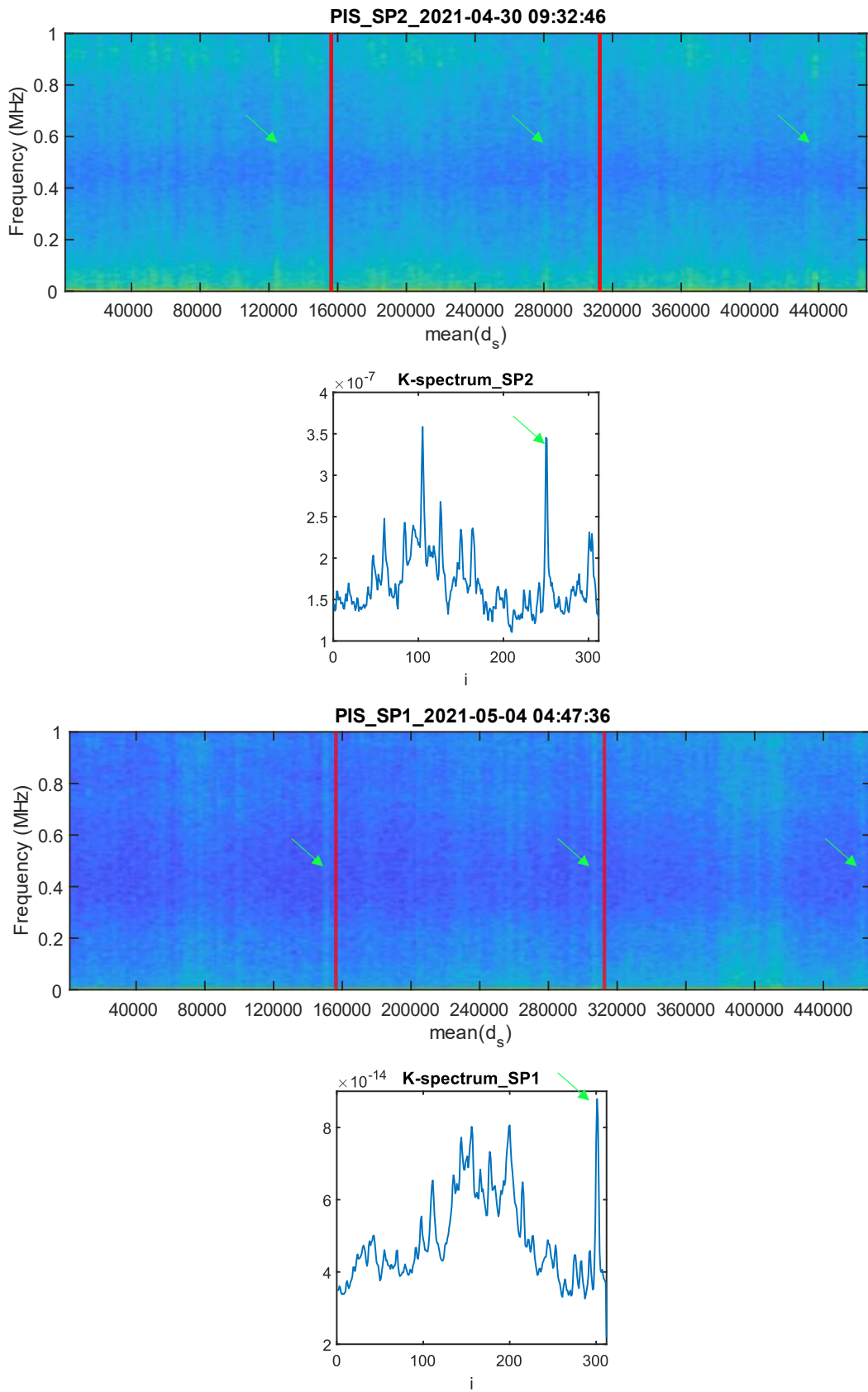
Figure 35, PIS verification, SP1 and SP2, rollerPass.

For the rollerPass behaviour, the AE pulse propagation to SP3-SP5 is considered equal. The PIS verification is therefore chosen according to the first significant peak in the L-time plot. Shown in Figure 36, the earliest significant peak corresponds to the file recorded 2021 May 23, 20:24:38, from SP3. The PIS confirmation is displayed in Figure 37.
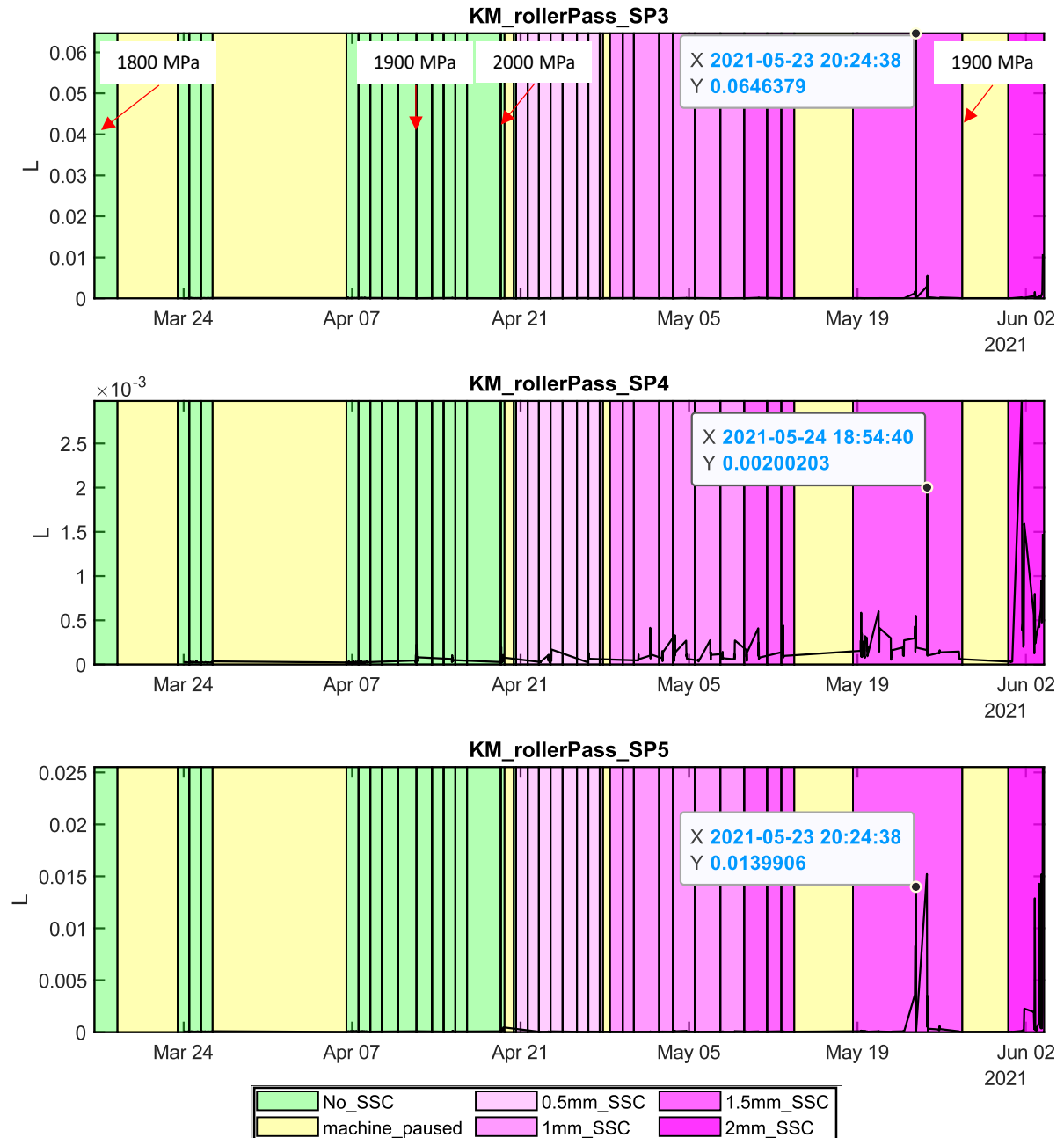

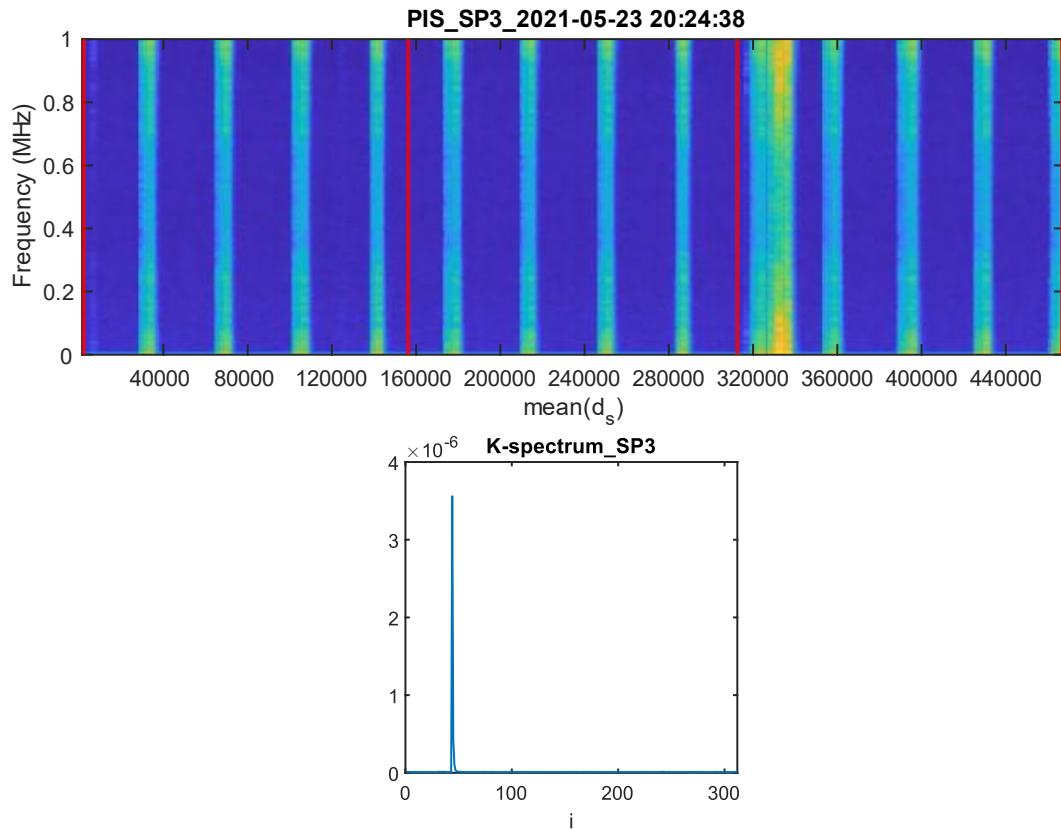Figure 36, L vs time plots for SP3-SP5, rollerPass.

Figure 37, PIS verification, SP3, rollerPass. No confirmation can be made. No distinct behaviour appears once between the red lines. The strong visible behaviour can originate from something else.

4.2.2 Behaviour 2, rotationPass

4.2.2.1 SP1 and SP2

The observed behaviour corresponding to $f_{fault} = 1/rev$, is denoted *rotationPass,* as it repeats once every axle rotation. There are three places in the test machine where this behaviour can originate from:

1- A point on the perimeter of a support roller, passing the test specimen.
2- A defect on either the inner or outer raceway of the linear bearing (Appendix E)
3- A defect on the axle or the axle coupling.

The behaviour does not repeat stably. In order to detect it, the outlier removal step (explained in section 3.6.1.5) had to be turned off. As this is the only behaviour that could potentially be influenced by aliasing (from the rollerPass behaviour), anti-aliasing is only performed on this behaviour. More will be discussed in section 5.1.3.

L-time plots and corresponding detector decision, D_1 for SP1 and SP2 are presented in Figure 38. PIS verification of detector decisions D_1 for both sensors are displayed in Figure 39.
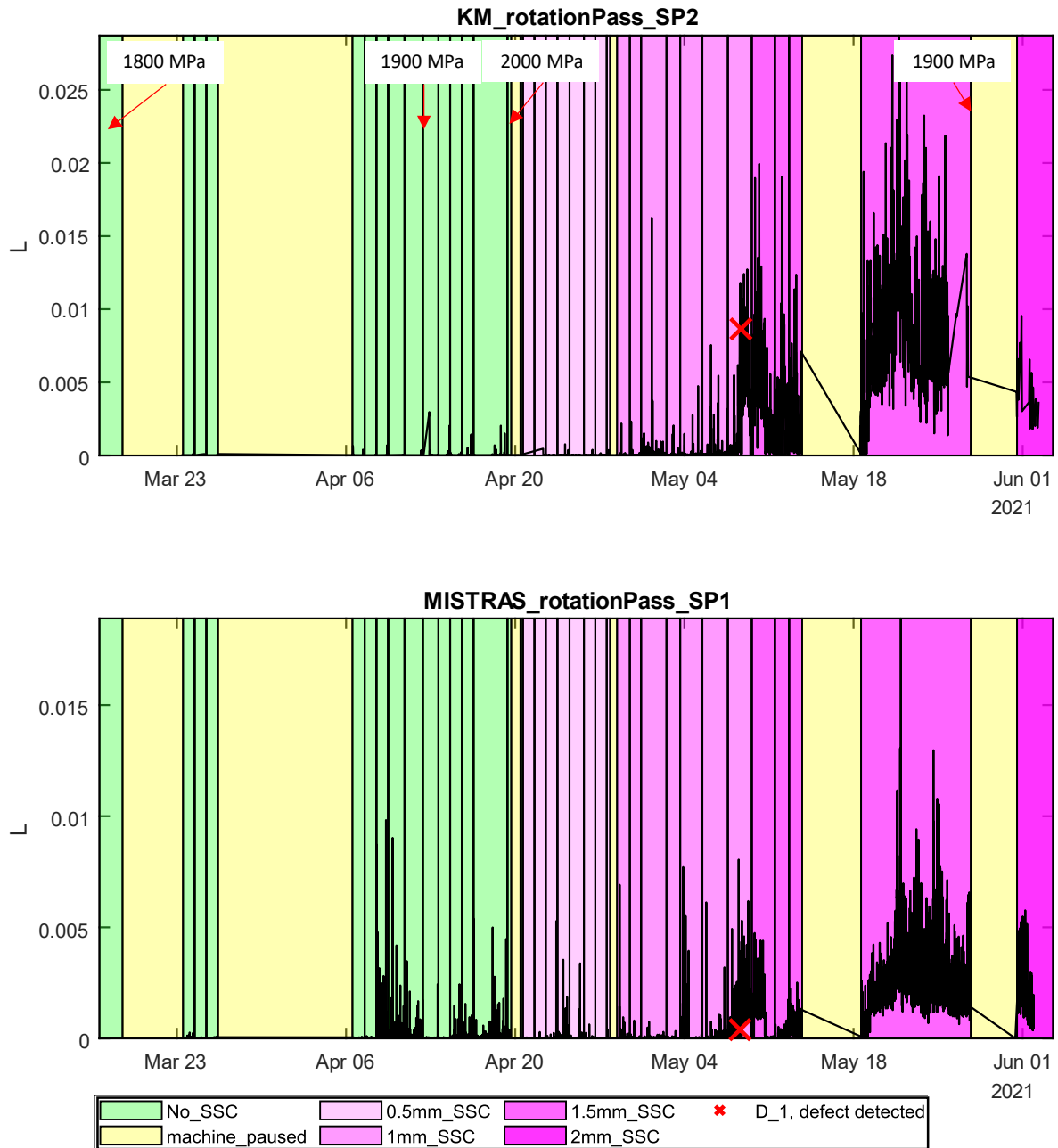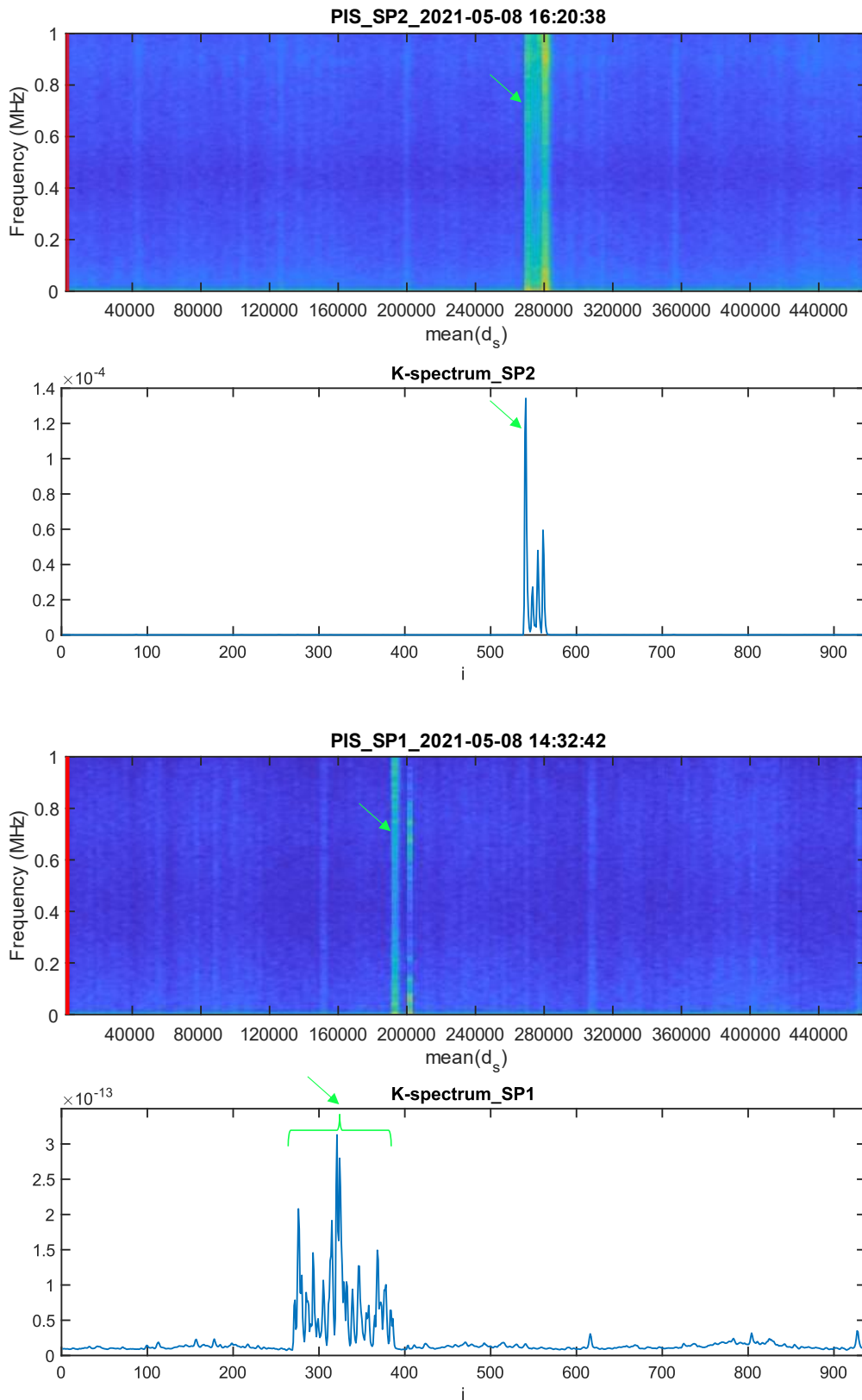

Figure 38, L-time plots for SP1 and SP2, rotationPass.

Figure 39, PIS verification, SP1 and SP2, rotationPass. These plots indicate that the rollerPass behaviour does not repeat stably. In the K-spectrum_SP1-plot, the peak "forest" from window position 270 to 390 indicate that the behaviour was observed in all these windows. This is explained more thoroughly in discussion section 5.1.3.

4.2.2.2 SP3 – SP5

As explained in section 4.2.1.1, this behaviour can originate from three places in the test machine. If the behaviour originates from a support roller, the pulse propagation to SP3-SP5 would not be equal. The PIS verification is therefore done according to the first significant peak in the L-time for each sensor. Shown in Figure 40, the chosen files are marked with black arrows. The PIS confirmations is displayed in Figure 41, Figure 42 and Figure 43.
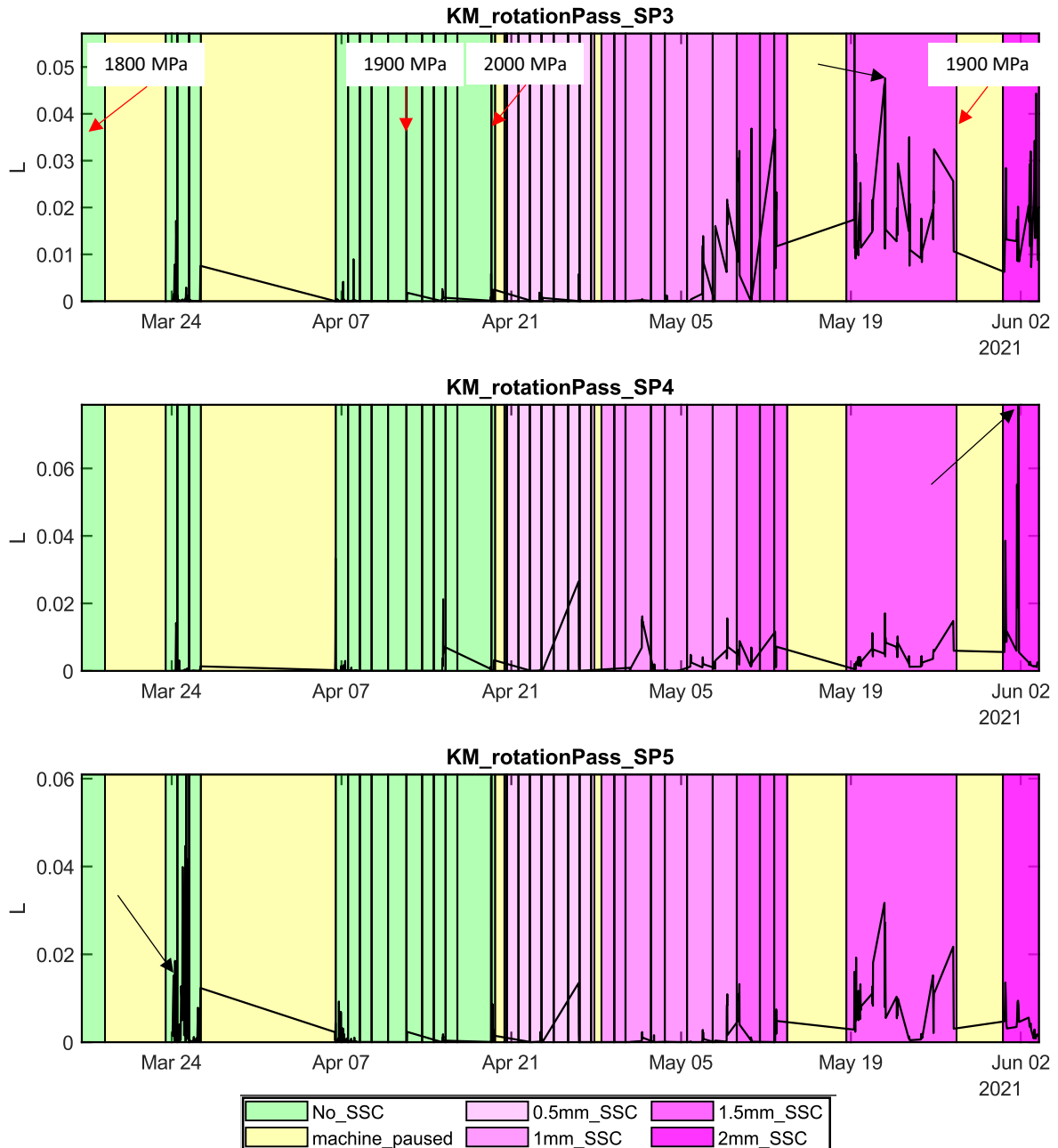
Figure 40, L vs datetime plots for SP3-SP5, rotationPass.
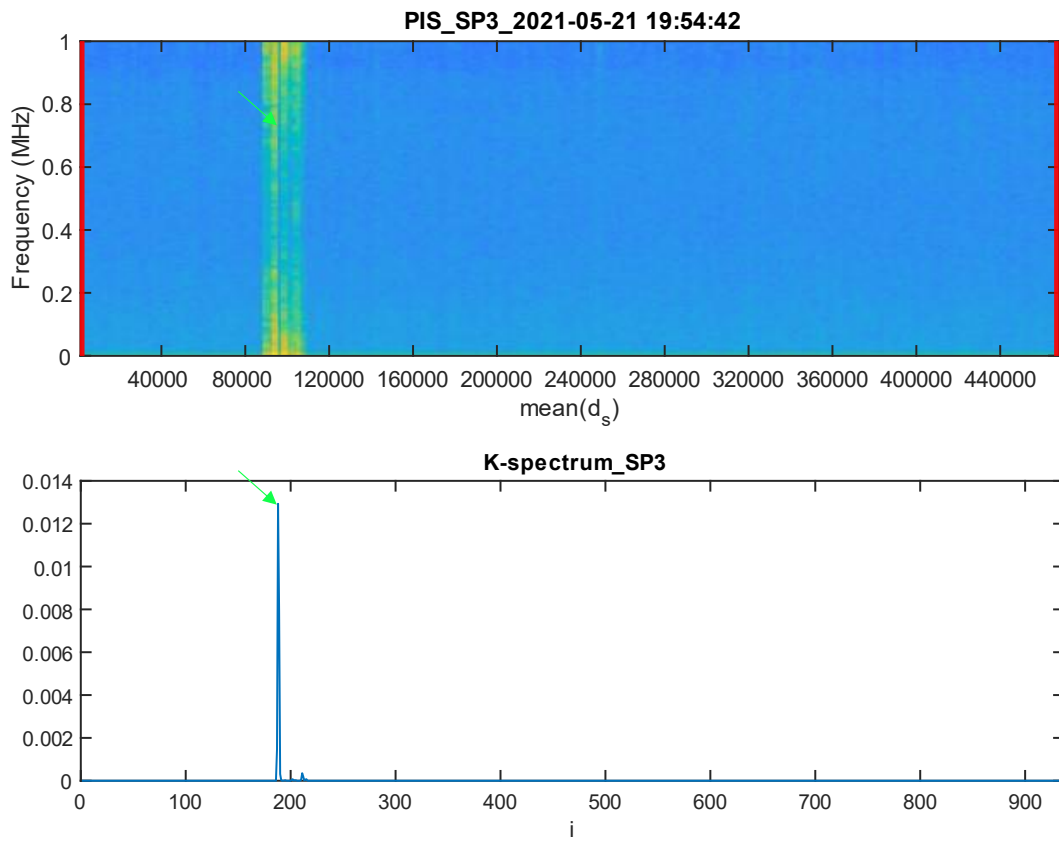
65
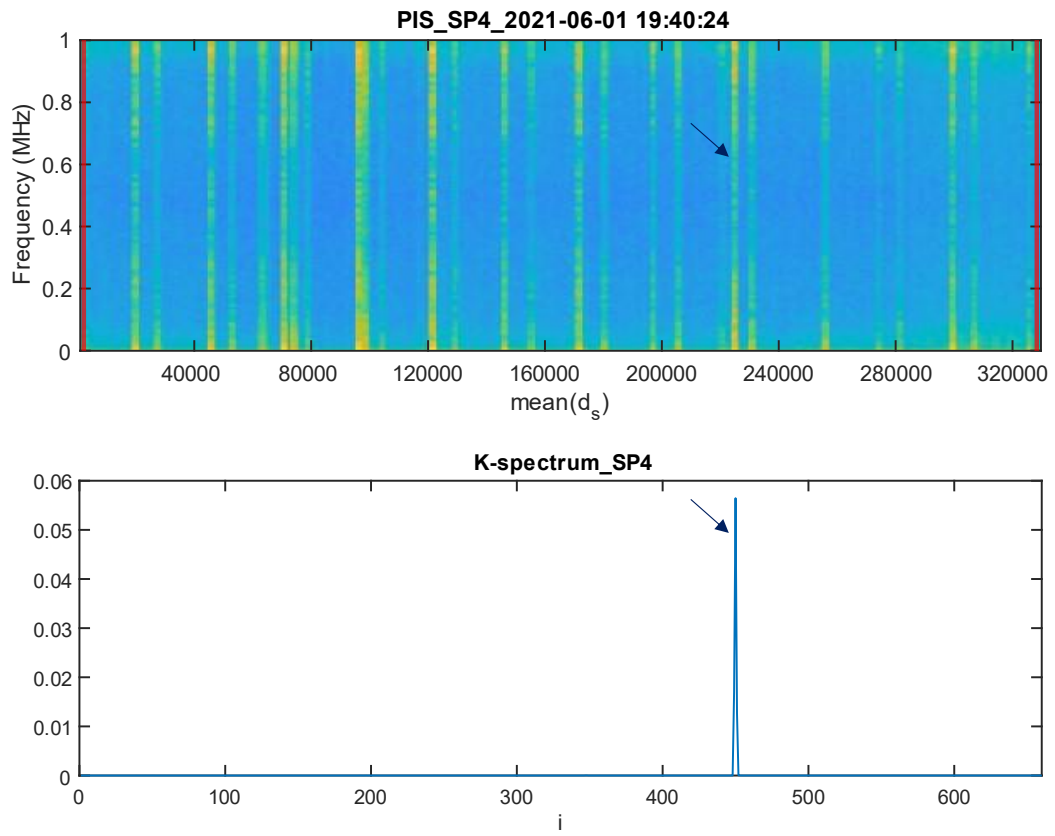
Figure 41, PIS verification, rotationPass, SP3.

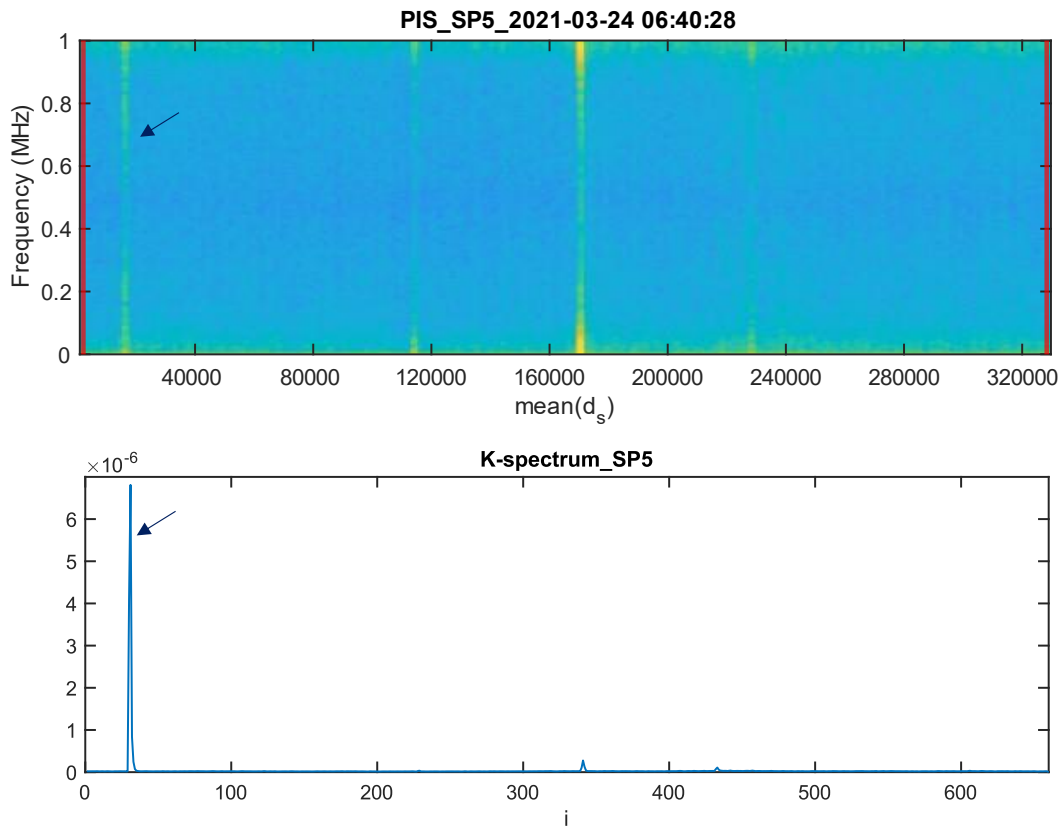Figure 42, PIS verification, SP4, rotatonPass.

Figure 43, PIS verification, SP5, rotationPass. As the other pulses in the PIS do not show up in the K-spectrum as aliases, this behaviour is confirmed.

4.2.3 Behaviour 3, BPFO

4.2.3.1 SP1 and SP2

The observed behaviour corresponding to $f_{fault} = 13.0209/rev$, is denoted BPFO (Ball Pass Frequency Outer), as it is suspected to originate from an outer race defect on the needle bearings. This will be explained further in section 5.1.4. The frequency estimation for f_{fault} was done same way as described in 3.6.3. Notice that, f_{fault} is *not* an integer. As expressed in section 3.6.1.2, the AE pulses corresponding to the BPFO will not be in the same axle position for each axle rotation. Recall that when f_{fault} is an integer, r_m is defined as the set of each starting position for every axle rotation recorded. When f_{fault} is *not* an integer, r_m is defined as the relative starting position for every g-th pulse. $d_s = r_{s+1} - r_s$, thus $mean(d_s)$ is a duration (in samples, n) containing g pulses. For the following PIS verifications, g is chosen to $g = 4$. That is, we will confirm that the 4 segments in the PIS contain one pulse each, at the same location.

L-time plots and detector decisions D_1 for SP1 and SP2 are presented in Figure 44. PIS verification of detector decisions D_1 for both sensors are displayed in Figure 45.
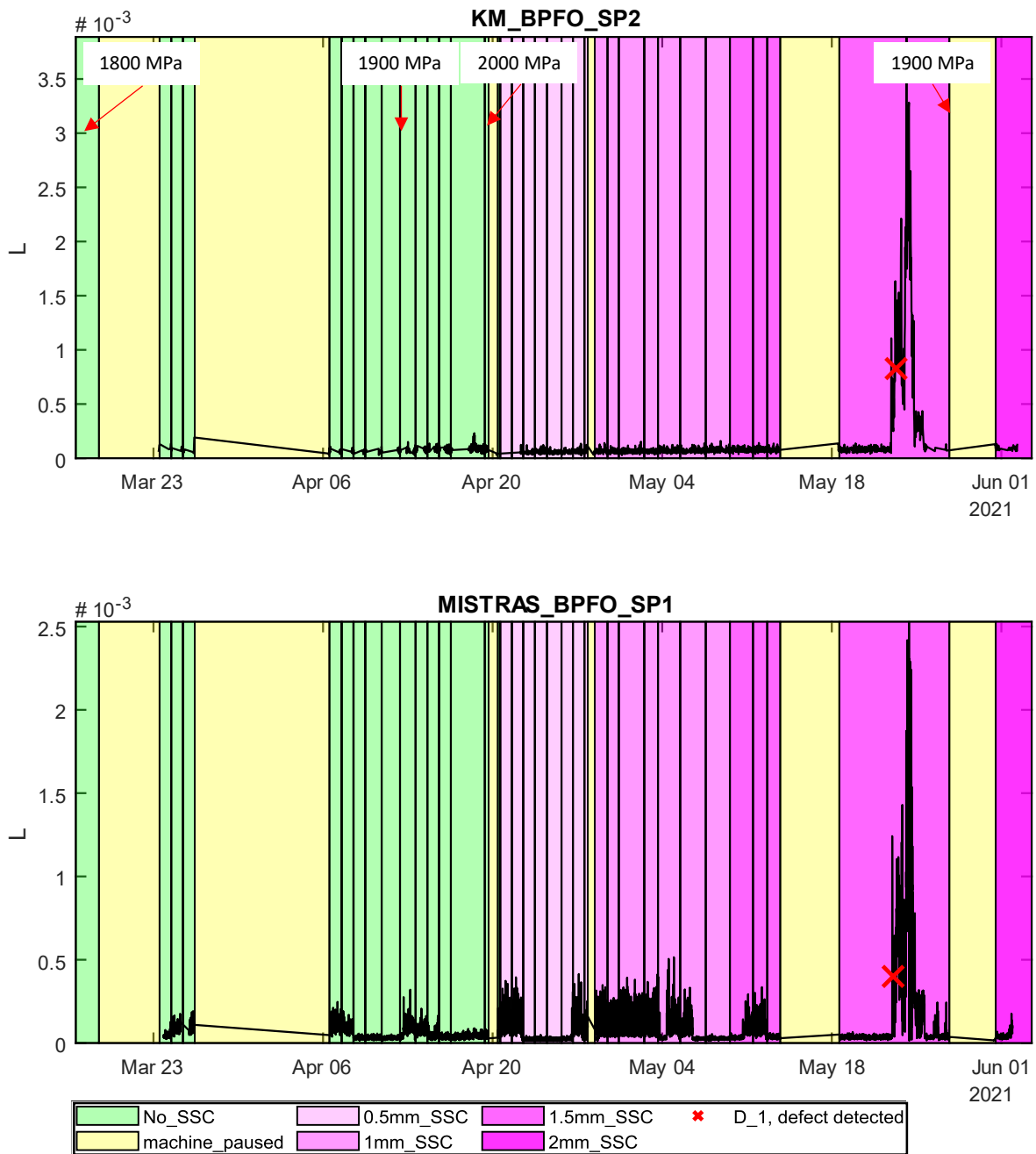
Figure 44, L-time plots for SP1 and SP2, BPFO.
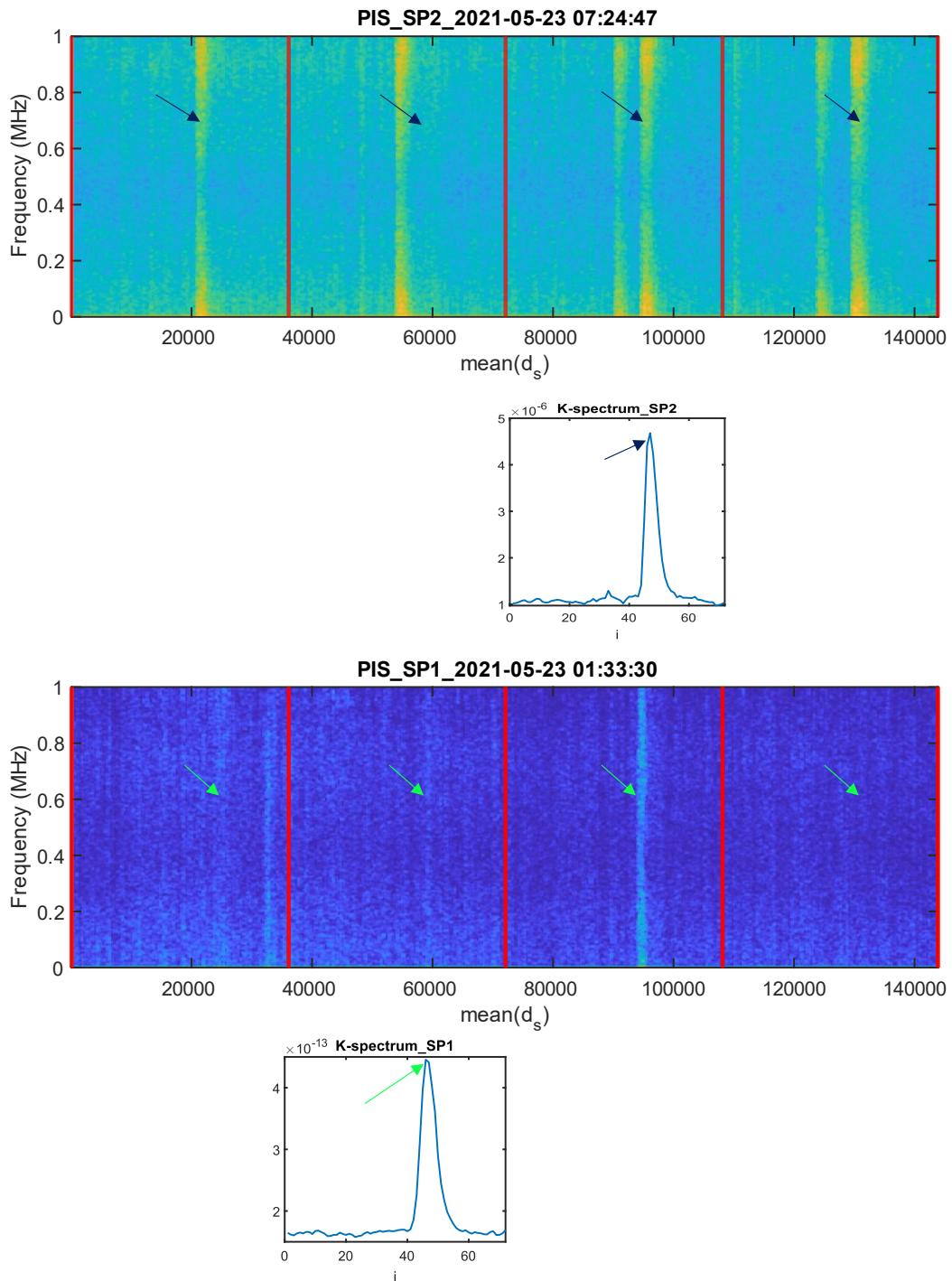
Figure 45, PIS verification, SP1 and SP2, BPFO. This verification is a bit harder to do. The integrated pulses vary in strength, but they appear consistently in the correct location.

4.2.3.2 SP3-SP5

The BPFO behaviour is the defect with the shortest distance to the SPx located on the given bearing housing. L-time plots are presented in Figure 46. In the figure, notice that all L-time plots are similar. However, SP4 is the sensor with the highest L-values. The first significant

peaks from all three sensors are chosen for PIS verification. They are marked with a data-tip-marker in Figure 46. PIS verifications are presented in Figure 47, Figure 48 and Figure 49.
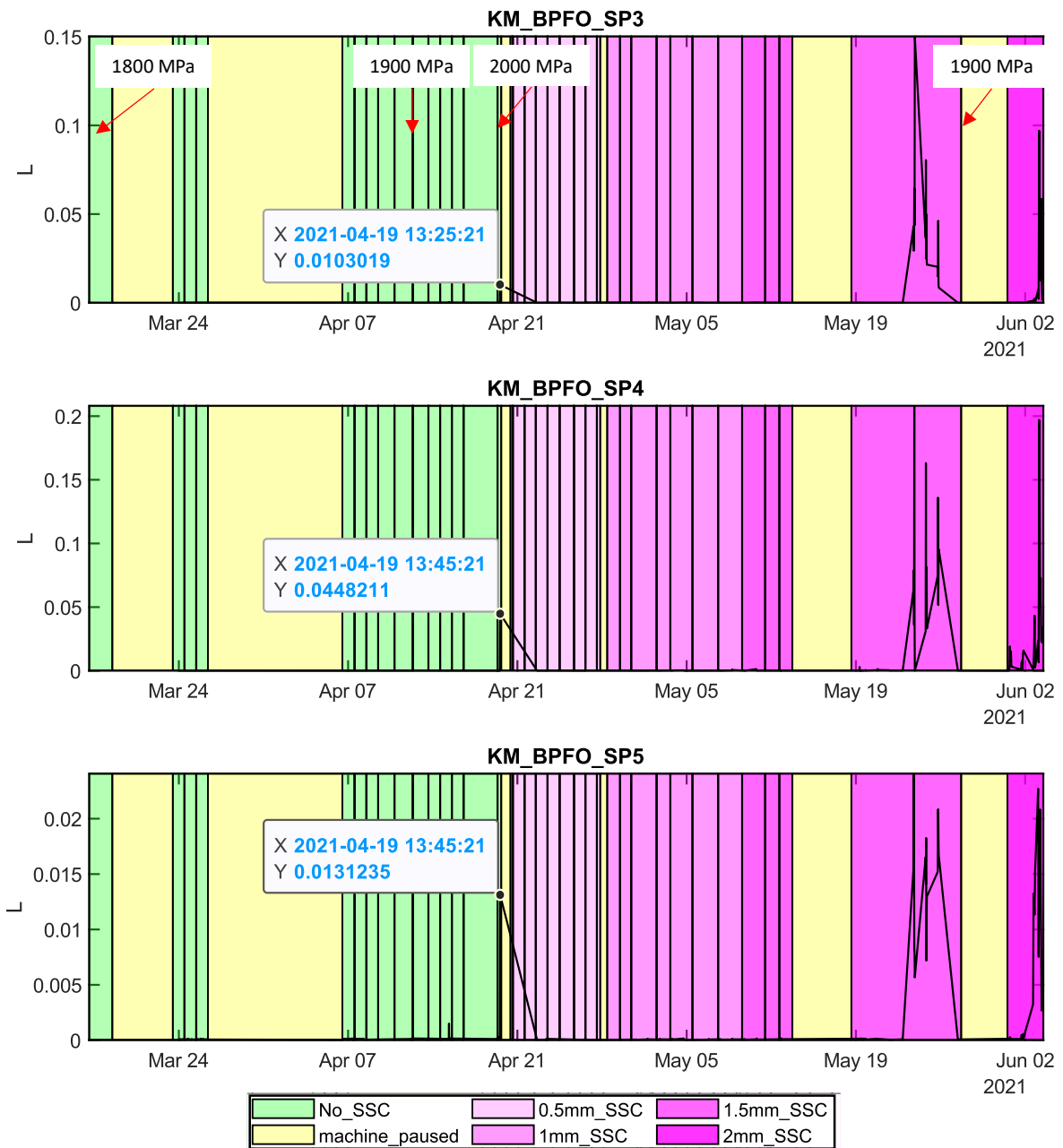
Figure 46, L vs time plots for SP3- SP5, BPFO.
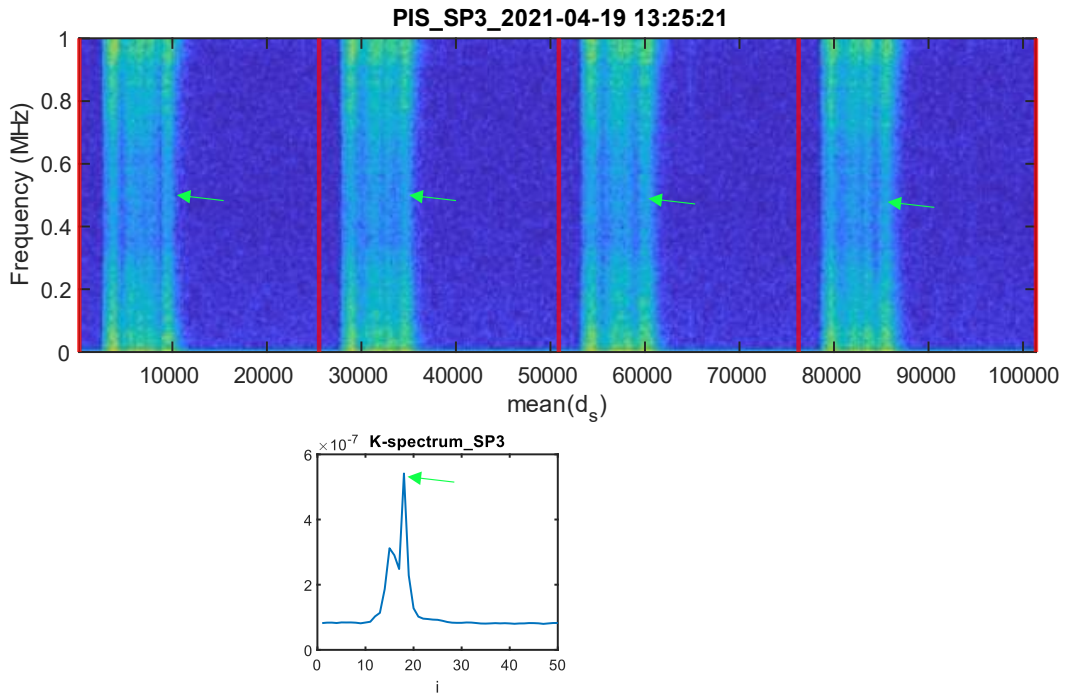
Figure 47, PIS verification for SP3, BPFO. The behaviour is consistent in all segments, but it is not a sharp pulse, as seen in previous PIS verification plots.
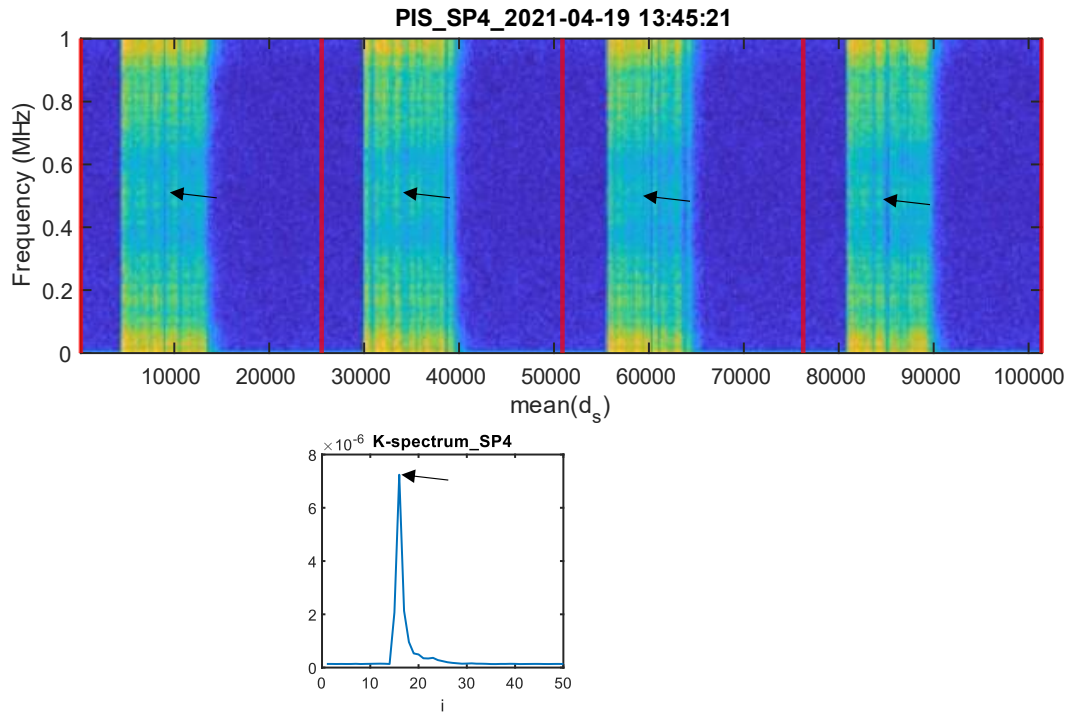
Figure 48, PIS verification for SP4, BPFO. The same, wide AE behaviour also happens here.
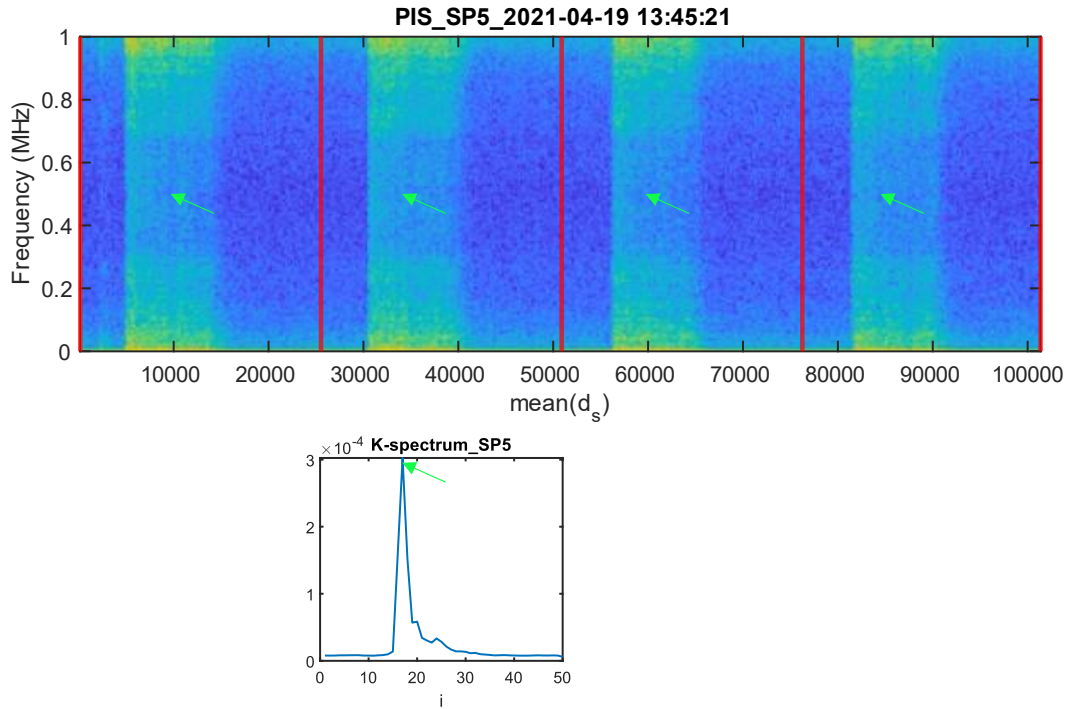
Figure 49, PIS verification for SP4, BPFO. The same, wide AE behaviour also happens here.

4.2.4 Behaviour 4, 100 Hz

4.2.4.1 SP1 and SP2

The observed behaviour corresponding to $f_{fault} = 100\ Hz$, is denoted *100 Hz*. Here, f_{fault} does *not* depend on f_r. For the following PIS verifications, the approach is the same as described in section 4.2.3. Here, g is also chosen to $g\ =\ 4$. That is, we will confirm that the 4 segments in the PIS contain one pulse each, at the same location.

L-time plots and detector decisions D_1 for SP1 and SP2 are presented in Figure 50. Notice that the L-time plot from SP1 displays an almost "on-off" process. This behaviour is not seen from SP2. For this reason, PIS verifications for SP1 is done for the first significant L. PIS for SP2 is done for the maximum L. These L-s are marked with black arrows in Figure 50. PIS verifications are presented in Figure 51.
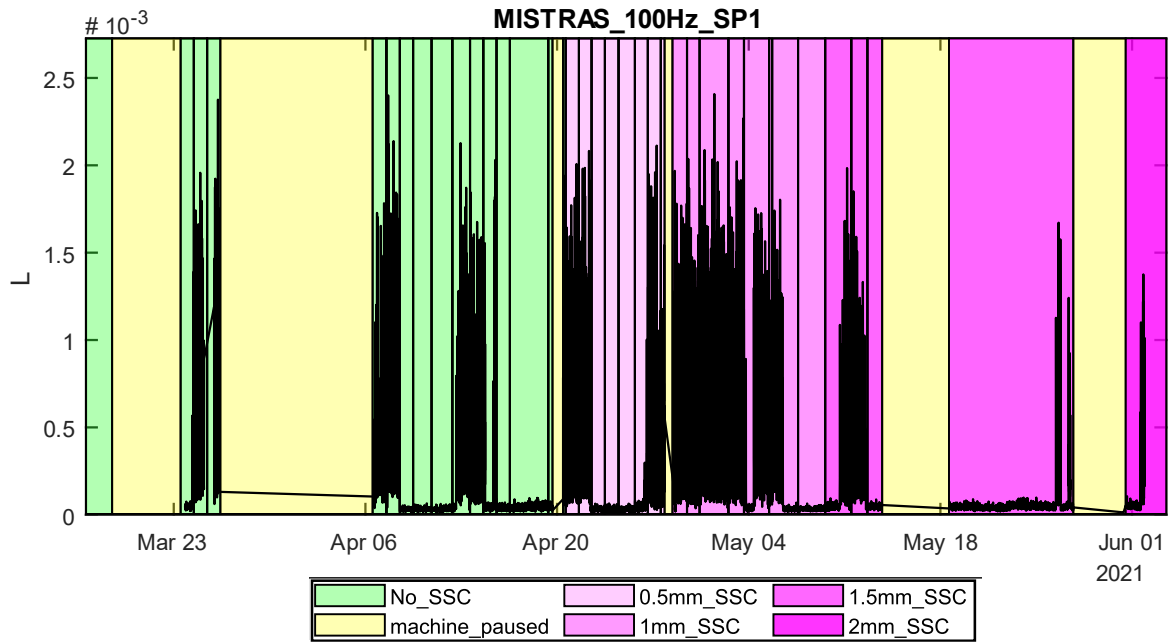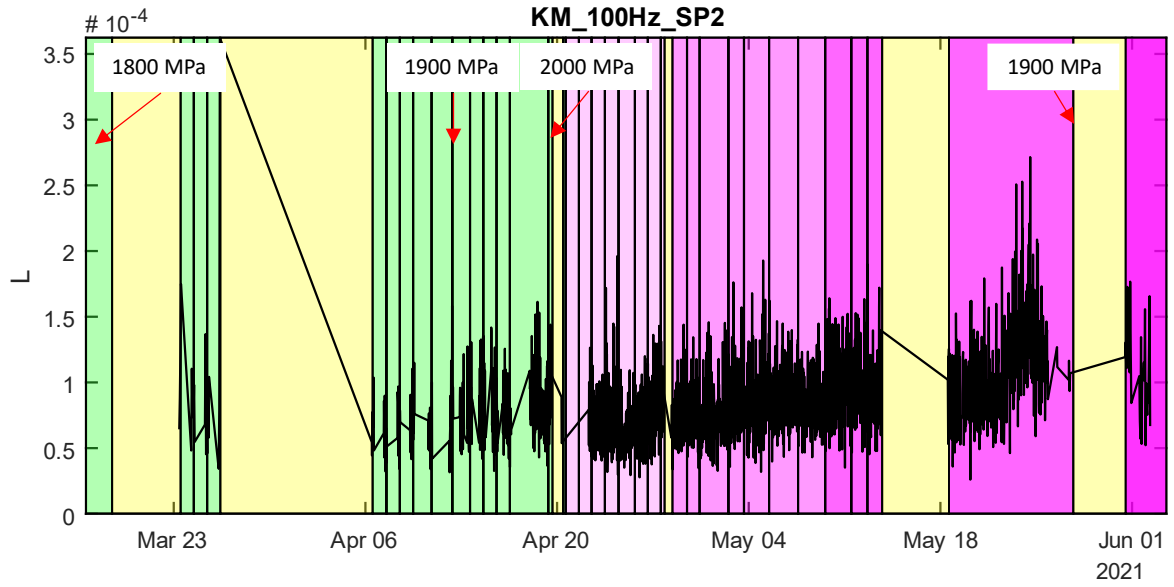
Figure 50, L-time plots for SP1 and SP2, 100 Hz. No defect was detected.
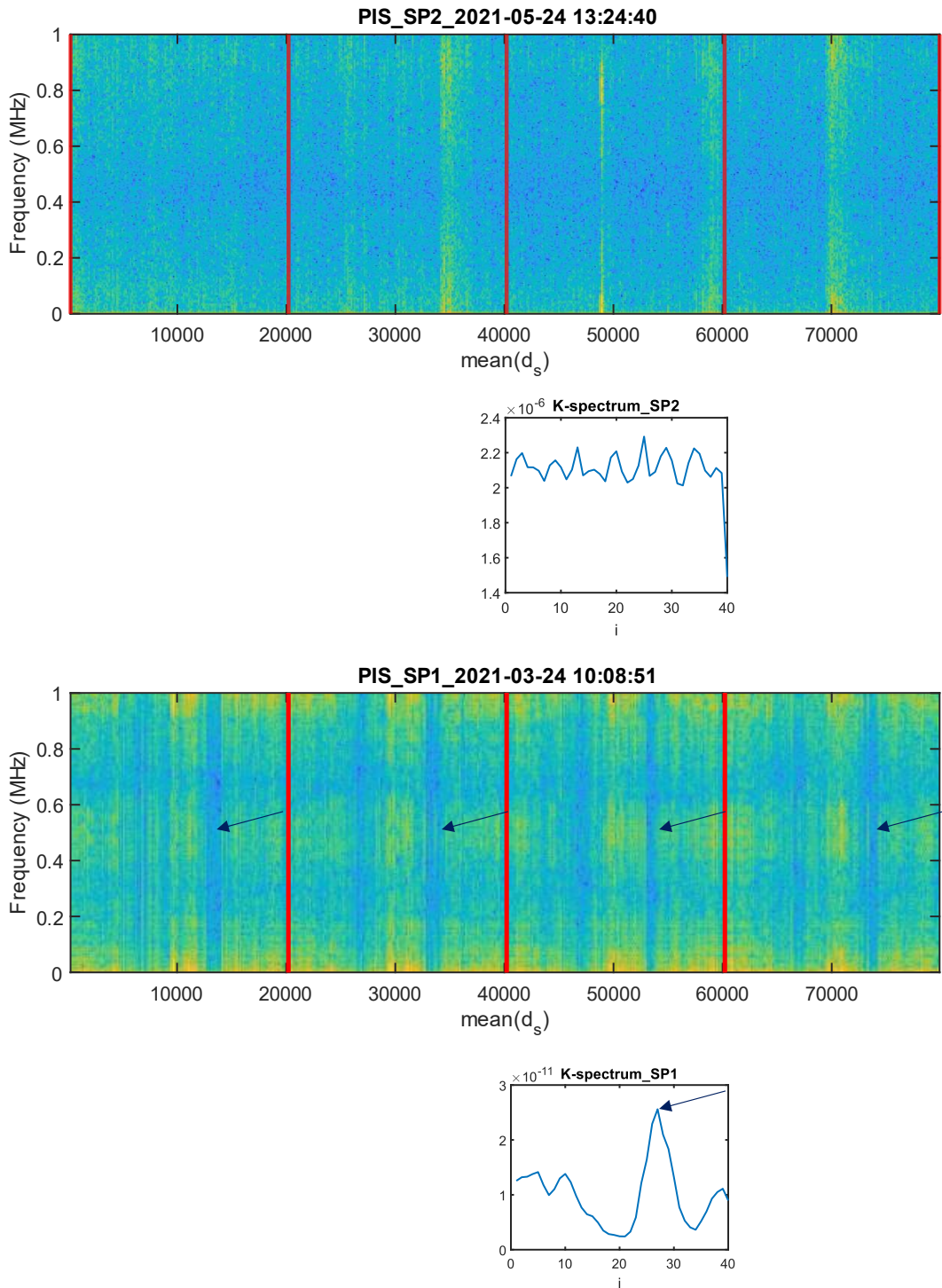
Figure 51, PIS verification for SP1 and SP2, 100 Hz. For SP2, no significant peak is discovered in the K-spectrum. The PIS does not provide a verification either. For SP1, the significant peak corresponds to a low spot in the PIS. This is the opposite of what to be expected from a defect originated AE pulse. Still, the pattern is consistent, and the defect is considered verified.

4.2.4.2 SP3-SP5

L-time plots from SP3-SP5 for the 100 Hz behaviour are presented in Figure 52. Notice that SP3 produced high L-s around March 24. The first significant L will be used for PIS

verification. This is marked with a black arrow in Figure 52. PIS verification for SP3 is displayed in Figure 53.
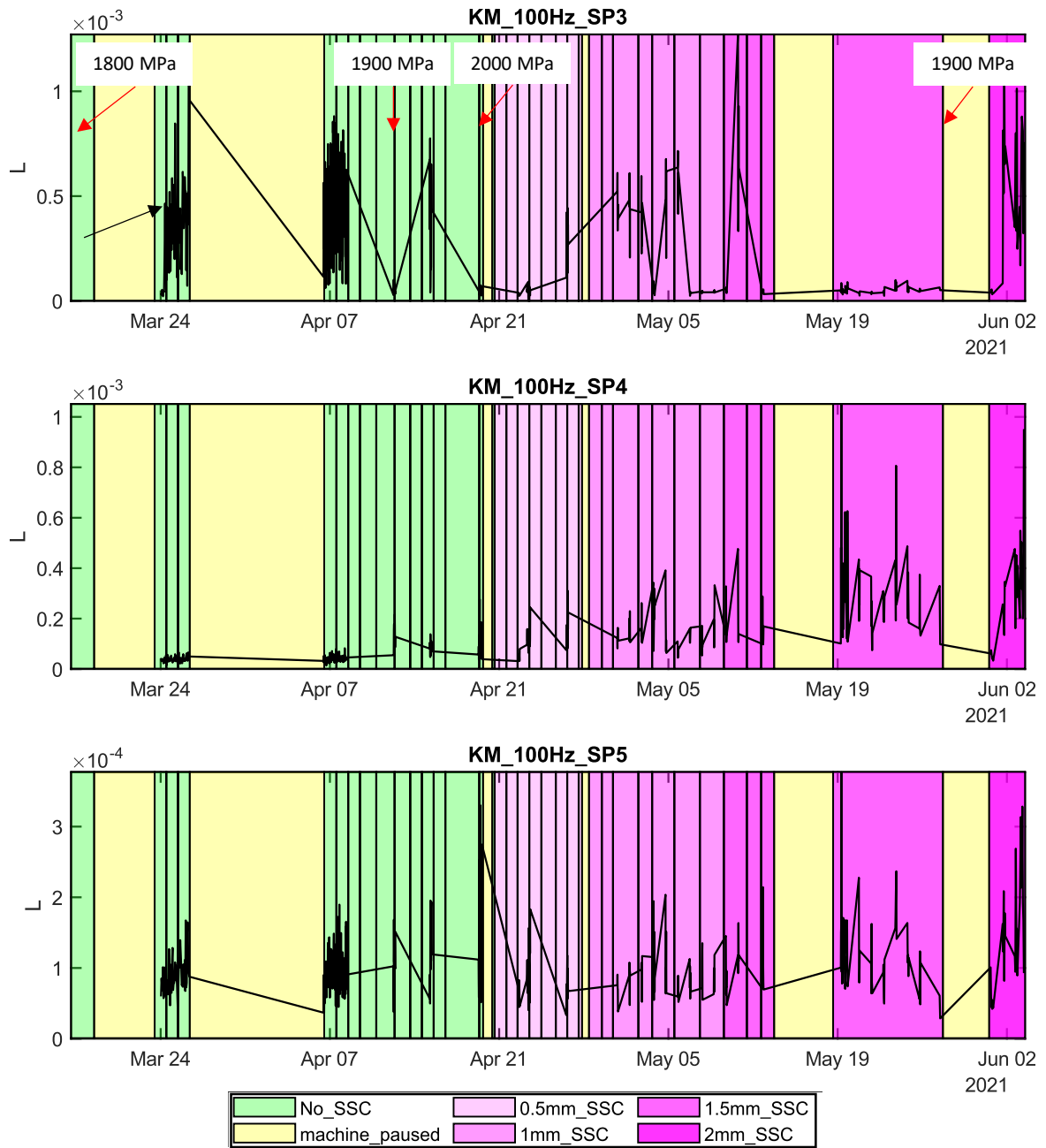
Figure 52, L-time plots for SP3- SP5, 100 Hz.
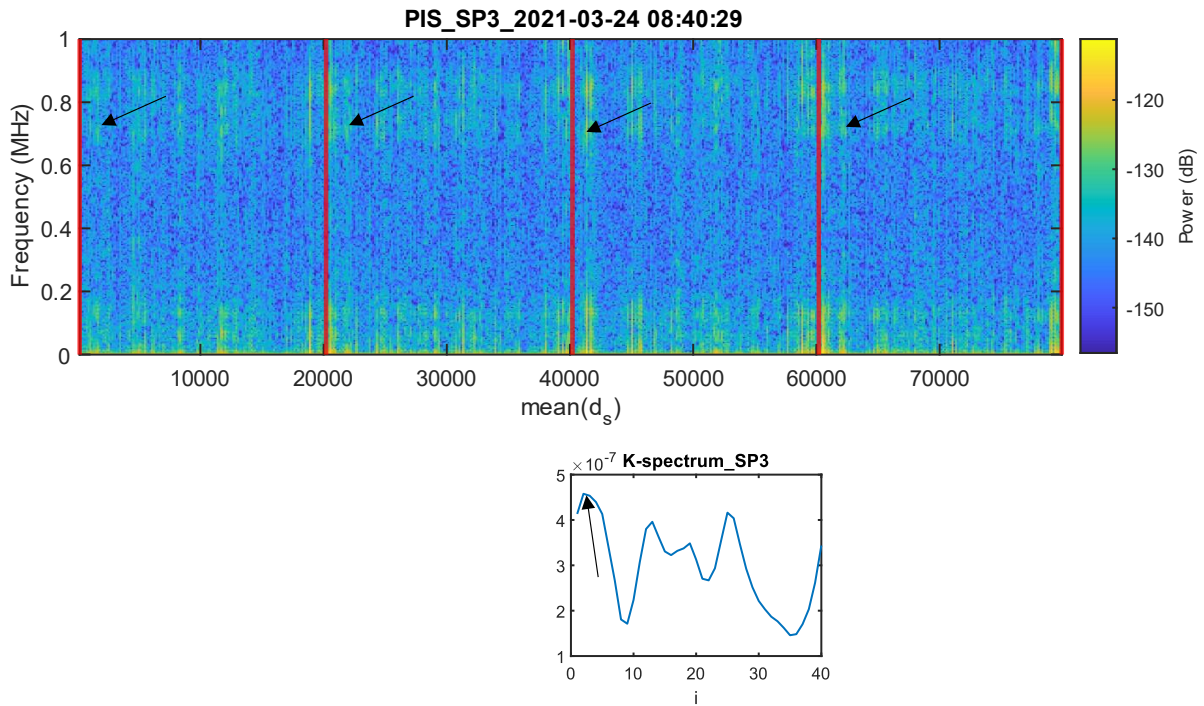
Figure 53, PIS verification for SP3, 100 Hz. The AE pattern does repeat stably in all segments, and the behaviour is confirmed. Notice that the peak with highest peakPower starts in $i = 36$ and ends at $i = 9$. This is an example of the edge case described in 3.6.1.7.

4.2.5 Behaviour overview, SP1 and SP2

To give a better overview of how observed behaviours have progressed during the duration test, two figures containing all observed behaviours for both SP1 and SP2 are presented in Figure 54 and Figure 55. RMS for every file (not high-pass filtered) are also plotted. This feature will be discussed in section 5.2.3. Notice that between May 18 and June 01, the rollerPass, rotationPass and BPFO behaviour all have high L-values from both SP1 and SP2. A PIS verification from SP2 is presented for all three behaviours in Figure 56, Figure 57, Figure 58.
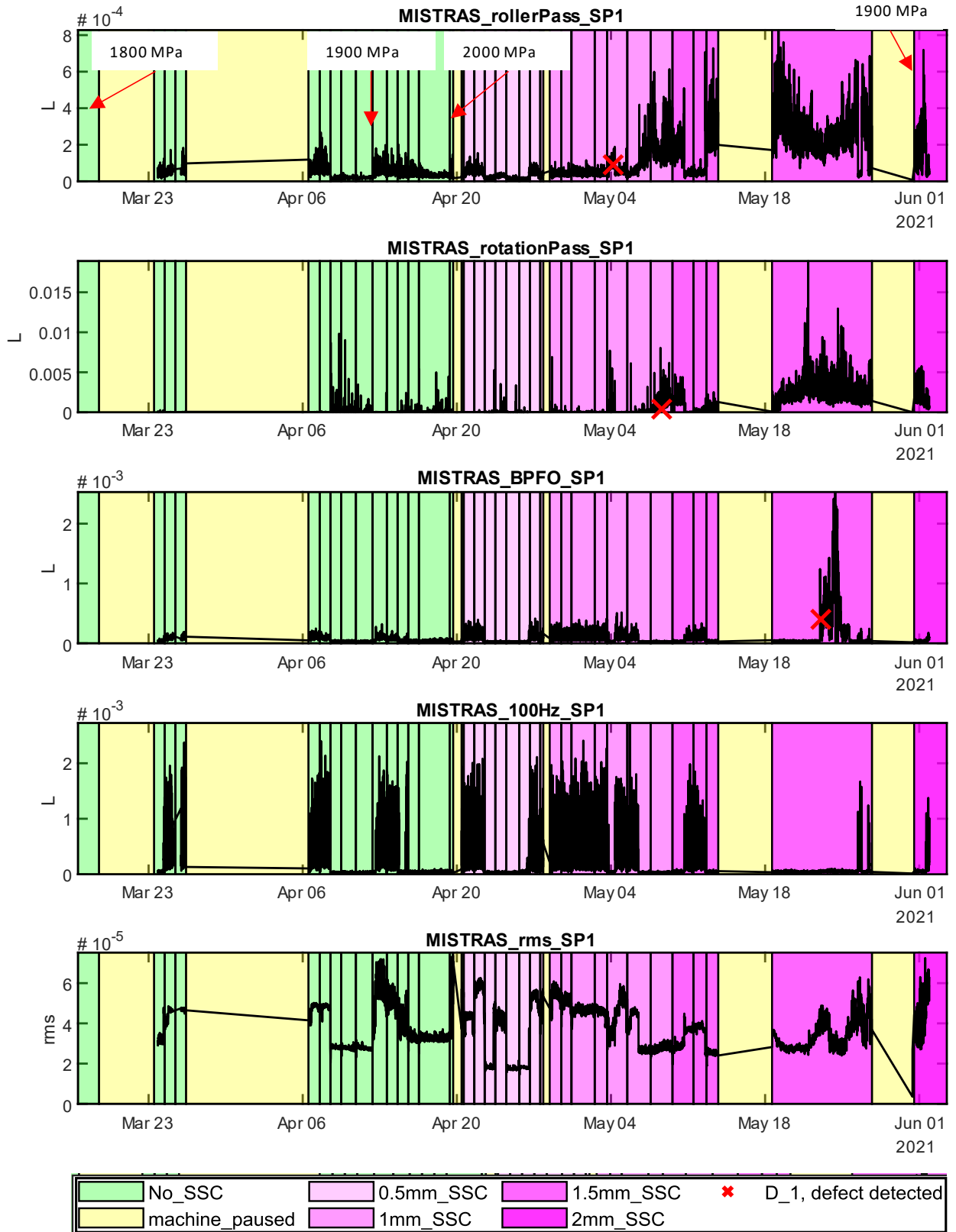
Figure 54, Overview of all observed behaviours, SP1. RMS is also included.
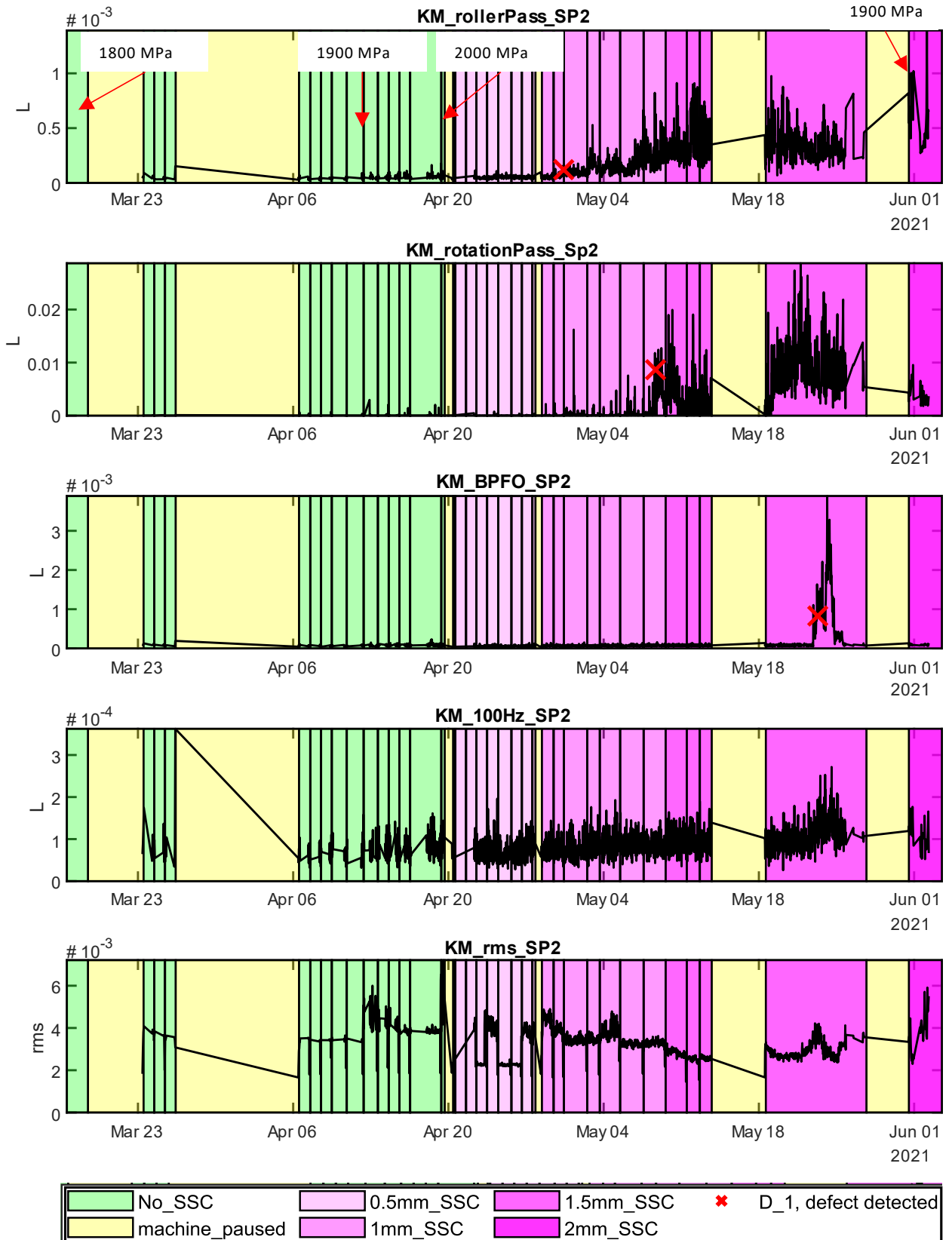
Figure 55, Overview of all observed behaviours, SP2. RMS is also included.
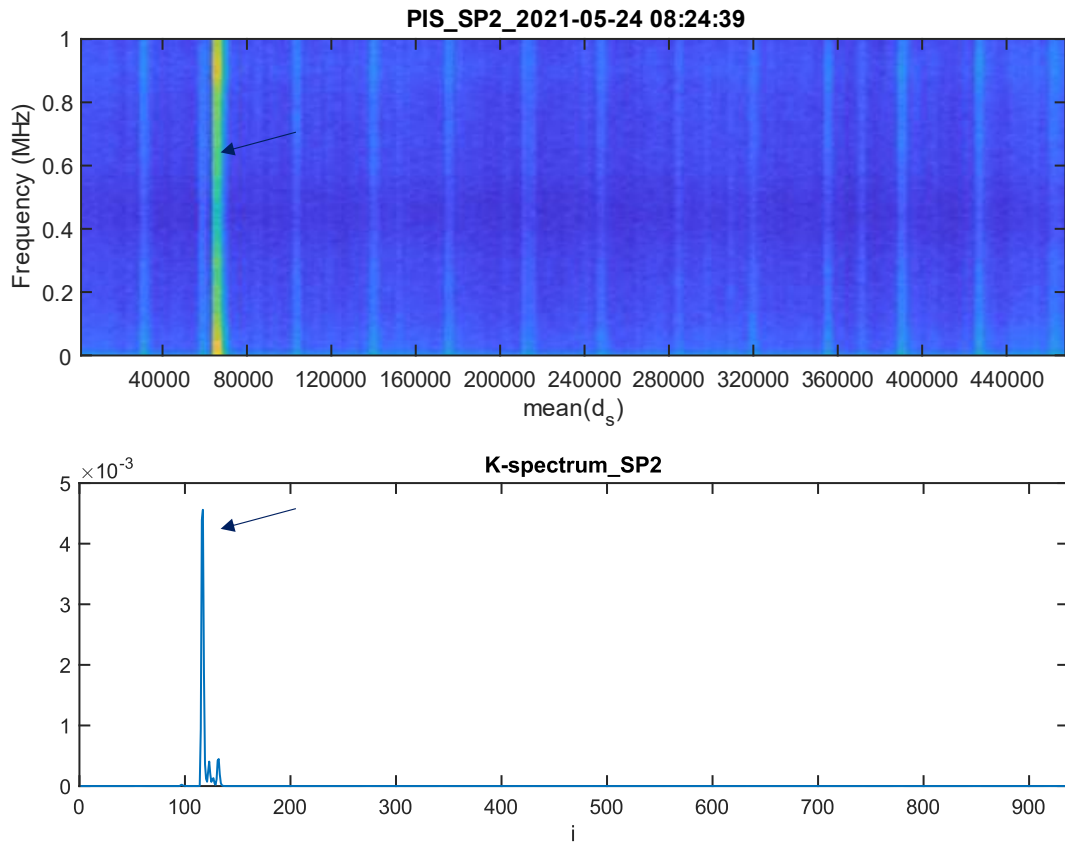
Figure 56, PIS verification, SP2, rotationPass.
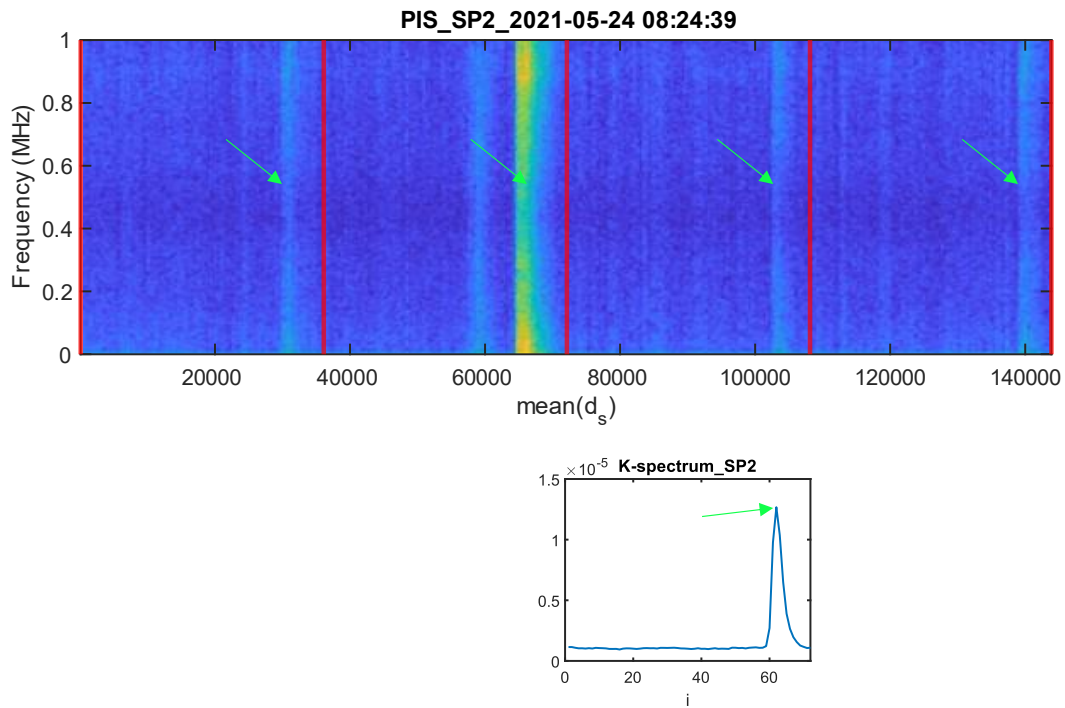
Figure 57, PIS verification for SP2, BPFO. In the second segment from the left, a pulse from the rotationPass behaviour has landed in the same location as the BPFO behaviour.
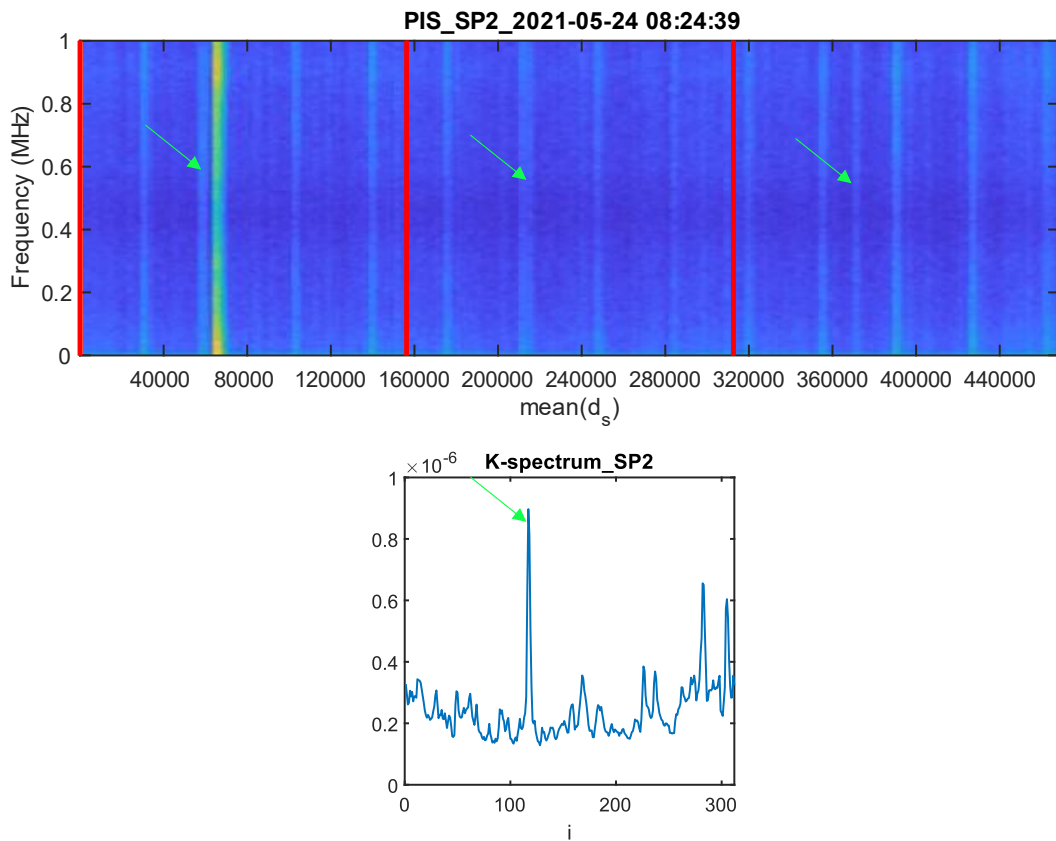
Figure 58, PIS verification, SP2, rollerPass. In the middle section, a pulse from the BPFO behaviour has landed in the same position as the rollerPass behaviour.

5 Discussion

5.1 Behaviour origins

5.1.1 rollerPass

AS described in section 4.2.1, the only place in the test machine where this behaviour can occur, is from a defect on the surface, or subsurface of the test specimen. To identify the origin of this behaviour, the only criteria needed are the results from the PAUT and salami-inspection described in 4.1. As described, no surface defects were found on the test specimen contact surface. Thus, one of the subsurface cracks observed in the PAUTs and the salami-inspection is the *confirmed* origin of the rollerPass behaviour.

5.1.2 100 Hz

This behaviour always repeats at $f_{fault} = 100Hz$. It did not change when the F_A was reduced from $F_A = 364RPM$ to $F_A = 256RPM$, 20 April 2021. Thus, this behaviour does not depend of F_A (and thus f_r). The only origin that can cause this behaviour is a full wave rectified alternating current (AC) source. In Europe, the AC current has a frequency of 50 Hz. This behaviour was most dominant in SP1. However, it was also present in SP3, but *not* SP2. This means that the source cannot be something that would affect all SPx, such as the motor controller. It is not something that would only affect one system either. The PAC 2/4/6 preamplifier (Appendix F) is used for on all SPx. It requires a supply voltage between 18-28V DC. The power supply used to deliver the DC current to the PAC 2/4/6 preamplifier, is built into the PCI-2. This built in power supply *rectifies* the AC current. If this power supply is defective, the output DC voltage could be contaminated with 100 Hz noise. Given these facts, the suspected source of the 100 Hz behaviour is a defective power supply built into the PCI-2 board. At the time this thesis was delivered, this had *not been confirmed*.

5.1.3 rotationPass

This was the most unpredictable behaviour observed during the duration test. Additionally, it seemed like it was turned on and off. The variation in pulse-to-pulse distance was so large that in order to detect it, the *outlier removal* step (ref 3.6.1.5) had to be turned off. This of course increases the probability of unrelated AE pulses influencing the decision making. However, the pulses originating from the rotationPass were so dominant, that the influence of unrelated pulses was assumed insignificant. An example of this can be seen in Figure 23. The file used for presentation contains the rotationPass behaviour, and the detector seeks for a behaviour with $f_{fault} = 1/rev$. However, there is no peak in the K-spectrum from the rotationPass. The reason is that the *outlier-removal* step was turned *on*. This made the aliasing problem easier to visualize. An example of how this K-spectrum looks without *outlier-removal* is presented in Figure 59.
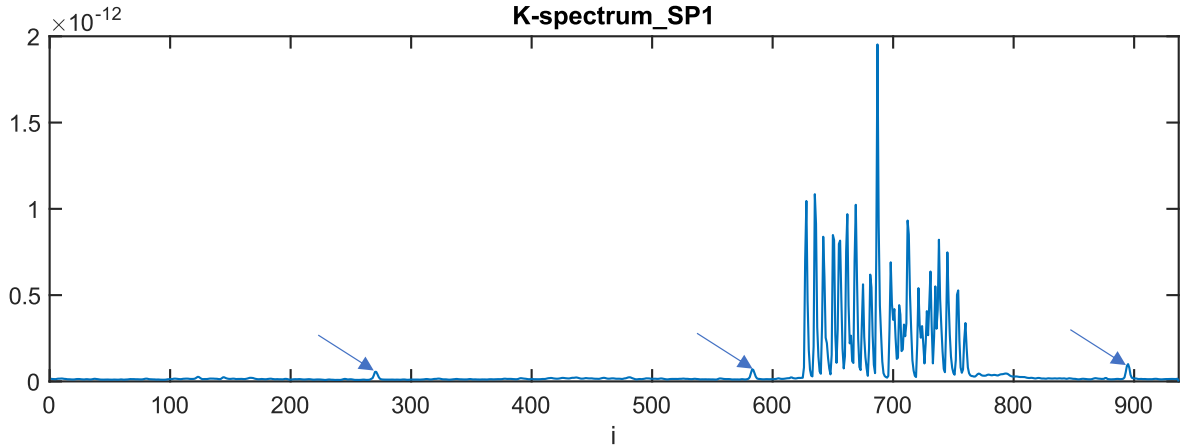
Figure 59, This K-spectrum illustrates the extreme character of the rotationPass behaviour. The aliases from the rollerPass behaviour are marked with blue arrows.

In Figure 59, the rotationPass peaks are multiple times higher than the rollerPass peak aliases. It has also been recognized in 150 windows. Given the chosen $l_w = 1000$ and $o_w = 500$, this means that relative peak position in each recorded axle revolution varied $(1000 - 500) *$ $150 = 75000$ samples. That is 37.5 ms. Given that each axle rotation takes 234 ms at $F_A = 256RPM$, this variation is substantial.

This behaviour does *not* originate from a weak signal, hidden in noise. Thus, the proposed detector is not made to detect signals like this. However, it demonstrates how robust the proposed detector is, and the importance of the *outlier-removal* to distinguish different behaviours occurring simultaneously in the AE waveform.

No confirmation about the origin of this behaviour was available by the time this thesis was delivered. The fact that it had maximum L-values three completely separate places during the duration test for SP3-SP5 (Figure 40) might even imply that there are more than one cause to this behaviour.

5.1.4 BPFO

The ball pass frequency outer, BPFO is the frequency of which a rolling element passes a defect on the outer race in an REB. It can be calculated as,

$$BPFO = \frac{N_B}{2}\left(1 - \frac{B_D}{P_D}\right),$$
<div align="right">30</div>

where $P_D = \frac{D_1 + D_2}{2}$, N_B is the number of rolling elements, D_1 is the outer race diameter, D_2 is the inner race diameter, and B_D is the rolling element diameter.

For the needle bearings (Appendix C and Appendix D) used in the test machine, the BPFO is 13.1765/rev. The reason the measured BPFO is $f_{fault} = 13.0209/rev$, is believed to be caused by a slightly larger circumference of the test specimen, compared to the support rollers.

Recall the first time the machine stopped due to excessive vibration. This happened April 19, 2021 (ref Table 2). The *only* observed behaviour that increased significantly that day was the BPFO. This behaviour change was visible in SP3-SP5 only (see Figure 47, Figure 48 and Figure 49) The behaviour visible in these PIS verifications is not crack related activity. It could be friction. Ultimately, it is believed that a defect was made to the outer race of one or several needle bearings that day. No confirmation about the origin of this behaviour was available by the time this thesis was delivered

5.2   Overview

5.2.1   SP2

From Figure 55, some properties can be identified. The rollerpass behaviour is the only behaviour that correlates with recorded SSC width. As this behaviour is confirmed as an SSC, this is a good result. rollerPass and rotationPass, might look like that they are correlated, but they are not. An example can be seen June 01, 2021, where the rotationPass suddenly drops in L-value, while the rollerPass continues at an increasing rate seemingly proportional to the SSC width.

Also, notice how unaffected the BPFO are to all recorded behaviours. This is a good indicator that the detector indeed manages to isolate distinct behaviours.

5.2.2 SP1

The most important fact to note about Figure 54, is that *all* observed behaviours were correlated with the 100 Hz noise behaviour. For the rotationPass, the *normalizing*-step (ref 3.6.1.10) works as intended. Notice that every time the 100 Hz noise turns on, the L-values for the rotationPass drops to nearly zero. This goes to show that, whenever there are noisy components of this magnitude in the AE waveform, we simply cannot trust the detector results (unless they are verified in the PIS). For the rollerPass, this step also works as intended, *after* the defect was declared detected. Notice that on May 04, 2021, the noise suddenly went off for a few hours, and the SSC was detected. Between May 04 and June 01, whenever the noise is on, the L-values for the rollerPass drops, which it should. Between March 23 and May 04, the opposite happens. The reason for this is unknown, and neither the contact pressure, or F_A seems to be the cause.

In case it was not clear from the discussion, the reason SP2 detected the SSC before SP1 was because SP1 were influenced by noise. One last important point to note is that the L-time plots for all observed behaviours are unaffected by the process involving PAUT. The *only* parameter that is influenced by PAUT, is the RMS.

5.2.3 RMS

The RMS (Root-mean-square) of the non-high-pass filtered waveform, $x[n]$, is included for both systems to prove a point. This is a parameter typically used for *feature extraction* in various machine learning based problem solutions. Notice that here, it does not correlate with *any* of the L-time plots. What this means is that if a classification model was to be based on the RMS feature, given the data from this duration test, it would not classify any of the observed behaviors correctly. Would RMS be able to classify a behavior that has *not* yet been identified in the duration test? Maybe, but if so, we would have *no* way of verifying the classification results.

5.3   Confirmation

5.3.1   The 3-stage confidence process

The process of confirming the output from a CBM system targeting early SSC activity in the AE waveform, can be described as a 3-stage process. That is

(1) **Detection:** The detector returns decision D_1, *a defect is detected*.

(2) **Verification:** The L that caused the decision is inspected (manually or automatically) to *verify* that the sought defect behaviour triggered the detector decision.

(3) **Confirmation:** The RM component is physically inspected to *confirm* that the detected defect is physically present.

In the paper by (Price et al., 2005), the confirmation can be considered a stage-1+3 confirmation. The detector, in this case a human monitoring the real-time time-frequency representation of the AE waveform, noticed a sudden change in the waveform during testing. This change was not verified any further, and thus stage-2 was skipped. Stage-3 was then confirmed by a physical inspection of the defected component.

The rest of the reviewed literature in this thesis can be considered as stage-1 confirmation *only*. It is thus hard to extract information about the reliability of the presented methods used to detect SSCs in REBs. All reviewed papers conclude that they have detected the presence of an SSC in the AE waveform. However, due to their stage-1 result confirmation, some of the methods used, directly contradict one another. As described in section 2.3.3, (Price et al., 2005) stated that in order to monitor wear at an early stage, analysis of continuously sampled AE waveforms are needed. (Fuentes et al., 2020) however, concluded that they had successfully detected SSCs in REBs using AE *hit-based* feature extraction only. If the detector proposed in this thesis had utilized *hit-based* feature extraction, instead of pulse integration, the only detected behaviour would be the rotationPass. All the other behaviours would have been hidden, especially the rollerPass, due to the high amplitude pulses from the rotationPass behaviour. In other words, the statement by (Price et al., 2005) is correct. The detector suggested by (Fuentes et al., 2020) would not work for the data used in this thesis. This is a consequence of non-verifiable results.

5.4   Detectors and classifiers

There is a good reason why most radars to this day do not rely on machine learning to detect targets. In the 1950s and 1960s the theoretical effort was made to solve the radar target detection problem. Fundamental performance limits were found. The theory describing how to effectively detect weak pulses in noisy waveforms is still used today.

5.4.1   The verification dilemma

One problem using machine learning to detect SSC related activity in the AE waveform, lies in stage-2, *verification*. Machine learning models, and especially deep learning models, typically represent a "black box" type system. A typical machine learning model takes an input x and maps it to some output y, and the system developer has hardly any insight to what the system does. The only thing the system developer knows, is the *correct answer*. To ensure that the system does what it is supposed to do, the system developer must verify that the output y is the correct answer. This process is called *supervised learning*. Fully connected neural networks (FCNNs), residual networks (ResNets) and convolutional neural networks (CNNs) are all known supervised learning models.

If the system developer does not know the answer, the only valuable option machine learning offers is the process called *unsupervised learning*. Here, the system developer has a collection of data x that is believed to be *normal*. The machine learning model can then train to replicate these data. After the training has finished, the model should be able to recognise familiar input data. If the input data is *unfamiliar*, the model will output some error proportional to how unfamiliar the data is. The system developer then has a tool that can recognise abnormal data from a dataset that neither the system developer nor the model knows anything about. An example of this type of machine learning model is the autoencoder. This can be based on both FCNNs and CNNs.

A great application to machine learning is the field of computer vision. Consider a machine learning model, a CNN for example. We want to make a *classifier*, able to recognize images of cats and dogs. The model is trained on images of dogs and cats taken at different angles, environments, lighting conditions, and distances. After the training is finished, the model can receive input images that it has never seen before, and predict whether a cat or dog is present,

with a certain success-rate. This model has now *derived the mathematical description* of what an image of a cat and a dog is. This is an extremely complex task that may be close to impossible to do manually.

However, the most important part of this process is that the system developer still knows more about the input data than the classifier. We know what images of dogs and cats look like. If the model guesses wrong, we would be able to tell immediately. This is not the case with AE waveforms recorded from an RM containing SSCs. We generally know close to nothing about what information is hidden beneath the noise in this sample vector. If we train a machine learning classifier to recognize SSCs in an AE waveform we are *unable to verify* that the model output is correct, by simple means.

The analysis of the duration test has shown that complicating processes such as noise, friction, multiple occurring defects with different magnitude, and aliasing problems all contribute to an AE waveform that is complex. So complex, that even if a subsurface defect is known to be present, the detector decisions must still be verified. For a machine owner, a CBM system that outputs: "Something might have happened in your RM" is hardly valuable information. If this problem continues to be solved with non-verifiable machine learning, it will most likely remain a lab experiment.

6 Conclusion and Further Work

6.1 Suggestions for future improvements

6.1.1 Learnable peak characteristics

The intention of the proposed detector in this thesis is not to indicate that all use of machine learning is insufficient. If it does not compromise with verifiability, it can be a useful tool. One suggested way to implement a machine learning part in the detector is to replace the peakPower with some learnable parameter that can have a better opinion about a peaks character than just the width and the prominence. Because the peaks are in the K-spectrum, a parameter space where we can tell what is going on (like a picture of a cat), verifiability can still be preserved using PIS verification.

An important observation to note about an SSC originated behaviour in the AE waveform is that the corresponding peaks in the K-spectrums are extremely sharp. This confirms that the f_r was properly estimated, but it also confirms that the pulses are short. So short that they only register in 4-6 consecutive windows (with 50% overlap). Peaks that originate from electrical noise are wide. There are probably more qualities to the K-spectrum peaks that are worth investigating. Perhaps the origin of an observed behaviour, being a surface or a subsurface defect, can be classified from learned peak characteristics.

6.1.2 Frequency scanner

The proposed detector relies on extremely narrow tolerances for f_{fault} (the BPFO for example). The tool used to achieve this (ref section 3.6.3) could be further developed to a frequency scanner. Machine owners wanting to invest in the system proposed in this thesis might not know the exact f_{fault} for every failure related frequency in their RMs. An onsite estimation of the failure frequencies would be a desirable solution to this problem.

6.1.3 Real-time applications

The proposed detector is intended as a real-time condition monitoring system. This is not a thesis in computer science and thus the computational complexity of the proposed detector will not be described. However, some indicating measurements of performance are described below:

- The execution time for 100 consecutive detector executions including a high-pass filtering of the entire input signal for *every* execution, given:
  $l_{signal} = f_s 10s, f_{fault} = 3, l_w = 1000, o_w = 500$, and $x_{HP} = highpass\{x[n]\}$.

Is measured to $t_D = 33.44s$. The average time duration for each execution is thus $t_d = 0.334s$

- The execution time for 1000 consecutive detector executions, given
  $l_{signal} = f_s 10s, f_{fault} = 3, l_w = 1000, o_w = 500$.

Is measured to $t_D = 65.02s$. The average time duration for each execution is thus $t_d = 0.0650s$

6.1.4 The most significant failure

As of now, the detector only extracts the peak in the K-spectrum with the highest peakPower. What this means is that if there exist multiple instances of the same defect in an REB, only the most developed defect is chosen by the detector. This is not necessarily a bad but could be addressed as a potential for improvement.

6.1.5 Assumptions

A lot of assumptions have been made in this work for the parameters window length, window overlap, definition of T and confidence c. These parameters where chosen through trial and error and the parameters that produced the best results are presented in this thesis. There are lots of room for improvement here, and several of the parameters, for example window length l_w can be investigated to improve probability of detection p_D.

6.1.6 Rotation frequency

The fact that a fixed estimated f_r proved sufficient for pulse integration with $l_w = 1000$ on a signal that is 20,000,000 samples long is almost unbelievable. This means that for the entire duration test, the machine operated with an f_r that deviated less than 0.001 Hz (ref 3.6.3) during every single axle rotation of the total 22.195.088 axle rotations completed. This is nothing less than remarkable and is a big compliment to SINTEF who built the machine. If the estimated f_r deviates more than 0.001 Hz from the true f_r, given a $l_w = 1000$ the detector will be useless. If this had happened in the results presented in section 4.2, it would have been clearly visible.

Luckily it did not, but in order to use this detector in a real machine, which can operate at varying rotation frequencies, the axle positions r_m *must* be based on sampled axle position data. The bare minimum way to a to do this is to use a rotation counter synchronously

sampled with continuous AE sampling. A better solution is to use a precision rotary encoder. With sampled axle position data, the full potential of the general encoder described in 3.6.1 can be utilized. This is the reason why the general solution for the detector, including d_s, is described in this thesis. It is the *only* solution that would work in a real machine outside the lab. Thus, this is the future improvement that should be implemented first.

6.2 Conclusion

As a laboratory test with the intention to solely generate AE waveforms containing RCF induced SSC pulses, the duration test might be described as a flawed test. All the observed behaviours and the unintended machine stops should, in a lab context, not have been present. However, as an acid test for a proposed detector with real world ambitions, the duration test was appropriate for the purpose.

This master thesis was written during the duration test. As more data became available and more behaviours were observed, the algorithms used were constantly developed to cope with the new findings. The result is a proposed detector with a bigger picture in mind. It is by no means a finished prototype, but it is built on well-established theory derived from radar technology. The main quality attributes are robustness and verifiability, which are vitally important for a system that potentially is used to monitor heavy expensive rotating machinery.

These quality attributes have not been prioritized by previous research aiming to solve the problem of SSC detection using AE. This is the main reason why this field of research has hardly progressed in 16 years. It is therefore time to establish a criterion of confidence that ensures that future research publications do not claim success based on unverifiable results. That is, *The 3-stage confidence process*.

7 References

Blake, L. V. (1986). *Radar Range-performance Analysis*: Artech House.

Cockerill, A., Clarke, A., Pullin, R., Bradshaw, T., Cole, P., & Holford, K. M. (2016). Determination of rolling element bearing condition via acoustic emission. *Proceedings of the Institution of Mechanical Engineers, Part J: Journal of Engineering Tribology, 230*(11), 1377-1388. doi:10.1177/1350650116638612

Eitzen, D. G., & Wadley, H. (1984). Acoustic Emission: Establishing the Fundamentals. *Journal of research of the National Bureau of Standards, 89*, 75-100.

Elforjani, M., & Mba, D. (2010). Accelerated natural fault diagnosis in slow speed bearings with Acoustic Emission. *Engineering Fracture Mechanics, 77*(1), 112-127. doi:https://doi.org/10.1016/j.engfracmech.2009.09.016

Esmaeili, K., Zuercher, M., Wang, L., Harvey, T. J., & Holweger, W. (2017). *Advanced signal processing techniques for wind turbine gearbox bearing failure detection.* Paper presented at the WCCM 2017 - 1st World Congress on Condition Monitoring 2017.

Fuentes, R., Dwyer-Joyce, R. S., Marshall, M. B., Wheals, J., & Cross, E. J. (2020). Detection of sub-surface damage in wind turbine bearings using acoustic emissions and probabilistic modelling. *Renewable Energy, 147*, 776-797. doi:10.1016/j.renene.2019.08.019

Fuentes, R., Howard, T. P., Marshall, M. B., Cross, E. J., & Dwyer-Joyce, R. S. (2016). Observations on acoustic emissions from a line contact compressed into the plastic region. *Proceedings of the Institution of Mechanical Engineers, Part J: Journal of Engineering Tribology, 230*(11), 1371-1376. doi:10.1177/1350650116638590

Geng, Z., Puhan, D., & Reddyhoff, T. (2019). Using acoustic emission to characterize friction and wear in dry sliding steel contacts. *Tribology International, 134*, 394-407. doi:https://doi.org/10.1016/j.triboint.2019.02.014

He, Y., Li, M., Meng, Z., Chen, S., Huang, S., Hu, Y., & Zou, X. (2021). An overview of acoustic emission inspection and monitoring technology in the key components of renewable energy systems. *Mechanical Systems and Signal Processing, 148*, 107146. doi:https://doi.org/10.1016/j.ymssp.2020.107146

Jalalahmadi, B., Slack, T., Raje, N., & Arakere, N. (2009). A Review of Rolling Contact Fatigue. *Journal of Tribology, 131*. doi:10.1115/1.3209132

Kim, J., & Kim, J.-M. (2020). Bearing Fault Diagnosis Using Grad-CAM and Acoustic Emission Signals. *Applied Sciences, 10*(6), 2050. doi:10.3390/app10062050

Lei, Y. (2016). *Intelligent fault diagnosis and remaining useful life prediction of rotating machinery*.

Lei, Y., Yang, B., Jiang, X., Jia, F., Li, N., & Nandi, A. K. (2020). Applications of machine learning to machine fault diagnosis: A review and roadmap. *Mechanical Systems and Signal Processing, 138*, 106587. doi:https://doi.org/10.1016/j.ymssp.2019.106587

Leser, W., Yuan, F., & Newman, J. (2013). *Band-limited Green's Functions for the Quantitative Evaluation of Acoustic Emission using the Finite Element Method*.

Lundberg, G., & Palmgren, A. (1947). *Dynamic capacity of rolling bearings*.

Mahafza, B. R. (2016). *Radar Systems Analysis and Design Using MATLAB*: CRC Press.

Martin-del-Campo, S., & Sandin, F. (2017). Online feature learning for condition monitoring of rotating machinery. *Engineering Applications of Artificial Intelligence, 64*, 187-196. doi:https://doi.org/10.1016/j.engappai.2017.06.012

MATLAB. (2021a). datetime (Version R2020b). Natick, Massachusetts, United States: The MathWorks, Inc. Retrieved from https://se.mathworks.com/help/matlab/ref/datetime.html

MATLAB. (2021b). erfcinv (Version R2020b). Natick, Massachusetts, United States: The MathWorks Inc. Retrieved from https://se.mathworks.com/help/matlab/ref/erfcinv.html

MATLAB. (2021c). findpeaks (Version R2020b). Natick, Massachusetts, United States: The MathWorks Inc. Retrieved from https://se.mathworks.com/help/signal/ref/findpeaks.html

MATLAB. (2021d). highpass (Version R2020b). Natick, Massachusetts, United States: The MathWorks, Inc. Retrieved from https://se.mathworks.com/help/signal/ref/highpass.html

MATLAB. (2021e). isoutlier (Version R2020b). Natick, Massachusetts, United States: The MathWorks, Inc. Retrieved from https://se.mathworks.com/help/matlab/ref/isoutlier.html

MATLAB. (2021f). pspectrum (Version R2020b). Natick, Massachusetts, United States: The MathWorks, Inc. Retrieved from https://se.mathworks.com/help/signal/ref/pspectrum.html

Mba, D. (2006). Development of Acoustic Emission Technology for Condition Monitoring and Diagnosis of Rotating Machines: Bearings, Pumps, Gearboxes, Engines, and Rotating Structures. *The Shock and Vibration digest, 38*, 3-16. doi:10.1177/0583102405059054

McDonough, R. N., & Whalen, A. D. (1995). *Detection of Signals in Noise*: Elsevier Science.

Meserkhani, A., Jafari, S. M., & Rahi, A. (2021). Experimental comparison of acoustic emission sensors in the detection of outer race defect of angular contact ball bearings by artificial neural network. *Measurement, 168*, 108198. doi:10.1016/j.measurement.2020.108198

Morales-Espejel, G. E., & Gabelli, A. (2015). The Progression of Surface Rolling Contact Fatigue Damage of Rolling Bearings with Artificial Dents. *Tribology Transactions, 58*, 418-431. doi:10.1080/10402004.2014.983251

Nélias, D., & Yoshioka, T. (1998). Location of an acoustic emission source in a radially loaded deep groove ball-bearing. *Proceedings of the Institution of Mechanical Engineers, Part J: Journal of Engineering Tribology, 212*(1), 33-43. doi:10.1243/1350650981541877

Price, E. D., Lees, A. W., & Friswell, M. I. (2005). Detection of severe sliding and pitting fatigue wear regimes through the use of broadband acoustic emission. *Proceedings of the Institution of Mechanical Engineers, Part J: Journal of Engineering Tribology, 219*(2), 85-98. doi:10.1243/135065005x9817

Quiney, Z., Lees, A. W., Ganji, A., & Murray, B. (2012). *Acoustic emission for the detection of subsurface cracking in bearing condition monitoring.* Paper presented at the Institution of Mechanical Engineers - 10th International Conference on Vibrations in Rotating Machinery.

Rahman, Z., Ohba, H., Yoshioka, T., & Yamamoto, T. (2009). Incipient damage detection and its propagation monitoring of rolling contact fatigue by acoustic emission. *Tribology International, 42*(6), 807-815. doi:10.1016/j.triboint.2008.10.014

Romanowicz, P. J., & Szybiński, B. (2019). Fatigue Life Assessment of Rolling Bearings Made from AISI 52100 Bearing Steel. *Materials, 12*(3). doi:10.3390/ma12030371

Skolnik, M. I. (1990). *Radar Handbook, Second Edition*: McGraw-Hill.

Watanuki, D., Tsutsumi, M., Hidaka, H., Wada, K., & Matsunaga, H. (2021). Fracture mechanics-based criteria for fatigue fracture of rolling bearings under the influence of defects. *Fatigue and Fracture of Engineering Materials and Structures, 44*(4), 952-966. doi:10.1111/ffe.13405

Weik, M. H. (2001). Nyquist theorem. In M. H. Weik (Ed.), *Computer Science and Communications Dictionary* (pp. 1127-1127). Boston, MA: Springer US.

Yang, B., Lei, Y., Jia, F., & Xing, S. (2019). An intelligent fault diagnosis approach based on transfer learning from laboratory bearings to locomotive bearings. *Mechanical Systems and Signal Processing, 122*, 692-706. doi:https://doi.org/10.1016/j.ymssp.2018.12.051

Yoshioka, T. (1993). Detection of rolling contact sub-surface fatigue cracks using acoustic emission technique. *Lubrication Engineering, 49*, 303-308.

Zurita-Millán, D., Delgado-Prieto, M., Saucedo-Dorantes, J. J., Cariño-Corrales, J. A., Osornio-Rios, R. A., Ortega-Redondo, J. A., & Romero-Troncoso, R. d. J. (2016). Vibration Signal Forecasting on Rotating Machinery by means of Signal Decomposition and Neurofuzzy Modeling. *Shock and Vibration, 2016*, 2683269. doi:10.1155/2016/2683269
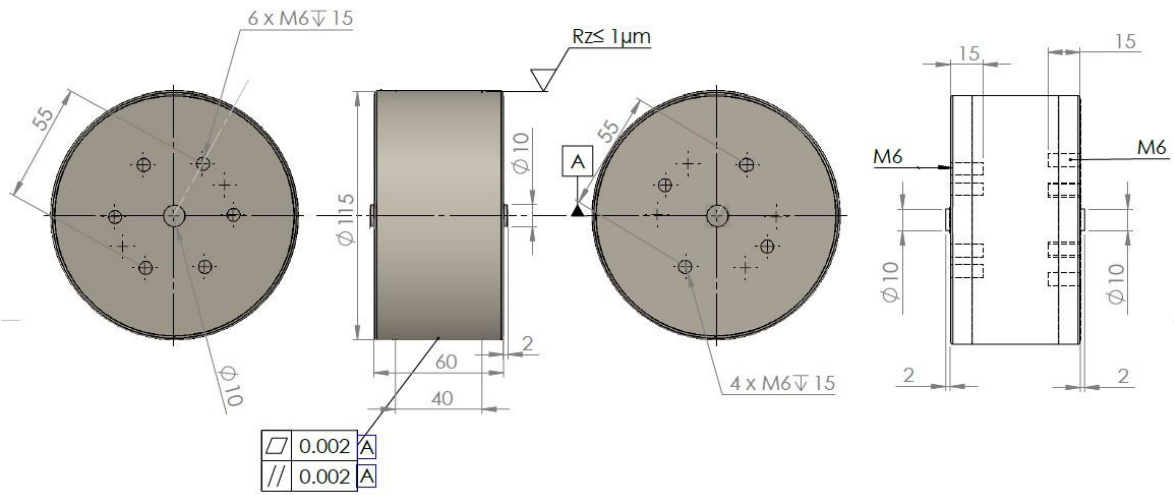
8 Appendix A
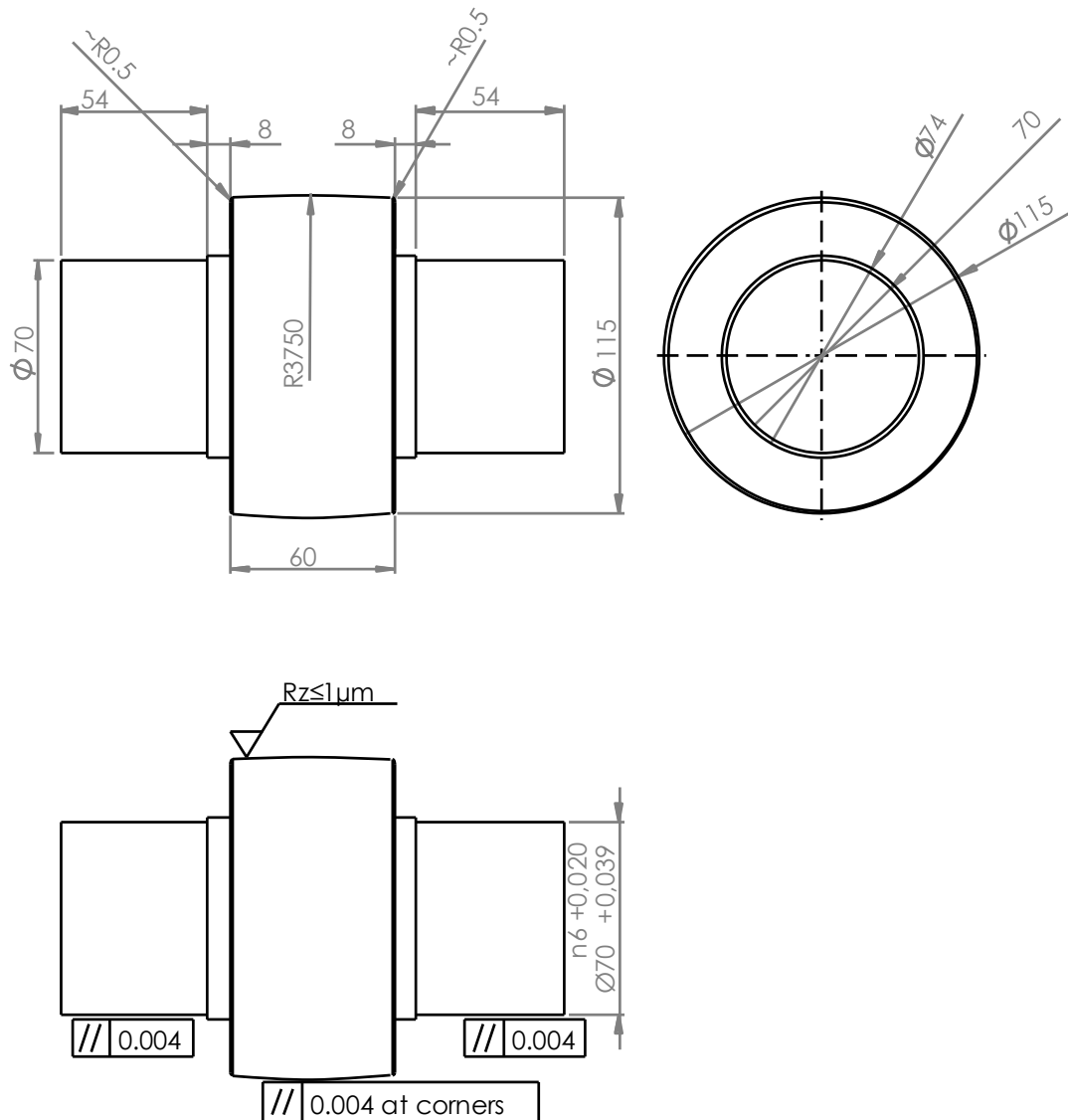
Final dimensions of the roller for precision grinding of the ⌀115.0mm contact surface with a continiuous radius curvature of 3750mm, and possible adjusment of the parallelity of the ⌀70mm axel.
The corners of the ⌀115 surface (~R0.5) are just slightly ground to avoid cutting sharpness.

9 Appendix B

Overall dimensional tolerances = ±0.05mm

10 Appendix C

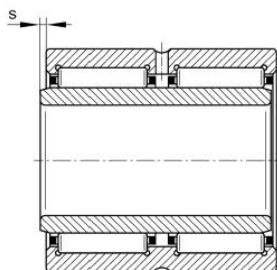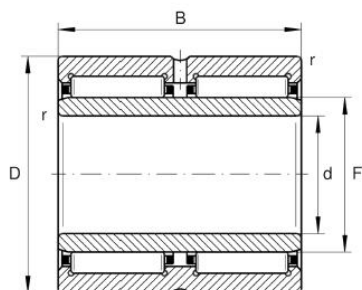**SCHAEFFLER**

NA6914-ZW-XL

Needle roller bearing

Schaeffler ID:
0507442670000

Needle roller bearings NA69..-ZW,
Dimension series 69, double row

X-life

Technical information

Main Dimensions & Performance Data

d	70 mm	Bore diameter
D	100 mm	Outside diameter
B	54 mm	Width
C_r	145.000 N	Basic dynamic load rating, radial
C_{0r}	265.000 N	Basic static load rating, radial
C_{ur}	48.000 N	Fatigue load limit, radial
n_G	5.700 1/min	Limiting speed
$n_{\vartheta r}$	3.300 1/min	Reference speed
	1,34 kg	Weight

Dimensions

F	80 mm	Raceway diameter inner ring
r_{min}	1 mm	Minimum chamfer dimension
s	1 mm	Axial displacement

Temperature range

T_{min}	-30 °C	Operating temperature min.
T_{max}	120 °C	Operating temperature max.

The datasheet is only an overview of dimensions and basic load ratings of the selected product. Please always observe all further information and guidelines for this product. For further information you can use the contact form on our website.

11 Appendix D
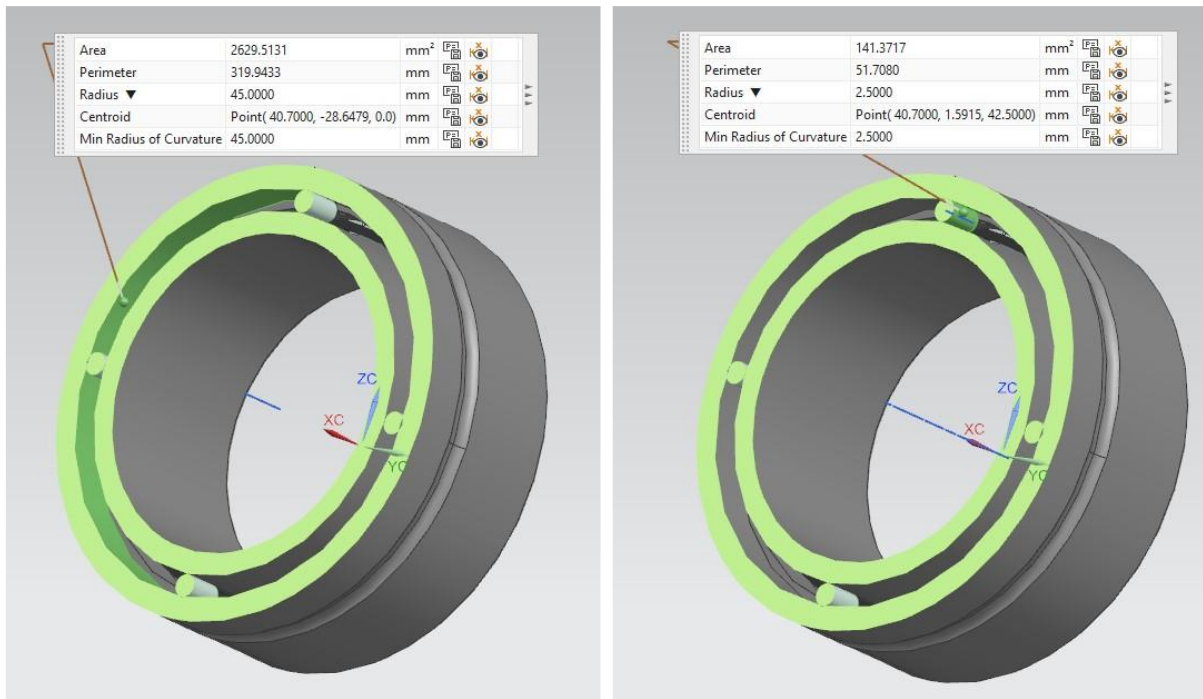
The number of rolling elements is 28.

12 Appendix E

GE20-PB
Radial spherical plain bearings
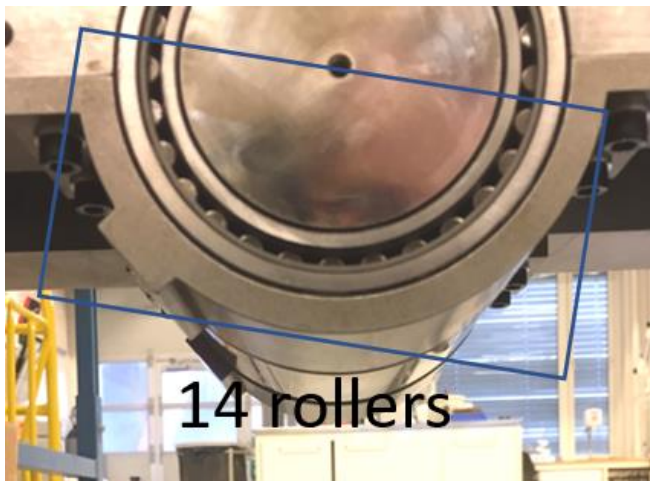dimension series K, requiring maintenance, to DIN ISO 12 240-1

🛒 Send to shopping basket
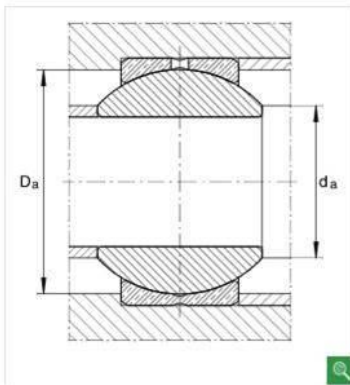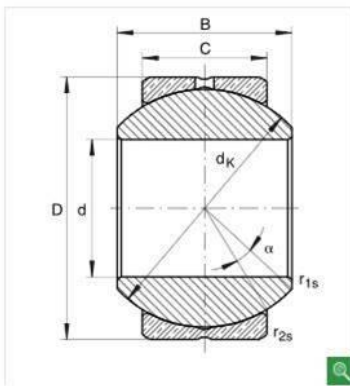
d	20 mm	Bore tolerance: H7 (arithmetic mean value)
		Tolerance: +0,021/0
D	40 mm	Tolerance: 0/-0,011
B	25 mm	Tolerance: 0/-0,12

	0,006 - 0,035 mm	Radial internal clearance Deviation from DIN 12240-1, dimension series K
C	18 mm	Tolerance: 0/-0,24
$D_{a\,min}$	31,5 mm	
$d_{a\,max}$	24,3 mm	
d_K	34,925 mm	
$r_{1s\,min}$	0,3 mm	Chamfer dimension
$r_{2s\,min}$	0,6 mm	Chamfer dimension
α	14 °	

m	0,15 kg	Mass
C_r	31400 N	Basic dynamic load rating, radial
C_{0r}	78600 N	Basic static load rating, radial

98

13 Appendix F

MISTRAS
A World of NDT Solutions | *Products & Systems Division*

2/4/6 Preamplifier

Description:
The 2/4/6 preamplifier was designed to be used with all available AE systems that have power supplied via the output signal BNC. It is supplied with 20/40/60 dB gain (switch selectable) and operates with either a single ended or differential sensor. Plug in filters provide the user with flexibility to optimize sensor selectivity and noise rejection. These filters are provided in the Low Pass (LP), High Pass (HP), and Band Pass (BP) configurations, and offers constant insertion loss for easy filter swapping without the need for recalibration. Automatic Sensor Test (AST) is standard. This option provides the sensor with the ability to characterize its own condition as well as send out a simulated acoustic emission wave that other sensors can detect.

Features:
- 20/40/60 Selectable Gain
- Wide Dynamic Range > 90dB Standard
- Low Noise < 2¤V (With Standard* Filter & Input Shorted)
- Large Output Signal 20Vpp into 50¤
- Single Power/Signal BNC or Optional Separate Power/Signal BNC
- Plug-in Filters (Utilizes the same filter as the SPARTAN 2000)
- High Input Impedance
- Standard Auto Sensor Test
- Input Protection

Electrical Specifications:
- Gain Selectable: 20/40/60 dB + 0.5% dB
- Input Impedance: 10KΩ // 15pF
- Power Required: 18-28V DC
- Operating Current: 30mA (With AST Installed)
- 28mA (Without AST Installed)
- Dynamic Range: 80dB (Utilizing an R15 Sensor)
  90dB (50Ω Input

Environmental Specifications:
- Temperature: -40 C to +65 C

Gain Selection	20dB	40dB	60dB
• Bandwidth (-3dB):	10kHz-2.5MHz	10kHz-2.0MHz	10kHz-900kHz
• Output Voltage (50Ω Load):	6Vpp	20Vpp	20Vpp
• CMRR (500kHz):	42dB	42dB	42dB
• Noise (RMS rti):			

Filter Frequency Response Hz	20dB With R15 Sensor	40dB With R15 Sensor	60dB With R15 Sensor	20dB Input Shorted	40dB Input Shorted	60dB Input Shorted
135k-185k	3 μV	1.4 μV	1.5 μV	2.0 μV	0.6 μV	0.42 μV
100k-300k*	3 μV	1.8 μV	1.8 ¤V	2.3 μv	1 μV	0.8 μV
10k-2.0M	5 μV	4 μV	3 μV	4 μV	3 μV	2.5 μV

*Standard filter

195 Clarksville Road, Princeton Junction, NJ 08550 USA
Phone: (609) 716-4000 • Fax: (609) 716-0706
Email: sales.systems@mistrasgroup.com • www.mistrasgroup.com

14 Appendix G

PAC 18-bit A/D, 1kHz - 3MHz PCI-2: The New AE Research Tool
2 Channels of Acoustic Emission for Simultaneous Waveforms and Feature Processing

BREAKTHROUGH!

In 1995, PAC introduced 16-bit 20 MHz A/D for AE. Now with the PCI-2, we are introducing our 18-bit **40 MSamples/sec** A/D for Lower Noise and Higher Speed.

Standard PCI

Pioneering a new 18-bit A/D architecture, the **PCI-2** is a low cost, 2-channels of simultaneous Acoustic Emission (AE) waveforms and features digital signal processing (DSP) system on a single full-size 32-bit PCI-Card, ready for operation in your PC or one of PAC's hardened PCs (for multiple channel operation).

Superior Noise Performance and Speed
...ideal for Research/Universities

Superior low noise and low threshold performance have been achieved with this revolutionary AE system design, through the use of an innovative **18-bit A/D conversion scheme**, with up to 40 MSample/second acquisition and real time sample averaging. Via the system's pipelined, real-time architecture, this performance is attained without sacrificing AE throughput speed.

With these features and its very low cost, the PCI-2 is ideal for laboratories, universities and industrial turnkey systems, and any application where low noise, low channel count and low cost are required, as well as where the use of an existing PC is desired.

Figure 1. PCI-2 AE System on a card

Through the high-performance PCI (Peripheral Component Interconnect) bus and Direct Memory Access (DMA) architecture, significant AE data transfer speeds can be attained, assuring a wide bandwidth bus for multichannel AE data acquisition and waveform transfer. In addition to two AE channels, the system also has **eight (8) parametric channels** for other transducers, such as strain gage, pressure, temperature, load, and more.

Data Streaming. . .Choice of AE Systems

Waveform data streaming capability is built within the board, allowing waveforms to be continuously transferred to the hard disk. The 32-bit PCI bus is the de-facto standard in all PC computers being shipped today. PCI-2 AE System cards can be implemented inside most standard PC computers or inside one of PAC's rugged, multichannel PAC system chassis, including the 8-channel benchtop chassis, the 12-channel portable AE system or a 4-channel notebook based chassis (μ-series).
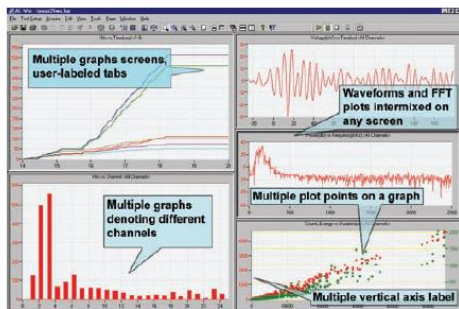
Figure 2. Simultaneous display of AE features and waveforms

Applications:

- Composite materials
- Aerospace structures
- Guided lamb wave systems
- Civil structures, concrete, steel
- Advanced materials testing
- Machine Monitoring, Tool touch and wear
- Acousto/Ultrasonic systems

- Ceramics high-resolution ultrasonic imaging
- On-line monitoring systems for bridges, composite structures, process control
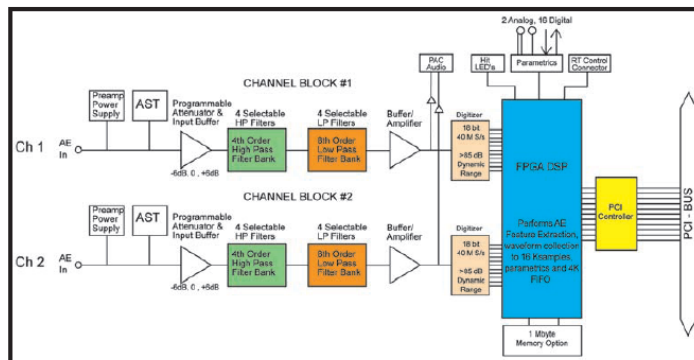- Tensile testing of samples and coupons

Figure 3. PCI-2 AE System block diagram.

Advanced Manufacturing. . .ISO Environment

Due to advances in surface mount technology and high density ASIC (high density Programmable Gate Arrays) devices, PAC has been able to provide this single AE System on a board with 2 complete high-speed AE channels of real time AE data acquisition, with real time feature extraction, waveform processing and transfer, eight (8) analog parametric input channels and 8 digital input and output control signals.

. .breakthrough A/D, speed, noise, quality and price. . .

User Friendly . . .by Design

• Software available for the PCI-2 includes the state-of-the-art **PACwin™ Software Suite.** With 30 years of Acoustic Emission application experience behind it, this Suite is comprised of three individual software packages (purchased separately); these are: AEwin™ real-time Windows acquisition, replay and analysis software, AEwinPost™ post analysis software and NOESIS™, the most complete Pattern Recognition (supervised or unsupervised) and Neural Networks software in the AE and NDT market today.

Key Features . . . *of the PCI-2 include*

♦ **Very low noise**, low cost, 2 channel complete, AE system on a card, with waveform and hit processing built in, on one full size, industry standard, 32-bit PCI card.

♦ Internal **18-bit A/D conversion** and processing for better resolution (less than 1 dB) at very low signal amplitudes, and low threshold settings, providing superior low noise performance.

♦ **40 MHz, 18-bit A/D conversion** with real time sample averaging (2x or 4x) to provide enhanced accuracy beyond any existing AE system on the market.

♦ Built-in, **real time AE feature extraction** and DMA transfer on each channel for high speed transient data analysis at high hit rates directly to the Hard Disk (HD).

♦ Built-in **waveform processing** with independent DMA transfer on each channel for high speed waveform transfer and processing.

♦ Designed with extremely high density FPGAs and ASIC ICs, to provide extreme high performance and minimize components and cost.

♦ 4 High Pass and 6 Low Pass **filter** selections for each channel, totally **under software control**.

♦ **AE Data Streaming** is also built into the PCI-2 board allowing continuous recording of AE waveforms to the hard disk at up to 10 MSamples/sec rate (on one channel, 5 MSamples/second on 2 AE channels).

♦ Up to **8 parametrics** on each PCI-2 board with **16-bit A/D** converter and update rates up to 10,000 readings/second. The first parametric is a full **Instrumentation conditioning** channel providing signal conditioning including gain control, offset control and filtering options for direct sensor input. The second provides a straight +/- 10 volt input for conditioned sensor outputs.

♦ Hit LED, and Audio drivers are built within the PCI-2 board, so that LEDs can be attached directly and sound can be processed via the PAC PCI-Audio Card (option).

♦ Digital signal processing circuitry virtually eliminates drift, thereby achieving high accuracy and reliability.
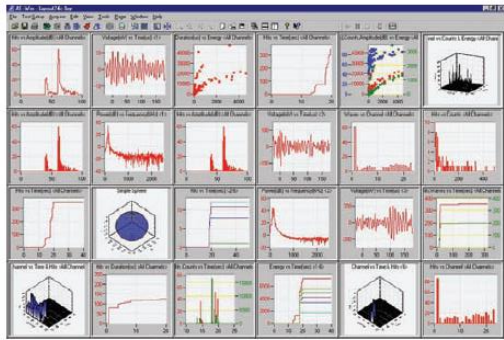
101

Figure 4. Many graphs per screen can be viewed in real time or replay. This screen shows some of the flexibility of AEwin™. In this overview, 2D and 3D graphs, waveforms, FFT's, line graphs, histograms, multi-plot graphs, etc. are shown.

- **Front Panel** activity lights are totally under the control of your PC to provide status on AE data as well as to give you indication of any malfunctioning of your system.

- **Audio** drives ready for high fidelity listening with your PAC PCI-Audio Card.

- **Auto Sensor** testing standard with all PAC systems for easy system/sensor self calibration and interface coupling efficiency monitoring.

System Flexibility. . . *by Design*

Standard 32-bit PCI hardware and 32-bit Windows AEwin™ software allows the customer maximum flexibility of using a PC or notebook computer. No need to change home made PCs, but ability to take advantage of today's PC speeds readily available with high performance PCI busses. Multiple AE channels (up to 20) are easily synchronized for multiple location algorithms.
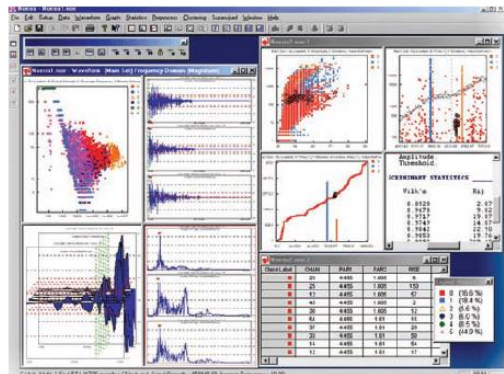

Figure 5. Noesis™ Software for the PCI-2 is sophisticated, yet user friendly and operates under Windows 2000

Software. . . *supported by PAC's AE multichannel systems experience since the early 70's*

PCI-2 is supported by PACwin™ Software Suite, a PAC Windows Platform consisting of AEwin™, AEwinPost™ and Noesis™ (individually purchased). All software runs in Windows 2000 and XP, thus taking advantage of standard features such as multi-tasking, graphic user interfaces, etc. and providing the ability to change AE parameters during test operation.

Multiple location algorithms are available including zohal, linear, planar, tank bottom, cylindrical, spherical (with ASME weld zones), conical, 3-D, advanced Non-Linear Regression (NLR) location, anisotropic 2-D, anisotropic cylinder and over-determined planar location for exceptional accuracy. All location algorithms utilize attenuation tables/curves, auto-sensor placement, and source corrected amplitude for more accurate location and AE intensity calculation.

PCI-2 Specifications:

Physical:
- Size: 13.415" L x 4.3" H x 0.7" T
- Weight: 1.1 lbs.
- Power Consumption: 12 Watts
- DC Power: +12.0 volts, 1.0 amps
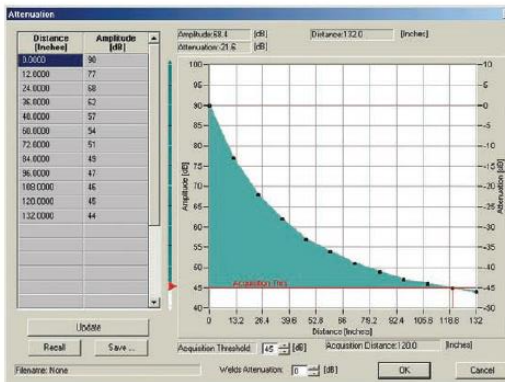   -12.0 volts, 0.05 amps
       +5.0 volts, 1.5 amp

Figure 6. AEwin™ Software can use an attenuation profile of the AE response on the structure. This information is important in determining the source amplitude of an AE event. Attenuation profiles can easily be constructed and displayed in tabular and graphical form. They can be saved and recalled. AEwin™ automatically determines the amplitude at the source (Source Amplitude) and provides this as a graphable AE feature.
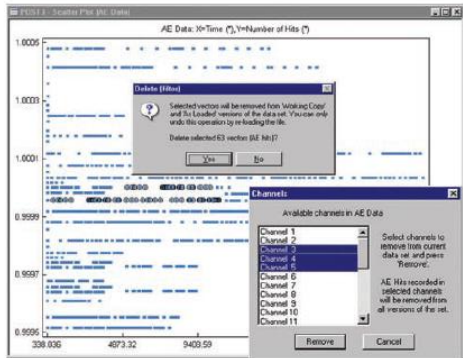
102

PCI-2 Acoustic Emission System on a Card

Figure 7. *AEwinPost™ offers a number of ways to filter data including: Select – Delete operation. Simply select the data to be filtered and press delete; filtering via graphical filters; and dedicated channel filters.*

PCI-2 Specifications (continued):

Environmental:
* Operating Temperature: 41° – 115° F (5° - 45° C)
* Storage Temperature: -4° – 140° F (-20° - 60° C)

Electrical:
* AE Inputs: 2 channels
* Input Impedance: 50 ohm or 1000 ohm, jumper selectable
* Preamplifier Power: Jumper selectable 0 volt or 28 VDC, 100 ma current limited (on BNC center conductor for phantom powering of external preamplifiers)
* Sensor Testing: AST built-in
* Frequency Response: 1 kHz – 3 MHz (at -3 dB points)

Signal Processing:
* AE Signal Gain: 0dB, 6 dB computer selectable input signal scaling
* Filters: 4 High Pass - computer selectable filters 1 kHz, 20 kHz, 100 kHz, 200 kHz, 4th order Butterworth

  6 Low Pass - computer selectable filters 100 kHz, 200 kHz, 400 kHz, 1 MHz, 2 MHz, 3 MHz, 6th order Butterworth
* Noise: Min. Threshold: 17 dB without AE Sensor, 22 dB with (1 kHz - 3 MHz bandwidth) R15 AE Sensor and 2/4/6 preamplifier, 24 dB with R15I Integral Preamp sensor

  Note: Lower noise will be achieved using narrow band filtering
* ASL Noise: 4 dB maximum, (with no input)
* Max. Signal Amplitude: 100 dB AE ASL99 dB
* ADC Type: 18 bit 40 MSPS per channel maximum

---

* Dynamic Range: > 85 dB, 2 kS/s, 5 kS/s, 10 kS/s, 20 kS/s, 50 kS/s
* Sample Rate: Computer selectable 100 kS/s, 200kS/s, 500kS/s, 1M-Samples/sec, 2 MSPS, 5 MSPS, 10 MSPS, 20 MSPS, 40 MSPS
* Sample Averaging: 40 MSPS with 2x averaging, for a 20 MSPS effective sample rate
* Extracted AE Features: Time of 1st Threshold Crossing, Counts to Peak, Peak Amplitude, Signal Strength, Duration, Rise Time, Counts, True Energy, RMS, ASL, Parametric 1 & 2.

Analog Parametrics:
* Parametric Channels: 8 Channels
* Parametric A/D Resolution: 16 bits
* Parametric Sample Rate: 10 kHz sample rate for each analog parametric
* Time Driven Data Rate: Controlled by software 10 msec. to 1800 seconds
* Time Parametrics: All 8 parametrics are available in time data set
* Parametric #1,3,5,7 Functions: Computer selectable Input Range ± 10.0v, ±1.0 v, ±0.10v, ±0.01v

  Computer selectable 30 Hz Low Pass filter or none

  5.0 V software programmable offset control with 12 bit DAC

  0 – 10 volt programmable excitation voltage for strain gage bridges
* Parametric #2,4,6,8 Functions: Parametric Input Range ± 10.0 v fixed, no filter

Digital I/O:
8 Digital Inputs, 8 Digital Outputs (5 v tolerant), TTL level compatible)

AE Out and Audio Monitor Interface:
Analog switch and buffer to select desired AE channel to be routed to standard PAC audio monitor board or AE output signal

LED Activity Monitor:
On board LED driver to directly drive LED's on front panel. LED minimum on-time is 0.05 seconds.
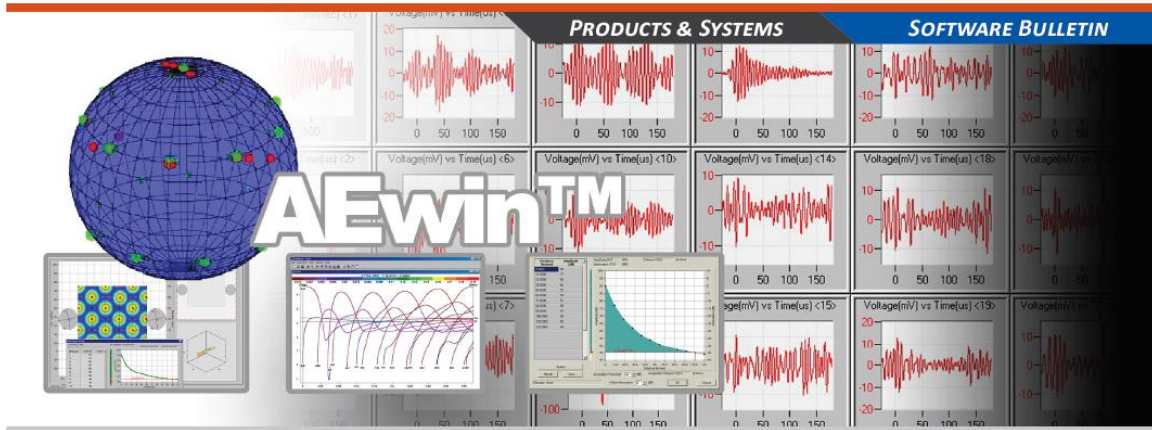
For more information:
Call **(609) 716-4000**
or Email us at **sales.systems@mistrasgroup.com**

Visit our website at:
www.mistrasgroup.com

CE

---

195 Clarksville Road, Princeton Junction, NJ 08550 USA
Phone: (609) 716-4000 • Fax: (609) 716-0706
Email: sales.systems@mistrasgroup.com • www.mistrasgroup.com.com

Specifications subject to change without notice. PAC #102803

AEwin™ | Comprehensive, Versatile & Friendly AE Software

AEWIN™ FEATURES OVERVIEW

AEwin™ is a Windows™ compatible (XP, Windows 8, and Windows 7) software for real-time "simultaneous" Acoustic Emission (AE) feature and waveform processing, display, fast storage and replay. Used for true, real-time operation and control with your MISTRAS AE Systems (Express-8, PCI2, SAMOS, SH II, SH III, AE USB Node, Wireless AE Node).

AEwin™ also features complete compatibility with MISTRAS' standard data file format (DTA), allowing you to replay and analyze your previously collected AE files and framework for easily adding graphs and additional graph screens and user controllable tool bars including: setup icons, acquisition control, line listing, status and statistics. Includes real-time connectivity with Industrial Control Systems (Modbus, OPC)

GRAPHIC CAPABILITIES

- Exceptional 2-D and 3-D graphing capabilities that allow the setup of multiple graphs on a screen, limited only by the screen resolution
- Toggling between multiple screens by selecting a user-labeled tab

- Mouse-driven "Data Selection" features that allows designation of hits, waveforms and events from graphs for detailed analysis and filtered export
- Ability to set up and individually size (on screen) many different types of graphs including; 2-D line graphs, histograms, point plots, waveforms, FFTs, overlays, multiple plots on a single graph and color options
- Arrange multiple graphs on a screen
- Expandable to full screen with zooming and panning for close-up analysis
- Full cursor readout capability
- Alarms triggered by graph data

LOCATION & CLUSTERING OPTION

- 1, 2 and 3 dimensional location modes
- Allows setup of multiple location groups
- Provides mouse-oriented sensor placement and editing features
- Allows selection of type of structure (plate, vessel, etc.) for setup, viewing & location
- Incorporates attenuation profiling into location software (to view a sensor coverage map and provide source amplitude info)
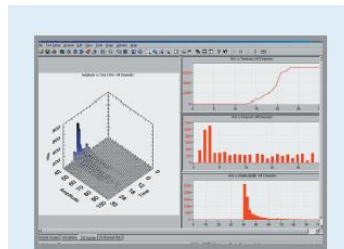
Above: AEwin's 3-D graphing capability allows the graph to be rotated freely, using the mouse.
Below: A typical activity screen with both AE features and waveforms, processed with a simple mouse clickz for any specific hit.
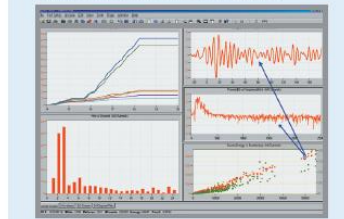
16 Appendix I

PRODUCT DATA SHEET

WD Sensor
Wideband Differential Sensor
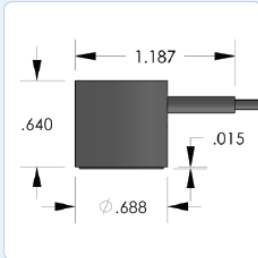
DESCRIPTION AND FEATURES

WD is a true differential wideband sensor with a very high sensitivity and bandwidth. It has a very good frequency response over the range of 100 – 900 kHz. Differential sensors differ from their general purpose counterparts by employing two sensing elements with opposite polarization directions. The two signal leads feed into a differential pre-amplifier which eliminates common-mode noise resulting in a lower noise output from the pre-amplifier. Noise improvements to the tune of 2 dB can be achieved using differential sensors over a single ended sensor. This sensor features a rugged steel construction with an integrated twin axial cable exiting on the side.

APPLICATIONS

This sensor is well suited for structural health monitoring of large structures like storage tanks, pipelines etc. This sensor is an ideal candidate for applications requiring high bandwidth for frequency analysis of the AE signals for noise discrimination and source identification. Wideband sensors are particularly well suited for research applications where a high fidelity AE response is required. It can be easily mounted using epoxy.
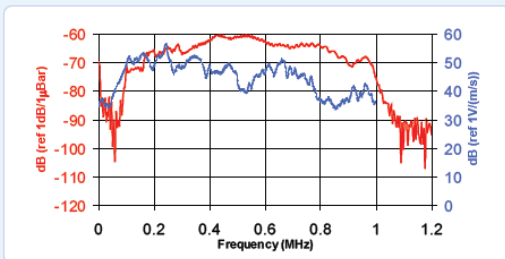
OPERATING SPECIFICATIONS

Dynamic
Peak Sensitivity, Ref V/(m/s).. 56 dB
Peak Sensitivity, Ref V/μbar......................................-61 dB
Operating Frequency Range .... 125-1000 kHz
Resonant Frequency, Ref V/(m/s).............................125 kHz
Resonant Frequency, Ref V/μbar ....450 kHz
Directionality .... +/-1.5 dB

Environmental
Temperature Range .... -65 to 177ºC
Shock Limit ....500 g
Completely enclosed crystal for RFI/EMI immunity

Physical
Dimensions...0.7"OD X 0.65"H
                                        17.8 mm OD X 16.5 mm H
Weight..20 grams
Case Material.. Stainless Steel
Face Material... Ceramic
Connector .... BNC
Connector Locations..Side

ORDERING INFORMATION AND ACCESSORIES
WD.. WD
Cable (specify length in '-XX' m at end of PN)................ 1 m
Magnetic Hold-Down .... MHSTD
Pre-Amplifier 0/2/4, 2/4/6
Preamp to System Cable (specify length in 'm') 1234-X
Amplifier Subsystems ....AE2A or AE5A

Sensors include
NIST Calibration Certificate & Warranty

17 Appendix J

MISTRAS

Micro30D Sensor
Miniature Differential Sensor
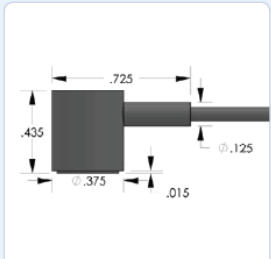
DESCRIPTION AND FEATURES

MICRO30D is a differential sensor designed to isolate the sensing terminals electrically from the cavity. This electrical isolation makes the sensor particularly useful for applications where high background electrical noise is a major concern. It has a very good sensitivity and frequency response over the range of 150 – 400 kHz. The two signal leads from the sensing element feed into a differential pre-amplifier which eliminates common-mode noise resulting in a lower noise output from the pre-amplifier. This sensor features a rugged steel construction and a dual BNC connector with an integrated twin axial cable exiting on the side.

APPLICATIONS

This sensor is well suited for structural health monitoring of large structures like storage tanks, pipelines etc. Wideband sensors are well suited for research applications where a high fidelity AE response is required. It can be easily mounted using epoxy.
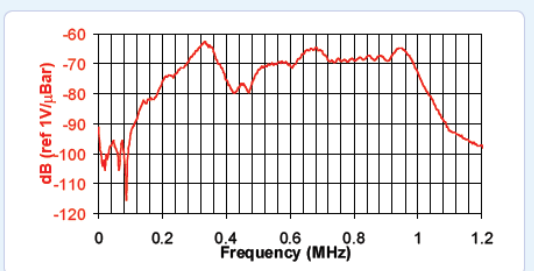
OPERATING SPECIFICATIONS

Dynamic

Peak Sensitivity, Ref V/(m/s) .... 65 dB
Peak Sensitivity, Ref V/μbar .... -67.5 dB
Operating Frequency Range .... 150-400 KHz
Resonant Frequency, Ref V/(m/s) .... 125 KHz
Resonant Frequency, Ref V/μbar .... 225 KHz
Directionality .... +/-1.5 dB

Environmental

Temperature Range .... -65 to 177ºC
Shock Limit .... .500 g
Completely enclosed crystal for RFI/EMI immunity

Physical

Dimensions .... 0.375"OD X 0.435"H
.... 18.4 mm OD X 11 mm H
Weight .... 23 grams
Case Material .... Stainless steel
Face Material .... ceramic
Connector .... Dual BNC
Connector Locations .... Side

ORDERING INFORMATION AND ACCESSORIES

MICRO30D MICRO30D
Cable (specify length '-XX' m at end of PN) .... 1 m
Amplifier Subsystems AE2A, AE5A
Pre-amplifier 0/2/4, 2/4/6, ILD40

Sensors include

NIST Calibration Certificate & Warranty

www.mistrasgroup.com

18 Appendix K

OLYMPUS

Industrial Solutions

Thickness and Flaw Inspection Solutions

OmniScan SX

Contact Us   Get a Quote   Request a Demo

Overview

Olympus is proud to introduce the OmniScan® SX, a flaw detector that benefits from more than 20 years of phased array experience and shares the OmniScan DNA. For improved ease of use, the OmniScan SX features a new streamlined software interface displayed on an 8.4 in. (21.3 cm) touch screen. A single-group and non-modular instrument, the OmniScan SX is easy to operate and cost-effective for less demanding applications.

360° View

The OmniScan SX comes in two models: the SX PA and SX UT. The SX PA is a 16:64PR phased array unit, which, like the UT-only SX UT, is equipped with a conventional UT channel for pulse-echo, pitch-catch or TOFD inspection. Compared to the OmniScan MX2, the SX is 33% lighter and 50% smaller, offering an unprecedented level of portability for an OmniScan.

The OmniScan SX touch screen offers a full-screen mode option that maximizes visibility, essentially converting many menu functions into easy touch-screen operations. The intuitive interface provides smooth menu selection, zooming, gate adjustments, cursor movements, and text and value input. These, along with other premium integrated features, including easy-to-follow setup and calibration Wizards, a rapid refresh rate for both the S-scan and A-scan displays, and a fast pulse repetition frequency (PRF), make the OmniScan SX a highly efficient inspection tool.

https://www.olympus-ims.com/en/omniscan-sx/

19 Appendix L

HSIO-100-A
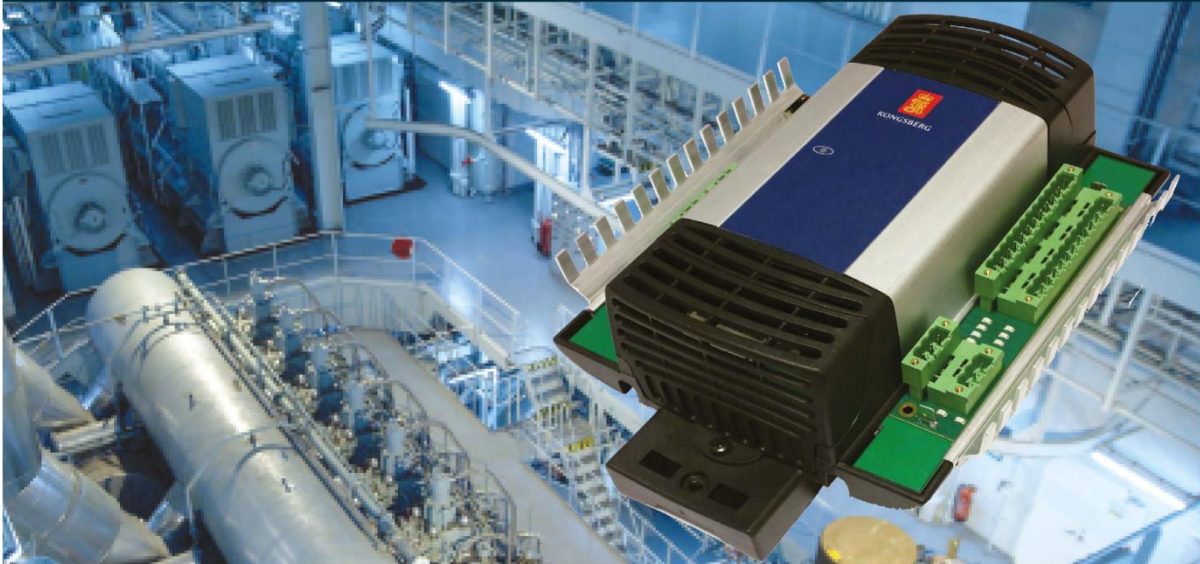
KONGSBERG

HIGH-SPEED I/O MODULE FOR CONDITION MONITORING

The Kongsberg HSIO-100-A high-speed acquisition module has outstanding signal processing and measurement capability making it highly appropriate for Condition Monitoring. The high-speed acquisition module is suitable for acoustic emission sensors. The module has 8 analog inputs and 4 digital I/O and can easily be extended to multiple synchronous channels via the high-speed internal bus. High accuracy and dynamic range over a wide temperature area gives high quality data. Raw data can be sent to databases for storage, trending and pre-processing. Hit count and other feature extraction parameters, together with signal analysis, help to identify status or faults of critical parameters of the machinery. Based on this information the user can plan the maintenance tasks of the equipment such as replacing worn-out components before they fail. This has the potential to save the owner significant amounts of work and money.

Principle of operation

The module is based upon an Altera Cyclon V processor with FPGA (Field Programmable Gate Array) technology. The FPGA enables parallel and high-speed data analysis of the raw data on several channels simultaneously. The module provides high-speed communication via Ethernet to analysis software.

Features & Benefits
- Compact 12 channel module
- Up to 2 MS/s sampling rate
- 24 bits ADC
- High dynamic range
- Supports channel extension
- 2 speed inputs
- Synchronous sampling
- Rated from - 40°C to +70°C
- Approved for Marine certification standards
- Ethernet/IP communication
- FPGA for real time data processing

TECHNICAL SPECIFICATIONS

Electrical and general:

Power supply	24 VDC (18 - 32 VDC)
Max power consumption	20 W
Operating temperature	- 40 °C to +70 °C
Enclosure	IP 21
Memory	SDRAM 8 Gb, MicroSDHC
Communication	Ethernet (100 Mbit/s)
Module mounting	DIN 35 mm rail
I/O connectors	16-pin female x 1
	3-pin female x 2
	2-pin female x 2
	SMA x 8
Removable front screw connection	Nominal cross section 2.5 mm²
Weight	895 g

Dynamic inputs:

Number of channels	8
Input range	Selectable up to maximum 20.9 V_{pp}
Frequency range	0.5 Hz - 900 kHz
Dynamic range	> 90 dB
Crosstalk	- 112 dB (f_{in} = 300 kHz)
Total accuracy	1.0 % FRO [1]
Repeatability	< 0.1 % FRO [1]
Sensor and preamplifier power	20 VDC
Input impedance	> 10 kΩ
Overvoltage protection	≥ 30 V

Digital inputs:

Number of channels	2
Input type	3-wire
Input range	0 - 24 VDC
Input frequency	Up to 1 MHz
Max power	2.5 W
Input impedance	> 15 kΩ

Digital outputs:

Number of channels	2
Output	0/24 V (open collector)

Complies with:

EN 60945:2002
IACS E10:2014
IEC 60533:2015
EN 61000-6-1:2007
EN 61000-6-2:2005
EN 61000-6-3:2007 + A1:2011
EN 61000-6-4:2007 + A1:2011
EN 61326-1:2013

Approvals:

Marine Class approvals	ABS, DNV-GL, LRS

[1] FRO = Full Range Output

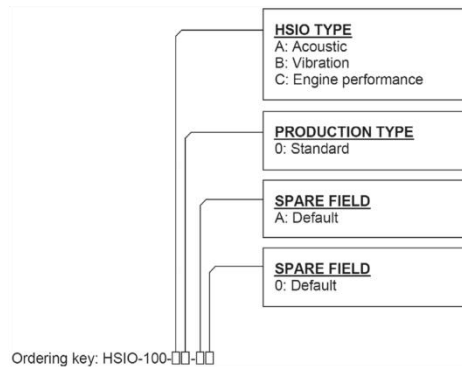*Specifications subject to change without any further notice.*
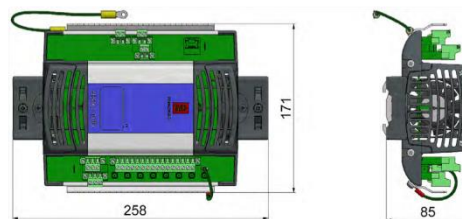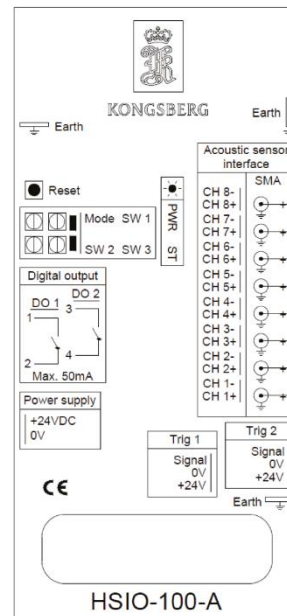

Figure 1: Ordering Key

Figure 2: Dimensions

Figure 3: Available pin assignment on HSIO-100-A

P-HSIO-100-A/CE Rev. A

20 Appendix M

GLEITMO 591

High-temperature paste, resistant to chemicals, for high-speed bearings

Performance Features

temperature range: -25 / +260 °C, short-term up to +280 °C
resistant to many chemicals and solvents
allows long lubrication intervals due to low evaporation losses
protects against corrosion
extremely pressure-resistant
resistant to oxidation

Description

GLEITMO 591 is an extraordinary special paste based on a synthetic oil of high stability and white solid lubricants. It is resistant to many aggressive chemicals and offers an excellent compatibility with a lot of elastomer and plastic materials.

Field of application

Due to its high thermal stability GLEITMO 591 is particularly well-suited for the lubrication of high-speed, high-temperature plain and roller bearings, for permanent lubrication of areas subjected to high temperatures and aggressive media, such as high-speed bearings at high temperatures, fans, electric motors, conveyor chains, centrifuge bearings, and stenter frame bearings in the textile industry.

Method of application

Bearings and sliding surfaces should be carefully cleaned with METABLANC PFPE. Please consider our Technical Information sheet concerning the lubrication with PFPE pastes.

Note